

Universität Stuttgart

Hybrid plasmonic devices for sensing and thermal imaging

Von der Fakultät Mathematik und Physik der Universität Stuttgart
zur Erlangung der Würde eines Doktors der
Naturwissenschaften (Dr. rer. nat.) genehmigte Abhandlung

vorgelegt von
Andreas Tittl
aus Heidenheim an der Brenz

Hauptberichter: Prof. Dr. H. Giessen
Mitberichter: Prof. Dr. P. Michler & Prof. Dr. T. Zentgraf
Vorsitzender: Prof. Dr. H. P. Büchler

Tag der mündlichen Prüfung: 15.07.2015

4. Physikalisches Institut der Universität Stuttgart

Juli 2015

I hereby certify that this dissertation is entirely my own work except where otherwise indicated. Passages and ideas from other sources have been clearly indicated.

Stuttgart, July 2015

Andreas Tittl

ABSTRACT

Plasmonics is an emerging field in nanooptics, which focuses on the optical properties of resonant subwavelength metal nanoparticles. Historically, such geometries commonly employed noble metal nanoparticles to achieve a variety of effects ranging from nanofocusing of light to negative refraction.

Building on these concepts, this thesis investigates hybrid nanoplasmonic devices, which combine passive noble metal nanostructures with chemically reactive or actively tunable materials to obtain novel functionalities.

Utilizing various complex plasmonic geometries, this work pursues two complementary threads of research, covering the technological scale from fundamental science to device applications.

On the one hand, it utilizes chemically synthesized hybrid plasmonic “smart dust” nanoprobe to detect progressively lower reagent concentrations. Starting from silica shell-isolated gold nanoparticles, which are used to map the catalytic reactions in adjacent extended palladium thin films, DNA-assembled bimetallic plasmonic nanosensors are investigated to resolve changes in sub-5 nm Pd nanocrystals on the single antenna level, pushing the lower limit of chemical detection volume.

On the other hand, it studies plasmonic perfect absorber structures, optical elements designed to absorb all radiation of a certain wavelength, which have shown promise for a variety of technological applications. Here, the focus is on both developing a theoretical model for the optical behavior of plasmonic perfect absorber structures, especially at large incident angles, as well as on the experimental realization of efficient gas sensors and active mid-infrared imaging devices.

ZUSAMMENFASSUNG

Als zentraler Bestandteil der Nanooptik beschäftigt sich die Plasmonik mit dem Studium der optischen Eigenschaften von resonanten metallischen Nanostrukturen. Hierbei wurden bislang vor allem Edelmetalle wie Gold und Silber eingesetzt, was jedoch nur passive plasmonische Geometrien erlaubt.

Hiervon ausgehend beschäftigt sich diese Arbeit mit neuartigen hybriden plasmonischen Nanostrukturen. Diese verbinden Edelmetall-Komponenten mit chemisch reaktiven oder extern schaltbaren Materialien um optische Elemente mit neuen Funktionalitäten zu realisieren. In diesem Kontext werden zwei komplementäre Forschungsrichtungen zwischen Grundlagenforschung und technischer Anwendung genauer betrachtet.

Auf der einen Seite steht die Untersuchung chemisch synthetisierter hybrider Nanopartikel (sogenannter "smart dust") zum Nachweis von Chemikalien und Spurengasen in geringen Konzentrationen. Hierzu werden zunächst Siliziumdioxid-überzogene Gold-Nanopartikel eingesetzt um lokale katalytische Reaktionen in benachbarten Palladium-Schichten zu detektieren. Weiterführend wird DNA Nanotechnologie verwendet um kleine Palladiumpartikel kontrolliert in der direkten Umgebung von Gold Nanoantennen zu platzieren. Hierdurch gelingt der optische Nachweis von chemischen Reaktionen in weniger als 5 nm großen Metall-Hydrid Partikeln für sehr kleine Detektions-Volumina.

Auf der anderen Seite befasst sich die Arbeit mit sogenannten plasmonischen perfekten Absorbern. Hierbei handelt es sich um optische Elemente, welche für die vollständige Absorption von Licht einer bestimmten Wellenlänge ausgelegt sind. Hier liegt der Fokus unter anderem auf der Entwicklung eines theoretischen Modells für die optischen Eigenschaften solcher Strukturen, insbesondere bei hohen Einfallswinkeln. Weiterhin werden perfekte Absorber für Anwendungen als effiziente Gassensoren sowie für die thermische Bildgebung im Mittelinfraroten experimentell realisiert.

AUSFÜHRLICHE ZUSAMMENFASSUNG

Die Plasmonik beschäftigt sich mit der Untersuchung von optischen Anregungen in nanoskaligen Metallstrukturen. Als Schlüsseltechnologie im Bereich der Nanooptik hat sie hierbei in den letzten Jahren vielseitige Anwendungen hervorgebracht und Materialien mit negativem Brechungsindex, verbesserte Solarzellen oder biokompatible Sensoren ermöglicht.

Triebfedern dieser bemerkenswerten Entwicklung sind Fortschritte in der Nanotechnologie, speziell in der Strukturierung von Materialien auf der Nanoskala. Hierbei unterscheidet man zwischen "top down" Techniken wie beispielsweise der Elektronenstrahl-Lithographie und der Nanoimprint-Lithographie, sowie den "bottom up" Techniken, die stärker in der chemischen Synthese verwurzelt sind.

Diese Durchbrüche im Bereich der Nanostrukturierung haben die experimentelle Realisierung von immer kleineren plasmonischen Strukturen ermöglicht und somit den Arbeitsbereich der Plasmonik vom Giga- und Terahertz-Bereich bis zum nahinfraroten und sichtbaren Spektralbereich ausgedehnt.

Die physikalische Grundlage der Plasmonik ist die Fähigkeit kleiner Metallpartikel, einfallendes Licht auf der Nanoskala zu bündeln und somit sehr hohe elektrische Feldstärken in kleinen Volumina zu erzeugen. Hierfür verantwortlich sind Oszillationen der Leitungselektronen vor dem Hintergrund der positiv geladenen Atomkerne, welche resonant über eine einfallende Lichtwelle angeregt werden können.

Das spektrale Verhalten solcher plasmonischen Anregungen (speziell die Absorptions- und Streuquerschnitte) kann nur für sehr einfache System analytisch berechnet werden. In komplexeren Systemen hängen die Plasmon-Resonanzposition und -Linienform stark von der Geometrie, der Materialzusammensetzung und der Umgebung der Nanostrukturen ab.

Anfänglich hat sich die Plasmonik-Forschung hauptsächlich auf Edelmetall-Nanopartikel konzentriert, da diese nur geringe

Materialverluste zeigen und somit Resonanzen von hoher Güte ausbilden. Beginnend von einfachen kugel- oder stabförmigen Strukturen wurden zunehmend komplexe Anordnungen mehrerer Partikel realisiert und die Kopplung solcher Resonatoren in zwei und drei Dimensionen untersucht. Solche komplexen gekoppelten Systeme zeigen bemerkenswerte optische Effekte, angefangen von effizienter Absorption einfallender Strahlung bis hin zu Strukturen, die zirkularen Dichroismus aufweisen.

Um neue Anwendungsfelder für die Plasmonik zu erschließen ist es jedoch nötig, die bislang häufig verwendeten (aber inhärent passiven) Edelmetalle wie Silber und Gold um neuartige Materialien zu ergänzen. Die Verbindung von passiven Komponenten mit chemisch reaktiven oder extern schaltbaren Materialien zu *hybriden* plasmonischen Strukturen eröffnet neue Freiheitsgrade für das Design solcher Geometrien, und erlaubt die Erweiterung bestehender Systeme durch neue Funktionalitäten.

In diesem Kontext beschäftigte sich die vorliegende Arbeit mit zwei komplementären Forschungsrichtungen im Spannungsfeld zwischen Grundlagenforschung und technischer Anwendung.

Zunächst lag ein Fokus der Arbeit auf dem komplett optischen Nachweis chemischer und katalytischer Reaktionen für sehr kleine Gaskonzentrationen und Detektions-Volumina. Ein zentrales Konzept für solche nanoplasmonischen Sensoren ist die antennenverstärkte Detektion, im Rahmen derer eine effiziente optische Antenne verwendet wird um kleine chemische Änderungen in einem benachbarten reaktiven Material aufzulösen.

Aufgrund der großen technologischen Bedeutung diente die katalytische Dissoziation von Wasserstoff-Molekülen und die anschließende Hydridbildung in Palladium als ideales Modellsystem für ein solches reaktives Material.

Um die grundlegenden Wirkprinzipien in solchen antennenverstärkten nanoplasmonischen Sensor-Geometrien zu identifizieren, wurde das Verhalten eines Palladium Nanopartikels im Fokus einer dreieckigen Gold Nanoantenne mittels ausgedehnter numerischer Simulationen untersucht. Hierbei zeigte sich, dass neben der wasserstoffabhängigen Brechungsindexänderung im Palladium ebenfalls die Ausdehnung des Palladium-Gitters be-

rücksichtigt werden muss, um ein solches System physikalisch korrekt zu beschreiben.

Antennenverstärkte Sensor-Geometrien liefern zwar hohe Sensitivitäten, jedoch ist ihre Herstellung mittels "top down" Nanofabrikationstechniken kompliziert und erfordert hohe maschinelle Genauigkeiten in der Lithographie.

Um flexiblere und einfacher herzustellende Nanosensoren zu realisieren konzentrierte sich die Arbeit deshalb im weiteren Verlauf auf die Untersuchung chemisch synthetisierter hybrider Nanopartikel (auch "smart dust" genannt) zum Nachweis von Chemikalien und Spurengasen in geringen Konzentrationen.

Hierzu wurden zunächst Siliziumdioxid-überzogene Gold-Nanopartikel eingesetzt um lokale katalytische Reaktionen in benachbarten Palladium-Schichten zu detektieren. Speziell wurde gezeigt, dass schon kleine Änderungen der Filmdicke und Film-morphologie zuverlässig und komplett optisch nachgewiesen werden konnten. Hierbei führte eine Änderung der Filmdicke um lediglich 5 nm bereits zu einer Änderung der Sensorantwort um mehr als 50 %.

Die genannten Au@SiO₂ Nanosensor-Partikel sind ideal um lokalisierte chemische Reaktion auf ausgedehnten Katalysator-Schichten aufzulösen. Um diesen konzeptuellen Ansatz nun auf die Detektion weniger Moleküle bestimmter chemischer Substanzen auszudehnen, müssen integrierte Sensor-Geometrien mit sehr geringen Detektions-Volumina realisiert werden.

Hierzu wurde DNA-Nanotechnologie verwendet um weniger als 5 nm große Palladium Nanokristalle präzise in der unmittelbaren Umgebung von chemisch synthetisierten, stabförmigen Gold Nanoantennen zu platzieren. Die DNA-Verbindungselemente erlauben eine kontaktfreie Anordnung der Sensorkomponenten mit extrem geringen Abständen (< 2 nm), was eine optimale Ausnutzung der plasmonischen Nahfeldverstärkung im Bereich der Antenne gewährleistet.

Die spektrale Antwort einzelner DNA-Nanosensoren wurde für verschiedene Wasserstoff-Konzentrationen gemessen und die Hydrid-Bildung in solchen winzigen Palladium Nanokristallen erstmals optisch nachgewiesen.

Ein zweiter Fokus der Arbeit war die Untersuchung sogenannter plasmonischer perfekter Absorber. Hierbei handelt es sich um optische Elemente, welche für die vollständige Absorption von Licht einer bestimmten Wellenlänge ausgelegt sind. Während "smart dust" Nanopartikel ideal für den Nachweis extrem kleiner Konzentrationen und das Erreichen winziger Detektionsvolumina geeignet sind, können plasmonische perfekte Absorber als Grundlage für technologisch relevante Sensoren in industriellen Anwendungen dienen.

Um dieses Konzept für die Gassensorik zu realisieren wurde eine Geometrie bestehend aus Palladium Nanodrähten über einer Magnesiumfluorid Abstandsschicht und einem Goldspiegel betrachtet. Durch Optimierung der kritischen Strukturparameter konnte die Reflexion der Geometrie für eine spezifische Design-Wellenlänge fast vollständig unterdrückt werden, was zusammen mit dem opaken Goldspiegel zu einer Absorption von $A > 99\%$ im sichtbaren Spektralbereich führt.

Die nahe bei Null liegende Reflexion erlaubt fast hintergrundfreie Messungen an der Resonanz-Wellenlänge, wodurch schon kleine Wasserstoff-bedingte Modulationen der optischen Antwort des Systems zu großen relativen Änderungen der Reflexion führen. Die Nutzung einer optimierten Struktur mit diesen Eigenschaften erlaubte den zuverlässigen Nachweis von Wasserstoffkonzentrationen bis hinunter zu 0.5% in Stickstoff Trägergas.

Ein weiterer wichtiger Aspekt für den Einsatz perfekter Absorber im technologischen Umfeld ist die Winkelabhängigkeit der Absorption. Wünschenswert ist eine hohe Absorption über einen möglichst großen Winkelbereich, was größere Toleranzen in der Justage solcher optischer Elemente und somit eine verbesserte Stabilität ermöglicht.

Bei Anwendungen im Bereich der Photovoltaik oder der Bildgebung kann durch eine Vergrößerung des Winkelbereichs der Absorption ausserdem die Effizienz deutlich gesteigert werden, da das gesamte einfallende Licht genutzt werden kann.

Um die Prinzipien des winkelabhängigen Verhaltens in perfekten Absorbern zu untersuchen wurden umfangreiche winkelabhängigen Reflexions-Messungen an verschiedenen Absorber-Geometrien durchgeführt. Durch einen Vergleich dieser Messun-

gen mit numerischen Simulationen konnte ein Modell basierend auf optischer Impedanz-Anpassung entworfen werden, welches das winkelabhängige Verhalten perfekter Absorber physikalisch korrekt beschreibt.

Insbesondere wurde die perfekte Anpassung des Imaginärteils der optischen Impedanz an das umgebende Medium als bestimmender Faktor für winkelunabhängige Absorption identifiziert. Ausgehend von dieser neuen Design-Regel für perfekte Absorber mit regelmäßig angeordneten Elementen wurde das Modell in der Folge auf eine Absorber-Geometrie mit zufällig angeordneten plasmonischen Resonatoren angewendet und somit die Flexibilität des Ansatzes unterstrichen.

Abschließend konzentrierte sich die Arbeit auf die Realisierung schaltbarer plasmonischer Strukturen, deren spezifische optische Eigenschaften mittels eines externen Einflussfaktors stark beeinflusst werden können. Hierbei sind solche schaltbaren Strukturen von den bisher demonstrierten Sensor-Geometrien vor allem dadurch abgegrenzt, dass sich die optischen Eigenschaften sehr stark und zwischen zwei genau definierten Schaltzuständen ändern lassen.

Als erster Grundbaustein wurden hier plasmonische Nanoantennen bestehend aus Yttriumhydriden (YH_x) untersucht. Durch Variation der Wasserstoff-Konzentration in der Umgebung können diese Antennen von einem metallischen (Yttriumdihydrid) in einen dielektrischen Zustand (Yttriumtrihydrid) überführt werden, was mit einem vollständigen Verschwinden der plasmonischen Resonanz einhergeht.

Durch Erweiterung dieses Konzeptes auf Au/YH_x hybride Nanoantennen in Kombination mit einem Platin-Spiegel konnte ausserdem das Strukturdesign eines schaltbaren perfekten Absorbers entwickelt werden.

Trotz des guten Schaltkontrastes der hergestellten Strukturen zeigte sich, dass die Schaltzeiten zwischen den genannten Yttriumhydriden vergleichsweise niedrig waren. Speziell die Desorption des Wasserstoffs bei Wegnahme des umgebenden H_2 -Partialdrucks lief sehr langsam auf einer Zeitskala von Stunden ab, was YH_x -basierte Systeme ungeeignet für viele realistische technologische Anwendungen macht.

Um einen wirklich schaltbaren perfekten Absorber im Mittelinfraroten zu realisieren wurde als alternatives Material deshalb Germanium-Antimon-Tellurid (GST) untersucht. GST ist eine zentrale Materialkomponente in optischen Speichermedien und kann sowohl optisch als auch elektrisch zwischen zwei bei Raumtemperatur nicht volatilen Zuständen hin und her geschaltet werden. Weiterhin kann dieser Schaltprozess bis hinunter zu Nano- und Picosekunden-Zeitskalen durchgeführt werden.

Das untersuchte Absorberdesign bestand aus quadratischen Aluminium Nanoantennen über einer GST-326 Abstandsschicht und einem Aluminiumspiegel. Diese Anordnung erlaubte die experimentelle Realisierung einer Absorption $A > 90\%$ im mittelinfraroten Spektralbereich bei Wellenlängen von 3-5 μm . Durch die Flexibilität des Designs konnte die Wellenlängenposition der resonanten Absorption ausserdem leicht durch geometrische Variation der Nanoantennen-Seitenlänge geändert werden.

Die Grundlage des schaltbaren Verhalten der Anordnung bildete der reversible Übergang zwischen den amorphen und kristallinen Phasen von GST. Der Phasenübergang geht mit einer starken Änderung des Brechungsindex einher, was einen großen Schaltkontrast und eine starke spektrale Verschiebung der mittelinfraroten Absorptionsbande der Anordnung ermöglichte. Diese starke optische Modulation beim Phasenübergang erlaubte das vollständige Schalten der Struktur zwischen zwei spektral getrennten Mittelinfrarot-Absorptionsbanden.

Wenn ein solcher schaltbarer Absorber in bildgebenden Detektoren im Mittelinfraroten integriert wird, ermöglicht er die Differenzierung von Objekten mit verschiedenen Temperaturen und kann somit für neue Anwendungen in der Materialprüfung oder der Astronomie eingesetzt werden.

Ausgehend von den in der vorliegenden Arbeit entwickelten Konzepten gibt es zahlreiche zukünftige Forschungsrichtungen, in denen hybride plasmonische Strukturen eine zentrale Rolle spielen können.

So können beispielsweise die Au@SiO₂ Nanosensor-Partikel verwendet werden um katalytische Prozesse auf ausgedehnten reaktiven Materialien orts aufgelöst zu beobachten. Hierzu werden die Nanosensoren netzartig auf der zu untersuchenden Ober-

fläche verteilt und ihre zeitaufgelöste optische Antwort während eines katalytischen Prozesses für alle Partikel in einem bestimmten Sichtfeld simultan gemessen.

Durch Vergleich dieser "Reaktionskarte" der Oberfläche mit Elektronen- bzw. Rasterkraftmikroskop-Aufnahmen kann dann der Einfluss lokalisierter Defekte, Risse oder Verwerfungen auf die Effizienz der katalytischen Reaktionen quantifiziert werden. Die hieraus entnommenen Erkenntnisse könnten dann einen wichtigen Beitrag für das Verständnis und die Entwicklung neuartiger Katalysatoren in Forschung und Industrie leisten.

Weiterhin können die gezeigten DNA-basierten Nanosensoren für die Verwendung neuer funktioneller bzw. chemisch sensitiver Materialien erweitert werden, was den Nachweis anderer signifikanter Stoffe und Spurengase ermöglichen würde. Ausserdem kann der Einsatz dieser hybriden Nanopartikel in biologischen Systemen untersucht werden, mit dem Ziel der flexiblen und komplett optischen Überwachung chemischer Reaktionen in Lebewesen potentiell bis hinunter zu Mikroorganismen.

Schließlich bildet das Konzept eines schaltbaren plasmonischen Elements im Mittelinfraroten einen idealen Ausgangspunkt für die Realisierung einer Anordnung zur orts aufgelösten Beeinflussung der Amplitude und Phase einfallenden Lichts. Ein solcher räumlicher Modulator für Licht ("spatial light modulator", SLM) wurde im Mittelinfraroten bislang nicht realisiert und würde somit eine wichtige technologische Lücke im Bereich der adaptiven Optik und für Anwendungen in der Astronomie und der optischen Datenübertragung ausfüllen.

Kernbestandteil einer solchen Anordnung ist eine hybride plasmonische Oligomer-Struktur, deren optische Antwort ein breites lorentzförmiges Absorptionsband mit einem spektral schärferen Transmissions-Fenster aufweist. Eine solche Fano-resonante Anordnung erlaubt die simultane Realisierung von hoher Transmission im Mittelinfraroten und starker Modulation der Phase in einem bestimmten Wellenlängenbereich. Kombiniert mit einer benachbarten GST-Schicht könnte somit die Amplitude und Phase des einfallenden Lichts über externe Impulse beeinflusst und aktiv geschaltet werden.

Unterteilt man eine solche aktive plasmonische Oberfläche in einzeln ansteuerbare Pixel, kann die Amplitude und Phase des einfallenden Lichts schließlich ortsabhängig beeinflusst werden.

Durch die einzigartige Kombination von hohen optischen Modulationen und geringen Strukturgrößen können hybride plasmonische Systeme zukünftig eine zentrale Rolle bei der Entwicklung miniaturisierter optischer Gerätschaften spielen. Die potentiellen Anwendungen für solche Nanophotonik-basierten Anordnungen sind vielfältig, angefangen von hochsensitiven Sensoren bis hin zur Bündelung von Energie für effiziente neuartige Katalysatoren.

PUBLICATIONS

Parts of this thesis have already been published:

- (P1) **A. Tittl**, P. Mai, R. Taubert, D. Dregely, N. Liu, and H. Giessen, *Palladium-Based Plasmonic Perfect Absorber in the Visible Wavelength Range and Its Application to Hydrogen Sensing*, *Nano Letters* **11**, 4366-4369 (2011).
- (P2) **A. Tittl**, C. Kremers, J. Dorfmueller, D. N. Chigrin, and H. Giessen, *Spectral shifts in nanoantenna-enhanced hydrogen sensors*, *Optical Materials Express* **2**, 111-118 (2012).
- (P3) **A. Tittl**, X. Yin, H. Giessen, C. Kremers, D. N. Chigrin, X.-Q. Tian, Z.-Q. Tian, and N. Liu, *Plasmonic smart dust for probing local chemical reactions*, *Nano Letters* **13**, 1816-1821 (2013).
- (P4) N. Strohfelddt, **A. Tittl**, M. Schäferling, F. Neubrech, U. Kreibig, R. Griessen, and H. Giessen, *Yttrium Hydride Nanoantennas for Active Plasmonics*, *Nano Letters* **14**, 1140-1147 (2014).
- (P5) **A. Tittl**, H. Giessen, and N. Liu, *Plasmonic gas and chemical sensing (review paper)*, *Nanophotonics* **3**, 157-180 (2014).
- (P6) **A. Tittl**, M. G. Harats, R. Walter, X. Yin, M. Schäferling, N. Liu, R. Rapaport, and H. Giessen, *Quantitative Angle-Resolved Small-Spot Reflectance Measurements on Plasmonic Perfect Absorbers: Impedance Matching and Disorder Effects*, *ACS nano* **8**, 10885-10892 (2014).
- (P7) N. Li*, **A. Tittl***, S. Yue, H. Giessen, C. Song, B. Ding, and N. Liu *equal contribution, *DNA-assembled bimetallic plasmonic nanosensors*, *Light: Science & Applications* **3**, e226 (2014).

-
- (P8) **A. Tittl**, A.-K. U. Michel, M. Schäferling, X. Yin, B. Gholipour, L. Cui, M. Wuttig, T. Taubner, F. Neubrech, and H. Giessen, *A switchable mid-infrared plasmonic perfect absorber with multi-spectral thermal imaging capability*, *Advanced Materials*, DOI: 10.1002/adma.201502023 (2015).

Additional scientific publications not presented in this thesis:

- (P9) N. Strohfeldt, **A. Tittl**, and H. Giessen, *Long-term stability of capped and buffered palladium-nickel thin films and nanostructures for plasmonic hydrogen sensing applications*, *Optical Materials Express* **3**, 194-204 (2013).
- (P10) R. Walter, **A. Tittl**, A. Berrier, and H. Giessen, *Large-area low-cost tunable plasmonic perfect absorber in the near-infrared by colloidal etching lithography*, *Advanced Optical Materials* **3**, 398-403 (2015).
- (P11) X. Yin, M. Schäferling, A.-K. U. Michel, **A. Tittl**, M. Wuttig, T. Taubner, and H. Giessen, *Active chiral plasmonics*, *Nano Letters* **15**, 4255-4260 (2015).

Conference contributions as presenting author:

- (C1) *Perfect Absorber Hydrogen Sensor*, Spring Meeting of the German Physical Society, Regensburg, Germany (2010).
- (C2) *Plasmonic sensors based on perfect absorption*, SPIE Optics + Photonics 2010, San Diego, USA.
- (C3) *Palladium-based perfect plasmonic absorber in the visible and its application to hydrogen sensing*, NANOMETA 2011 – 3rd International Topical Meeting on Nanophotonics and Metamaterials, Seefeld, Austria (2011).
- (C4) *Palladium-based perfect plasmonic absorber in the visible and its application to hydrogen sensing*, Spring Meeting of the German Physical Society, Dresden, Germany (2011).

-
- (C5) *Palladium-based perfect plasmonic absorber in the visible and its application to hydrogen sensing*, Summer school “Plasmonics, Functionalization and Biosensing”, Heidelberg, Germany (2011).
- (C6) *Palladium-Based Plasmonic Perfect Absorber in the Visible Wavelength Range and Its Application to Hydrogen Sensing*, Summer school “Nano-Antennas”, Bad Honnef, Germany (2011).
- (C7) *Spectral Shifts in Optical Nanoantenna-Enhanced Hydrogen Sensors*, Spring Meeting of the German Physical Society, Berlin, Germany (2012).
- (C8) *Palladium-Based Plasmonic Hydrogen-Sensing: Perfect Absorbers and Antenna-Enhanced Geometries*, MRS 2012 Spring Meeting, San Francisco, USA (2012).
- (C9) *Palladium-Based Plasmonic Hydrogen-Sensing: Perfect Absorbers and Antenna-Enhanced Geometries*, META 2012 – 3rd International Conference on Metamaterials, Photonic Crystals and Plasmonics, Paris, France (2012).
- (C10) *Systematic Study of the Hydrogen-Sensing Performance of Buffered and Capped Pd and PdNi Layers for Plasmonic Applications*, E-MRS 2012 Spring Meeting, Strasbourg, France (2012).
- (C11) *Perfect Absorber Sensor: Towards Single Catalytic Detection*, Nanofair 2012 – 9th International Nanotechnology Symposium, Dresden, Germany (2012).
- (C12) *Plasmonic smart dust for probing local chemical reactions*, META 2013 – 4th International Conference on Metamaterials, Photonic Crystals and Plasmonics, Sharjah, Dubai, United Arab Emirates (2013).
- (C13) *Plasmonic smart dust for probing local chemical reactions*, SPIE Optics + Photonics 2013, San Diego, USA (2013).
- (C14) *CMOS-compatible switchable plasmonic perfect absorber in the mid-infrared*, WE Heraeus seminar on active plasmonics and metamaterial dynamics, Bad Honnef, Germany (2014).

-
- (C15) *CMOS-compatible switchable plasmonic perfect absorber*, Spring Meeting of the German Physical Society, Dresden, Germany (2014).
- (C16) *CMOS-compatible switchable plasmonic perfect absorber in the mid-infrared*, META 2014 – 5th International Conference on Metamaterials, Photonic Crystals and Plasmonics, Singapore (2014).
- (C17) *Bimetallic plasmonic nanosensors: DNA self-assembly and core-shell nanocrystals*, Spring Meeting of the German Physical Society, Berlin, Germany (2015).

Additional conference contributions as co-author:

- (C18) *Systematic study of the hydrogen-sensing performance of buffered and capped Pd and PdNi layers for plasmonic applications*, META 2012 – 3rd International Conference on Metamaterials, Photonic Crystals and Plasmonics, Paris, France (2012).
- (C19) *Long-term stability of capped and buffered PdNi films and nanostructures for plasmonic hydrogen-sensing applications*, ICMAT 2013, Singapore (2013).
- (C20) *Yttrium hydride nanoantennas for reconfigurable plasmonics*, WE Heraeus seminar on active plasmonics and metamaterial dynamics, Bad Honnef, Germany (2014).
- (C21) *Origin of the huge asymmetry in ab- and desorption kinetics of hydrogen in capped films*, 14th International Symposium on Metal Hydrogen Systems, University of Salford, United Kingdom (2014).
- (C22) *Yttrium hydride nanoantennas for reconfigurable plasmonics*, Gordon Research Conference on Plasmonics, Newry, Maine, USA (2014).
- (C23) *Yttrium hydride nanoantennas for active plasmonics*, SPIE Optics + Photonics 2014, San Diego, USA (2014).

-
- (C24) *Large-area low-cost Palladium based plasmonic Perfect Absorber for Hydrogen Sensing*, NANOMETA 2015 – 5th International Topical Meeting on Nanophotonics and Metamaterials, Seefeld, Austria (2015).
- (C25) *Active mid-IR plasmonic metasurfaces: Tunable and switchable chirality and flat-surface beam steering*, Spring Meeting of the German Physical Society, Berlin, Germany (2015).
- (C26) *Sensitivity engineering in direct contact Au@Pd nano-sandwich hydrogen sensors*, Spring Meeting of the German Physical Society, Berlin, Germany (2015).
- (C27) *Magnesium for UV plasmonics and chemical reaction sensing*, Spring Meeting of the German Physical Society, Berlin, Germany (2015).
- (C28) *Large-area spectrally selective plasmonic perfect absorber sensor fabricated by laser interference lithography*, Spring Meeting of the German Physical Society, Berlin, Germany (2015).
- (C29) *Plasmonic copper nanostructures for monitoring electrochemical redox-reactions*, Spring Meeting of the German Physical Society, Berlin, Germany (2015).
- (C30) *Active mid-IR plasmonic metadevices*, META 2015 – 6th International Conference on Metamaterials, Photonic Crystals and Plasmonics, New York, USA (2015).

CONTENTS

1	INTRODUCTION	1
2	PLASMONIC THEORY FOR SENSING AND ACTIVE CONTROL	5
2.1	Basic equations of electrodynamics	5
2.2	Dynamics of conduction electrons	7
2.3	Resonant plasmonic systems	9
2.3.1	Surface plasmon resonances	9
2.3.2	Localized surface plasmon resonances	11
2.4	Plasmonic perfect absorbers	17
2.5	Materials for hybrid plasmonic devices	19
2.5.1	The palladium-hydrogen system	19
2.5.2	Yttrium and yttrium hydrides	21
2.5.3	Phase-change materials for active plasmonics	23
3	INTRODUCTION TO PLASMONIC GAS AND CHEMICAL SENSING	27
3.1	Thin films with embedded plasmonic particles	32
3.2	Engineered nanoparticles and smart dust	42
3.3	Large-area nanostructured sensor chips	49
3.4	Complex grating-based plasmonic hydrogen sensors	53
3.5	Antenna-enhanced sensor geometries	57
4	SINGLE PLASMONIC NANOPROBES FOR TRACE GAS DETECTION	63
4.1	Antenna-enhanced hydrogen sensors	63
4.2	Plasmonic smart dust nanoprobcs	73
4.3	DNA-assembled bimetallic nanosensors	86

5	PERFECT ABSORBERS FOR SENSING AND ACTIVE PLASMONICS	97
5.1	Palladium-based perfect absorber sensor	97
5.2	Impedance matching in plasmonic perfect absorbers	105
5.3	Yttrium for reconfigurable antennas and absorbers	121
5.4	Switchable perfect absorber for thermal imaging . .	130
6	CONCLUSIONS & OUTLOOK	147
	BIBLIOGRAPHY	152
	ACKNOWLEDGMENTS	179

INTRODUCTION

In the last decade, plasmonics has developed into an expansive and vibrant field, with applications as diverse as negative refraction, enhanced photovoltaics, and targeted drug delivery¹⁻³.

This remarkable progress has been driven by major advances in the fabrication of nanostructured systems, including both “top-down” approaches such as electron-beam or nanoimprint lithography as well as “bottom-up” techniques like nanosphere lithography and chemical synthesis⁴⁻⁶. The unprecedented ability to structure metals and dielectrics on the nanoscale has allowed plasmonics to move from giga- and terahertz into the near-infrared and visible spectral ranges.

Since the response of plasmonic structures in the optical range allows for remote and non-invasive read-out using standard optical spectroscopy, this transition has also been a crucial driving factor for the field of plasmonic sensing⁷⁻¹¹.

In general, plasmonic device concepts rely on the ability of small metal particles to concentrate incident light into deep sub-wavelength volumes. This behavior is due to the collective oscillations of the conduction electrons against the restoring force of the positively charged nuclei, which can be resonantly driven by an external electromagnetic field¹². The spectral behavior of such plasmonic resonances (specifically the scattering and absorption cross-sections) can be calculated analytically only for geometrically simple systems, such as subwavelength gold spheres in an isotropic medium. For more complex systems, the plasmon resonance position and lineshape are highly dependent on material composition, nanoscale geometry, and dielectric environment of the nanostructure¹³.

Initial experiments in plasmonics research have focused on noble metal nanoparticles, starting from investigations of simple sphere- and rod-type structures and moving towards coupled arrangements of nanoparticles in two and three dimensions. Such

complex coupled nanoparticle geometries can exhibit remarkable optical properties such as perfect absorption¹⁴, the plasmonic analogue of electromagnetically induced transparency¹⁵, or circular dichroism¹⁶.

However, in a push towards novel applications, plasmonics requires a shift from widely used but passive metals such as silver or gold towards novel materials systems. Integrating such materials into hybrid plasmonic devices allows for additional degrees of freedom in structure design and can add new functionality to known systems.

Utilizing various complex nanoplasmonic devices, this thesis pursues two complementary threads of research, covering the technological scale from fundamental science to applications.

On the one hand, it focuses on the development of chemically synthesized hybrid plasmonic nanosensors, which combine an efficient optical probe with a chemically sensitive material to enable novel sensing applications. By performing optical measurements on individual plasmonic nanoprobles, it aims to detect reagents in progressively smaller sensing volumes, with the ultimate goal of observing chemical and catalytic reactions involving only a few molecules.

On the other hand, it studies plasmonic perfect absorber structures, optical elements designed to absorb all radiation of a certain wavelength, which have shown promise for a variety of technological applications. Here, the focus is on both developing a theoretical model for the optical behavior of plasmonic perfect absorber structures, as well as on the experimental realization of efficient gas sensors and active mid-infrared imaging devices.

As a theoretical primer, chapter 2 presents some of the fundamental scientific concepts for describing and understanding the behavior of hybrid plasmonic nanostructures. This includes a general discussion of the electrostatics of metal/dielectric interfaces and metal nanoparticles as well as an overview of the material systems used in the presented sensor and imaging devices.

Chapter 3 gives a brief overview of the field of plasmonic gas and chemical sensing, covering a range of detection con-

cepts from plasmonically-functionalized thin films to highly engineered nanostructures.

Chapter 4 focuses on single plasmonic nanoprobes for trace gas detection, especially using increasingly complex chemically grown plasmonic nanoprobes, often referred to as “smart dust”.

Chapter 5 discusses the the theoretical modeling and experimental realization of various plasmonic perfect absorber devices. Topics covered include the development of an impedance-matching model for the optical properties of perfect absorbers particularly at high incident angles, as well as applications ranging from hydrogen sensing to active infrared imaging.

In chapter 6, the main results of the thesis are summarized, and a short outlook on how future hybrid plasmonic devices can build on the presented concepts is given.

THEORY OF PLASMONIC DEVICES FOR SENSING AND ACTIVE CONTROL

This chapter outlines some of the theory of plasmonic devices for sensing and active control. It focuses first on the basic equations governing the interaction of light with plasmonic systems, namely Maxwell's equations and the Drude model for the dynamics of conduction electrons. Building on this, surface plasmon and localized surface plasmon resonances are discussed. After a brief description of the working principle of plasmonic perfect absorbers, some material systems for hybrid plasmonic devices are introduced.

A description of basic electrodynamic principles and plasmonic systems can be found in a variety of textbooks. This introductory chapter follows the line of argument in Ref.¹², with some parts adapted from Ref.¹⁷.

2.1 BASIC EQUATIONS OF ELECTRODYNAMICS

Maxwell's equations form the theoretical foundation of optics and electrodynamics. In vacuum and using SI units, they are commonly written as

$$\operatorname{div} \mathbf{E} = \frac{\rho}{\varepsilon_0} \quad (2.1)$$

$$\operatorname{div} \mathbf{B} = 0 \quad (2.2)$$

$$\operatorname{rot} \mathbf{E} = -\frac{\partial \mathbf{B}}{\partial t} \quad (2.3)$$

$$\operatorname{rot} \mathbf{B} = \mu_0 \mathbf{j} + \mu_0 \varepsilon_0 \frac{\partial \mathbf{E}}{\partial t} \quad (2.4)$$

where bold symbols denote vector quantities and ε_0 and μ_0 are the electric permittivity and magnetic permeability of vacuum, respectively.

These equations link the electric field \mathbf{E} and the magnetic field \mathbf{B} at a any given point in space with the corresponding charge density ρ and current density \mathbf{j} . Since electric charge is conserved in any closed volume, we also require

$$\operatorname{div} \mathbf{j} + \frac{\partial \rho}{\partial t} = 0. \quad (2.5)$$

Two straightforward solutions of Maxwell's equations are plane waves of the electric and magnetic fields of the form

$$\mathbf{E}(t) = \mathbf{E}_0 \cdot e^{i(\mathbf{k}\mathbf{r} - \omega t)} \quad \mathbf{B}(t) = \mathbf{B}_0 \cdot e^{i(\mathbf{k}\mathbf{r} - \omega t)} \quad (2.6)$$

where \mathbf{k} is the propagation vector of the wave, ω is its angular frequency, and the vectors \mathbf{E}_0 and \mathbf{B}_0 are linked by the relation $\omega \mathbf{B}_0 = \mathbf{k} \times \mathbf{E}_0$.

The analysis of electric and magnetic fields becomes somewhat more complicated when introducing a medium. In the following, we will focus on the simplest case of a linear, nonmagnetic and isotropic medium. Consequently, such a medium can be described as an arrangement of microscopic dipoles, which can be aligned in an applied external electric field.

This polarization in the material leads to the formation of an internal charge density ρ_{int} , which needs to be included in addition to the external charge density ρ in Maxwell's equation for the divergence of the electric field. This leads to

$$\operatorname{div} \mathbf{E} = \frac{\rho + \rho_{\text{int}}}{\epsilon_0} = \frac{\rho_{\text{tot}}}{\epsilon_0}. \quad (2.7)$$

The internal charge density is further related to the electric dipole moment per unit volume \mathbf{P} via $\operatorname{div} \mathbf{P} = -\rho_{\text{int}}$. Putting these two observations together, one obtains

$$\epsilon_0 \operatorname{div} \mathbf{E} + \operatorname{div} \mathbf{P} = \operatorname{div} (\epsilon_0 \mathbf{E} + \mathbf{P}) = \operatorname{div} \mathbf{D} = \rho \quad (2.8)$$

where \mathbf{D} is the dielectric displacement given by

$$\mathbf{D} = \epsilon_0 \mathbf{E} + \mathbf{P}. \quad (2.9)$$

This argument also holds for the magnetic material response, where the magnetic field \mathbf{H} can be introduced via

$$\mathbf{H} = \frac{1}{\mu_0} \mathbf{B} - \mathbf{M} \quad (2.10)$$

with magnetization \mathbf{M} . Since we assume a linear ($\mathbf{P} \sim \mathbf{E}$), nonmagnetic ($\mathbf{M} = 0$) and isotropic medium, this reduces to

$$\mathbf{D} = \varepsilon_0 \varepsilon \mathbf{E} \quad (2.11)$$

$$\mathbf{B} = \mu_0 \mu \mathbf{H} \quad (2.12)$$

with relative permittivity ε and relative permeability μ (in the nonmagnetic case $\mu = 1$).

Maxwell's equations in a linear, nonmagnetic, and isotropic medium can now be written as

$$\operatorname{div} \mathbf{D} = \rho \quad (2.13)$$

$$\operatorname{div} \mathbf{B} = 0 \quad (2.14)$$

$$\operatorname{rot} \mathbf{E} = -\frac{\partial \mathbf{B}}{\partial t} \quad (2.15)$$

$$\operatorname{rot} \mathbf{H} = \mathbf{j} + \frac{\partial \mathbf{D}}{\partial t}. \quad (2.16)$$

These equations contain all four macroscopic fields and link them with the external charge and current densities. Finding solutions for the complex boundary conditions of metal-dielectric nanoscale systems is a key challenge in plasmonics research.

2.2 DYNAMICS OF CONDUCTION ELECTRONS

Compared to the study of simple dielectric materials, the electrodynamic treatment of metals is more complex. One key difference is the presence of conduction electrons in the metal, which can interact with an incident electric field.

A straightforward description of this interaction is found in the Drude model, which assumes a cloud of conduction electrons freely moving against a fixed background lattice of positively charged ions. These electrons do not interact with each

other and their only contacts with the lattice are elastic collisions happening at a specific frequency $\gamma = 1/\tau$, where τ is the characteristic relaxation rate of the electron gas.¹³

Due to these simplifications, the Drude model ignores quantum effects and the detailed electronic band structure. However, it can still yield sufficient results for alkali metals and, in spectral regions where interband-transitions are absent, noble metals like platinum, gold and palladium.

The dynamics of this system can now be calculated by introducing a periodic external electric field \mathbf{E}_{ext} . Importantly, we consider the conduction electrons as harmonic oscillators driven by the external electric field. Assuming no electrostatic interaction between the background lattice of ions and the electrons ('free electron model'), the equation of motion for the electrons becomes

$$m\ddot{\mathbf{x}}(t) + m\gamma\dot{\mathbf{x}}(t) = -e \cdot \mathbf{E}_{\text{ext}}(t). \quad (2.17)$$

In optical systems, we can assume that the time-dependence of the electric field is harmonic and can simply be written as $E_{\text{ext}} = E_0 \cdot e^{-i\omega t}$. After an initial relaxation time, the frequency of an harmonic oscillator will be equal to the frequency of the driving force, which leads to the ansatz $\mathbf{x}(t) = \mathbf{x}_0 \cdot e^{-i\omega t}$. This links the oscillator amplitude \mathbf{x} to the incident field via

$$\mathbf{x}(t) = \frac{e}{m(\omega^2 + i\gamma\omega)} \mathbf{E}_{\text{ext}}(t). \quad (2.18)$$

Going back to a macroscopic picture, these oscillator amplitudes lead to a material polarization $\mathbf{P} = -nex$ where n is the density of the conduction electrons. The magnitude of this polarization is frequency dependent and given by

$$\mathbf{P} = -\frac{ne^2}{m(\omega^2 + i\gamma\omega)} \mathbf{E}_{\text{ext}}(t). \quad (2.19)$$

Combined with Maxwell's equations in matter, this relation can be used to obtain the complex dielectric function of the free electron gas

$$\varepsilon(\omega) = 1 - \frac{\omega_p^2}{\omega^2 + i\gamma\omega} \quad (2.20)$$

where ω_p is the plasma frequency of system given by

$$\omega_p^2 = \frac{ne^2}{\epsilon_0 m} \quad (2.21)$$

and m is the electron mass. A metal with these properties is also referred to as an ideal metal. $\epsilon(\omega)$ can be separated into real and imaginary parts via $\epsilon(\omega) = \epsilon_1(\omega) + i\epsilon_2(\omega)$ to obtain

$$\epsilon_1(\omega) = 1 - \frac{\omega_p^2}{\gamma^2 + \omega^2} \quad \epsilon_2(\omega) = \frac{\omega_p^2 \gamma}{\omega \gamma^2 + \omega^3}. \quad (2.22)$$

From this, it is straightforward to calculate the complex refractive index $N = n + i\kappa = \sqrt{\epsilon}$ using

$$n^2 = \frac{\epsilon_1}{2} + \frac{1}{2} \sqrt{\epsilon_1^2 + \epsilon_2^2} \quad \kappa = \frac{\epsilon_2}{2n}. \quad (2.23)$$

This leads to a more descriptive picture, since n directly determines the propagation speed of an electromagnetic wave in the material and κ is directly proportional to the absorption coefficient $\alpha = 2\kappa\omega/c$ that enters Beer's law via $I(x) = I_0 e^{-\alpha x}$.

In summary, the Drude model can be used to describe the frequency dependent dielectric properties of many metals (in spectral regions where no interband transitions occur) using only two parameters, the plasma frequency ω_p and the damping constant γ . Compared to the use of tabulated dielectric data, this simplified description can significantly speed up analytical and especially numerical calculations of the optical properties of plasmonic systems.

2.3 RESONANT PLASMONIC SYSTEMS

2.3.1 Surface plasmon resonances

Surface plasmon resonances (SPRs) are oscillations of the free electron gas confined to a metal-dielectric interface and driven by an external electric field. They can be described as a propagating electromagnetic wave along the interface that simultaneously exhibits exponential decay perpendicular to it. Specifically, we

consider a nonabsorbing dielectric half space (dielectric function ϵ_d) on top of a metal half space (dielectric function ϵ_m given by the Drude model), as shown in Fig. 2.1.

The goal of the numerical analysis of such a system is to find propagating solutions in x -direction, derived from the electromagnetic wave equation in matter

$$\nabla^2 \mathbf{E} - \frac{\epsilon}{c^2} \frac{\partial^2 \mathbf{E}}{\partial t^2}. \quad (2.24)$$

The calculation of the full spatially resolved electric field $\mathbf{E}(x, z)$ is complex and additional details can be found in many books on nanophotonics.¹² One fundamental result is the strong enhancement of the fields close to the metal/dielectric interface found in such systems (see Fig. 2.1).

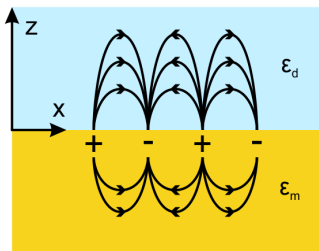


Figure 2.1: The electric field lines of surface plasmon mode propagating with a wave vector parallel to the x -axis. Note the surface charge wave at the metal/dielectric interface and the high density of electric field lines (i.e., the strong field enhancement).

We now examine the relation between the frequency ω of the incident electromagnetic plane wave and the wave vector k_x of the propagating surface plasmon wave. This dispersion relation is given by

$$k_x = \frac{\omega}{c} \sqrt{\frac{\epsilon_d \epsilon_m}{\epsilon_d + \epsilon_m}} \quad (2.25)$$

and visualized for different refractive indices of the dielectric half-space in Fig. 2.2.

The surface plasmon dispersion relation usually lies to the right of the respective light line. This means, that surface plas-

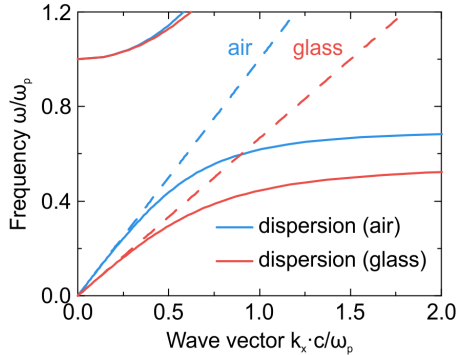


Figure 2.2: Dispersion relations of a propagating surface plasmon at metal/air and metal/glass interfaces. The dashed lines are the respective light-lines.

mons cannot simply be excited by shining light on the metal/dielectric interface since there is a substantial mismatch between the incident and SPR wave vectors. This can be overcome by introducing additional vector components using, e.g., grating or prism couplers.

SPR-based optical devices have found a variety of applications, chiefly in the field of sensing. Because of the high electric fields at the metal/dielectric interface, the SPR is very sensitive to environmental refractive index changes in the vicinity of the metal surface.

However, sensing geometries based on surface plasmon resonances usually require extended metal/dielectric interfaces. This imposes a lower limit on the detection of small amounts and concentrations of a given sensing agent. In order to reach sensing volumes in the range of attoliters, it is crucial to move to a system where the electromagnetic fields are confined in more than one dimension: localized surface plasmon resonances.

2.3.2 Localized surface plasmon resonances

In contrast to propagating plasmonic surface waves, sub-wavelength metal nanoparticles can support plasmonic oscillations with much stronger confinement of the electromagnetic energy.

These localized surface plasmon resonances (LSPRs) maintain the large field enhancement and refractive index sensitivity of SPR geometries, and can be excited using free space illumination.

The large coupling between light and a nanoscale structure combined with strong field-enhancement and many design possibilities makes localized surface plasmon resonances ideal candidates for sensing applications.^{9,14} Depending on the specific nanophotonic device, many different sizes and shapes of metal nanoparticles can be used, ranging from simple spheres to complex arrangements of triangular or even fractal nanoparticles.⁸

Metal nanoparticles used in plasmonic devices are commonly sub-wavelength. To further simplify the numerical analysis, we can assume that the characteristic size d of the particle is much smaller than the wavelength λ of the incident light. Consequently, the electric field acting on the conduction electrons can be taken as constant over the entire particle, leading to the so called quasi-static approximation.

Quasi-static approximation

Let us first consider a simple system that can still be solved analytically: a metal sphere characterized embedded in a nonabsorbing medium with a given dielectric constant (see Fig. 2.3). Due to symmetry considerations, it is best to describe this system in spherical coordinates.

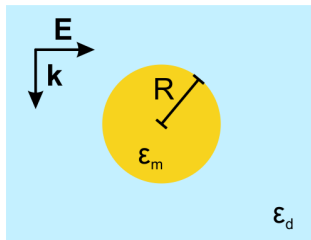


Figure 2.3: Schematic of a localized surface plasmon geometry: a metal sphere embedded in a nonabsorbing dielectric.

Furthermore, since $d \ll \lambda$ we can assume that the strength of the incident electric field acting on the particle does not vary spatially over its volume. Put differently, at a given time every point of the particle experiences the same external field.

The optical properties of the particle can then be derived by expanding the incident and scattered fields in spherical harmonics and fixing their expansion coefficients in a way that satisfies the boundary conditions of the system.⁸

Since the conduction electrons oscillate collectively against a stationary background of positive ions, the resonance has dipolar character. Due to the sub-wavelength character of the problem, we can describe the oscillation like a point dipole fixed at the spheres center with dipole moment

$$\mathbf{p} = 4\pi\epsilon_0\epsilon_d R^3 \frac{\epsilon_m - \epsilon_d}{\epsilon_m + 2\epsilon_d} \mathbf{E} \quad (2.26)$$

where R is the radius of the sphere and \mathbf{E} the incident electric field. This can be expressed in a more concise way by introducing the polarizability

$$\alpha = 4\pi R^3 \frac{\epsilon_m - \epsilon_d}{\epsilon_m + 2\epsilon_d} \quad (2.27)$$

and writing $\mathbf{p} = \epsilon_0\epsilon_d\alpha\mathbf{E}$. As evident from (2.26) and (2.27), both the polarizability and the dipole exhibit resonant character and reach their peak values when $|\epsilon_m + 2\epsilon_d|$ becomes minimal.

If we now assume a metal with vanishing losses ($\text{Im}(\epsilon_m) \approx 0$), the resonance condition becomes $\text{Re}(\epsilon_m) = -2\epsilon_d$. By inserting the Drude model for ϵ_m we obtain a simple expression for the dipole resonance frequency ω_{LSPR} of a spherical metal nanoparticle in the quasistatic limit:

$$\omega_{\text{LSPR}} = \frac{\omega_p}{\sqrt{1 + 2\epsilon_d}} \quad (2.28)$$

where ω_p is the plasma frequency of the metal.

The strong field enhancement in LSPR-based systems becomes evident when looking at the expressions for the electric field inside and outside of the spherical metal nanoparticle

$$\mathbf{E}_{\text{in}} = \frac{3\varepsilon_d}{\varepsilon_m + 2\varepsilon_d} \mathbf{E} \quad (2.29)$$

$$\mathbf{E}_{\text{out}} = \mathbf{E} + \frac{3\mathbf{n}(\mathbf{n} \cdot \mathbf{p}) - \mathbf{p}}{4\pi\varepsilon_0\varepsilon_d} \frac{1}{r^3} \quad (2.30)$$

where \mathbf{n} is the unit vector in the direction of the point of interest. Both fields show resonant behavior similar to the polarizability α , which makes such nanoparticle system highly sensitive to refractive index changes in their environment.

Size effects and retardation

In realistic plasmonic systems, the constituent particles are often larger than the limit for the quasi-static approximation (particle size $\gg 10$ nm) and a constant electric field over the whole particle can no longer be assumed.

The incorporation of electric fields with varying phase over the particle complicates the electrodynamic treatment of plasmonic systems. The first solution to this problem for a metal sphere in a dielectric medium was given by Mie¹⁸ to account for the optical properties of colloidal solutions.

This approach again expands the incident and scattered fields in spherical harmonics, this time taking retardation effects into account, and fixes their expansion coefficients in a way that satisfies the boundary conditions at the metal/dielectric interface.

To the first order corrections, the polarizability becomes

$$\alpha_{\text{Mie}} = 4\pi R^3 \frac{1 - \frac{1}{10}(\varepsilon_m + \varepsilon_d)\zeta^2}{\left(1 + \frac{3\varepsilon_d}{\varepsilon_m - \varepsilon_d}\right) - \frac{1}{10}(\varepsilon_m + 10\varepsilon_d)\zeta^2 - i\frac{16}{3}\varepsilon_d^{3/2}\zeta^3} \quad (2.31)$$

where $\zeta = \pi R/\lambda_0$ is the size parameter and λ_0 the free-space wavelength of the incident light.¹⁹ The influence of the size parameter (and thus the radius) on the polarizability can be seen in Fig. 2.4.

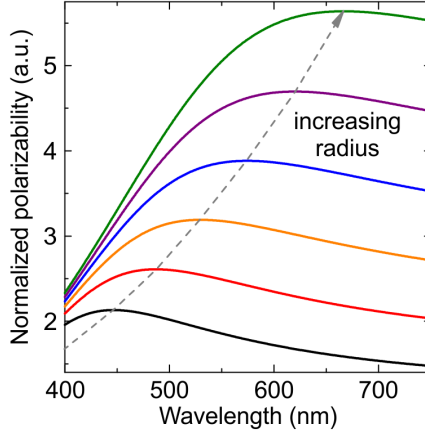


Figure 2.4: Results of Mie's theory for the polarizability of a gold sphere embedded in a dielectric medium. ω_p and γ were taken from literature²⁰ and the medium was assumed to be water with $n = 1.333$.

The resonance clearly redshifts and broadens for increased particle radius. In addition, the magnitude of the polarizability increases. In comparison to the quasi-static picture in (2.27), where the resonance position was independent of the particle radius and only influenced by the dielectric environment, (2.31) provides a more physical picture of the plasmonic resonance.

These conclusions are also helpful for the discussion of optical spectra of metal particles, since the polarizability α is directly related to the scattering and absorption cross-sections via

$$\begin{aligned} C_{\text{sca}} &= \frac{k^4}{6\pi} |\alpha|^2 \\ C_{\text{abs}} &= k \text{Im}(\alpha) \end{aligned} \quad (2.32)$$

where k is the wave vector of the incident light.

Plasmonic lifetimes

In order to understand why the localized surface plasmon resonance of a metal sphere broadens with increasing radius, we need to examine the role of damping in plasmonic systems. There are

two main sources of damping: radiative damping due to scattering of photons into the far-field and non-radiative damping caused by absorption.¹³

Since scattering cross-section and absorption cross-section scale with $C_{\text{sca}} \sim R^6$ and $C_{\text{abs}} \sim R^3$ according to (2.32), non-radiative damping is the leading influence for small particle sizes in the 10 nm range whereas radiative damping becomes dominant for larger (size > 100 nm) particles.

NON-RADIATIVE DAMPING When a metallic nanoparticle is excited by incident light, energy is transferred to oscillations of conduction electrons in the system. These oscillations experience damping due to electron scattering or intra-band transition effects, leading to increased damping of the resonance as a whole. Ohmic losses in the metal also contribute heavily to the non-radiative part of the damping.

RADIATIVE DAMPING For sufficiently small metal particles, the far-field optical properties of the localized plasmon resonance can be modeled as a simple electric dipole. Consequently, the plasmonic particle is able to efficiently emit light into the far-field, which reduces the effective number of oscillating electrons and in turn causes damping. Due to the increase of oscillator strength with particle size, radiative effects are the main reason for the strong increase in damping for larger particles observed in Fig. 2.4.

Both radiative and non-radiative effects can be described by introducing an electron dephasing time T_φ to model the breakdown of the coherent plasmon oscillation over time. The dephasing time is related to the linewidth Γ of the resonance via

$$\Gamma = \frac{2\hbar}{T_\varphi} \quad (2.33)$$

where $\hbar = h/2\pi$ is Planck's constant. It can be written as the sum of two contributions

$$\frac{1}{T_\varphi} = \frac{1}{2T_{\text{rel}}} + \frac{1}{T_{\text{col}}} \quad (2.34)$$

where T_{rel} describes the relaxation of the oscillating electrons towards equilibrium and includes both radiative and nonradiative damping and T_{col} is related to collisions of the electrons with the lattice atoms.

It has been shown, however, that the contribution of collisions can be neglected in most systems and the dephasing time thus reduces to $T_{\varphi} = 2T_{\text{rel}}$. Focusing on the size-dependence of the radiative and non-radiative contributions to T_{rel} , an optimum size on the order of 20 nm (for spherical particles) is found, which results in a minimum linewidth for the localized surface plasmon resonance.¹³

2.4 PLASMONIC PERFECT ABSORBERS

Plasmonic devices with absorbance close to unity have emerged as essential building blocks for a multitude of technological applications ranging from trace gas detection to infrared imaging.

To enable this functionality, plasmonic absorbers commonly incorporate resonant particles above a dielectric spacer layer and metallic mirror to achieve absorbance close to unity in a variety of spectral ranges. Starting from original experiments in the GHz and THz region,^{21,22} plasmonic and metamaterial-based perfect absorbers have moved towards the near-infrared and visible spectral ranges, with applications ranging from glucose and gas sensing to spectroscopy and photovoltaic efficiency enhancement.^{14,23–25}

In general, a reflectance of zero in an optical element can be obtained by matching its optical impedance Z to the value of the surrounding space. In perfect absorbers, this impedance can be tuned by varying geometric parameters such as the size of the resonant structure or the thickness of the spacer layer. Since the thick metallic mirror below the structure ensures zero transmittance, perfect impedance matching consequently results in perfect absorption at a certain design wavelength.

The underlying physics behind perfect absorption are commonly explained in one of two ways. The first explanation assumes resonant near-field coupling between the top nanostructure and the metallic mirror below. For simplicity, we focus on

the absorber structure from section 5.1, consisting of palladium nanowires stacked above a MgF_2 spacer layer and a gold mirror.

When light impinges on the structure, particle plasmon oscillations are excited in the resonant nanostructure at the top of the stack. The corresponding charge distribution then causes the oscillation of a mirror plasmon in the metallic film below (Fig. 2.5).

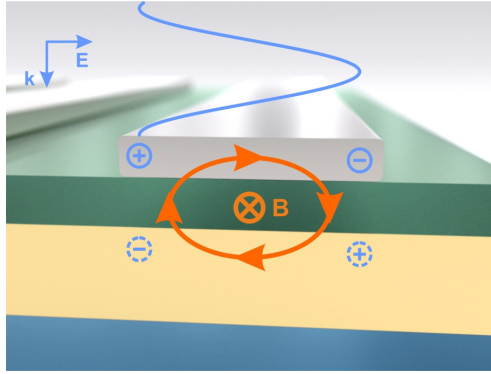


Figure 2.5: Working principle of a plasmonic perfect absorber consisting of resonant palladium nanowires stacked above a MgF_2 spacer layer and a gold mirror. The formation of an magnetic mode allows for efficient coupling of incident light to the structure, and the energy is subsequently dissipated via Ohmic losses in the metallic components of the structure.

By tuning the thickness of the dielectric spacer layer, the phase delay between the plasmon and the mirror plasmon oscillation can be adjusted so they oscillate in antiphase. This is assumed to lead to the formation of a circular current distribution and consequently an induced magnetic mode in the spacer layer, which enables control over the impedance, and can also be found in other plasmonic geometries.^{26,27} Additionally, impedance matching plays an important role in areas such as plasmonic waveguiding.²⁸

Recently, it has been shown that the near-field interaction of the resonant particle and the mirror can be decoupled, and the absorptive behavior can be explained in terms of interference between the two layers.²⁹ However, it is important to stress that regardless of the microscopic explanation of the perfect absorp-

tion behavior, the impedance matching picture for the full optical element remains valid.

2.5 MATERIALS FOR HYBRID PLASMONIC DEVICES

2.5.1 *The palladium-hydrogen system*

Transition metals play a key role in solar to chemical energy conversion technologies, due to their ability to store large amounts of hydrogen in their lattice. This confinement of potentially explosive hydrogen gas in a closed and inert system is a mayor safety requirement for a future hydrogen economy.

Palladium is a prototypical and widely investigated metal-hydride system, owing to the fact that pure samples are relatively easy to prepare and require no specialized surface treatments.³⁰

In order to examine the hydrogen absorption and desorption trajectories, the concentration of hydrogen atoms in the palladium lattice c_H in relation to the applied hydrogen pressure p_H is measured for different temperatures T (Fig. 2.6). The pronounced plateaus of these pressure-composition isotherms at pressures below a certain critical point p_C show that two phases are present in the system.³¹

For small pressures, hydrogen forms a solid solution in the palladium lattice, which is in thermal equilibrium with the surrounding hydrogen atmosphere. In this so called α -phase the relationship between concentration c_H and pressure p_H is simply given by Sievert's law

$$\sqrt{p_H} = K_S \cdot c_H \quad (2.35)$$

where K_S is Sievert's constant.

In this pressure range, the dissolved hydrogen is treated as protons moving freely throughout the bulk of the metal, forming a so-called solid solution.

When moving to higher pressures, the H-H and Pd-H interactions become stronger, leading to the formation of a palladium hydride β phase. Here, the face-centered cubic lattice structure of the palladium is maintained whereas the lattice constant increases by approximately 4%.³² Since the lattice expands equally

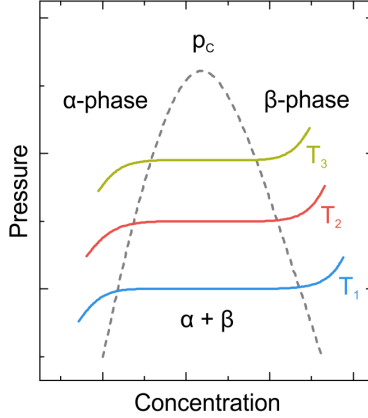


Figure 2.6: Sketch of the pressure-composition isotherms in the palladium hydrogen system. Intermixing between the α and β phases leads to the formation of pronounced plateau regions below a critical point p_H .

in all directions, this corresponds to a substantial volume increase of around 12%, which will become important in the antenna-enhanced sensing geometries presented in section 4.1.

The isotherms in Fig. 2.6 can now be divided into three distinct parts. For low pressures, the α -phase dominates, hydrogen is freely dissolved in the palladium lattice and the concentration follows Sievert's law $c_H \sim \sqrt{p_H}$.

Starting at a critical pressure $p_\alpha(T)$ (dashed line in Fig. 2.6, left side), H-H interactions begin to create agglomerations of hydrogen, which serve as seeds for palladium hydride formation. During phase coexistence, the conversion from α to β phase strongly increases the concentration of hydrogen in the lattice without a corresponding jump in pressure. This follows from Gibbs' phase rule, assuming both phases are in thermal equilibrium.

For pressures above $p_\beta(T)$ (dashed line in Fig. 2.6, right side), only the β phase remains and the isotherm follows a curve similar to the low-pressure regime. This is due to the fact, that increased external hydrogen pressure only leads to the formation of more palladium hydride and not to the creation of a new phase.

In the coexistence region $p_\alpha < p < p_\beta$, the pressure where the plateau region of the isotherm is located is highly dependent on the history of the system. Specifically, different plateau pressures are recorded for hydrogen ab- and desorption. This hysteresis effect is well known for bulk palladium systems and has recently been investigated for palladium nanoparticles down to only several nanometers in size.^{33–35}

Importantly, the complex phase-transition behavior of the palladium hydrogen system can be accessed optically by measuring the changes of the dielectric function of palladium, which is directly linked to the hydrogen content in the Pd lattice.³⁶

2.5.2 Yttrium and yttrium hydrides

The strong hydrogen-induced dielectric change is one of the key features of palladium-based plasmonic devices. However, both palladium and palladium hydride have metallic character, limiting the dynamic range of such geometries. To move beyond this limitation, a material which exhibits a phase transition from metallic to nonmetallic or vice versa is needed.

Promising candidates for such materials are the rare-earth hydrides, which show a robust and reversible phase transition with pronounced optical contrast at visible and near-infrared wavelengths. Among the rare earths, yttrium (Y) and its hydrides (YH_x) play a prominent role, especially due to their use in technologically relevant switchable mirror devices.³⁷

As deposited, yttrium is a metal with hexagonal close-packed crystal structure. Upon hydrogenation, it undergoes a phase transition to yttrium dihydride (YH_2), which again has metallic character but exhibits face-centered cubic crystal structure. Importantly, this phase transition is irreversible at room temperature, and the YH_2 phase is stable even when the partial pressure of hydrogen in the environment is reduced to zero.

The reversible phase transition occurs between the yttrium dihydride (YH_2) and trihydride (YH_3 , hcp crystal structure) states and can be driven by the hydrogen partial pressure applied to the system. The metal-to-insulator transition occurs at a hydrogen

content of $x = 2.86$, where the system changes from metal-like to semiconductor-like.³⁸

The pronounced dielectric contrast and qualitative change of optical properties (metal vs. dielectric/semiconductor) makes yttrium an ideal candidate for incorporation into reconfigurable plasmonic systems. The experimental realization of such a device based on yttrium nanoantennas is discussed in section 5.3 together with the concept of a reconfigurable perfect absorber.

Even though yttrium trihydride is commonly written as YH_3 , full stoichiometric YH_3 (hydrogen content $x = 3$) cannot be obtained even in a fully saturated hydrogen atmosphere at normal pressure, where $x = 2.9$ is reached. Full hydrogenation requires pressures on the order of 4 GPa or 40 times normal pressure.³⁹

So far, we have described the YH_2 - YH_3 phase transition as reversible, in the sense that the system can be switched from metal to semiconductor and back to the original metallic state. However, when tracing the hydrogenation and dehydrogenation trajectories a significant hysteresis effect is discovered. Strikingly, the plateau regions of the pressure-composition isotherms for hydrogen loading and unloading show a four orders of magnitude difference in hydrogen partial pressure.

This pronounced behavior is due to the different crystalline structure of YH_2 and YH_3 , which leads to different stress states during hydrogen loading and unloading. In rare earth hydrides with single phases such as lanthanum hydride (LaH_x), there is no phase coexistence and consequently a continuous increase or decrease of the hydrogen content without hysteresis.³⁸

Even though the yttrium hydrides offer excellent hydrogen-induced optical contrast, they are not able to catalytically dissociate hydrogen molecules into atomic hydrogen, which is required for hydride formation. To provide this catalytic functionality, yttrium is commonly combined with a platinum or palladium capping layer.³⁹ This layer both enables the efficient dissociation of hydrogen molecules and prevents the oxidation of yttrium films and nanostructures in normal atmosphere.

When optimizing the switching times of the hybrid Y/Pd material system, the thickness of the Pd capping layer plays a key role. Especially, the layer needs to be thick enough to form a con-

tinuous film, since thicknesses below the percolation thickness of Pd (around 7 nm) lead to island formation and allow oxygen to reach the yttrium layer below. For thick yttrium films, an ideal Pd thicknesses of 19 nm was found,³⁹ with even thicker layers resulting in a reduction of switching time.

2.5.3 *Phase-change materials for active plasmonics*

The realization of active plasmonic devices requires a move from widely used but passive metals such as silver or gold towards novel materials systems.^{40,41} This allows for additional degrees of freedom in device design and enables external control over the optical response of a plasmonic nanostructure without having to directly modify its geometry.^{42,43}

This direction has been a major topic of recent plasmonics research, with projects focusing on devices that can be reconfigured using external stimuli such as laser pulses, mechanical strain, heat, or electrical currents.

Phase change materials provide an ideal toolkit for the realization of such active nanodevices and several materials with heating- or laser-induced switching behavior such as vanadium-dioxide (VO₂)⁴⁴ and gallium lanthanum sulphide (GLS)⁴⁵ have already been investigated in the context of plasmonics.

Among these materials, germanium antimony telluride (GST) plays a key role. GST alloys can be stabilized in a variety of different stoichiometries, with the most widely studied being Ge₂Sb₂Te₅. GST-225 has been used in a wide variety of technological applications, especially in optical data storage. This is due to several advantageous material properties:

First, GST-225 can be stabilized in two distinct phases (amorphous and crystalline) at room temperature, which show significant contrast in their optical and electrical properties.⁴⁶

Second, the GST phase transition is reversible and can be induced by external heating or triggered optically on nano- and possibly even picosecond timescales.^{47–50} Furthermore, electrical switching on very fast timescales is also possible.^{51–53}

Third, GST alloys are fully compatible with standard complementary oxide semiconductor (CMOS) chip-scale nanofabrication techniques, aiding the integration into technological devices.

The detailed phase change processes for optical and electrical switching in GST-225 are shown in Fig. 2.7. As deposited, GST-225 presents as an amorphous chalcogenide glass and the simplest way of inducing the amorphous to crystalline phase transition is to heat the material above the phase transition temperature of 160 °C.⁵⁴

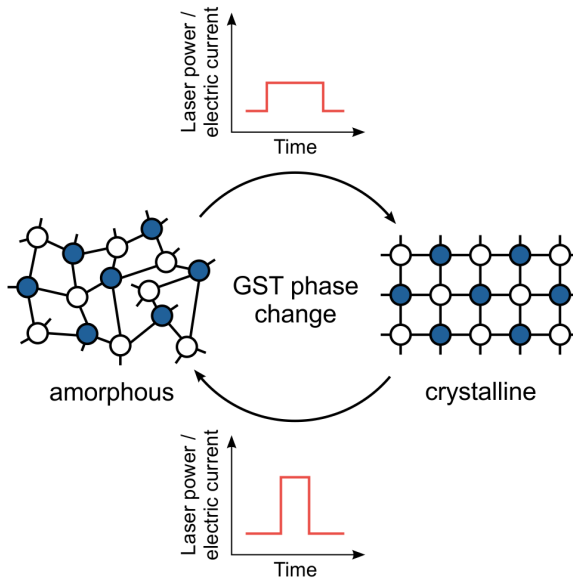


Figure 2.7: Sketch of the phase change processes in GST. Starting from the initial (as deposited) amorphous phase, crystallization can be induced by thermal heating above a specific crystallization temperature or by applying a long laser or voltage pulse. The system can be driven back to the amorphous state by applying a shorter high intensity pulse, which induces a melt-quench process.

Using all-optical or electrical means, the amorphous to crystalline phase transition can be triggered by applying a longer and lower power laser or voltage pulse. This leads to localized heating in the material and the subsequent formation of the crystalline phase (Fig. 2.7, top).

To drive the material back to the amorphous state, a shorter high intensity pulse is applied. The deposited energy heats the material above the melting temperature ($T_m \approx 600\text{C}$). Due to the near-instantaneous removal of the external heat source, the melted GST material undergoes a quenching process, stabilizing it in the amorphous phase (Fig. 2.7, bottom). Importantly, this switching of the GST material is very reproducible and can be performed several thousand times, enabling optical data storage applications, e.g., in rewritable CDs and DVDs.

However, due to the high absorption of GST-225 in the visible and infrared spectral ranges, hybrid plasmonic devices including GST-225 face some challenges. These can either be overcome by utilizing very thin GST layers,⁵¹ which may limit the optical contrast, or by moving to a different GST stoichiometry. Particularly, GST-326 is a promising candidate for plasmonic applications in the near- and mid-infrared due to its very low optical losses, as demonstrated in section 5.4.

INTRODUCTION TO PLASMONIC GAS AND CHEMICAL SENSING

Sensitive and robust detection of gases and chemical reactions constitutes a cornerstone of both scientific research and a multitude of industrial applications. In an effort to reach progressively smaller reagent concentrations and sensing volumes, optical sensor technology has experienced a paradigm shift from extended thin-film systems towards engineered nanoscale devices.

In this size regime, plasmonic particles and nanostructures provide an ideal toolkit for the realization of novel sensing concepts. This is due to their unique ability to simultaneously focus light into subwavelength hotspots of the electromagnetic field and to transmit minute changes of the local environment back into the farfield as a modulation of their optical response. Since the basic building blocks of a plasmonic system are commonly noble metal nanoparticles or nanostructures, plasmonics can easily be integrated with a plethora of chemically or catalytically active materials and compounds to investigate processes ranging from hydrogen absorption in palladium to the detection of trinitrotoluene (TNT).

This chapter will discuss a multitude of plasmonic sensing strategies, spanning the technological scale from simple metal nanoparticles embedded in extended thin films to highly engineered complex plasmonic nanostructures.* Due to their flexibility and excellent sensing performance, plasmonic structures open an exciting pathway towards the detection of chemical and catalytic events down to the single molecule level.

A crucial enabling factor for this are the greatly enhanced electromagnetic fields at the surface of a resonant plasmonic structure, which allow for the probing of minute changes in the surrounding environment. Due to the evanescent nature of the fields,

* This chapter is adapted from A. Tittl et al., *Plasmonic gas and chemical sensing*, *Nanophotonics* 3, 157-180 (2014). Reprinted with permission. Copyright 2014 Science Wise Publishing & De Gruyter.

the sensing volume of plasmonic nanostructures is only marginally larger than the structures themselves, making them ideal local probes for neighboring changes in a medium (Fig 3.1a,b). Consequently, plasmonic probes are especially relevant for monitoring of chemical or catalytic reactions, where the reaction efficiency can crucially depend on localized changes in reagent concentration or catalyst morphology.

In order to quantify the sensing performance of a plasmonic system, we can consider its refractive index sensitivity S , defined as the peak shift in nanometers of the plasmonic resonance per refractive index unit (RIU). However, since the final accuracy of the peak tracking depends both on the magnitude of the peak shift and on the resonance linewidth, a more suitable choice for plasmonic systems is the figure of merit (FOM), obtained by dividing the refractive index sensitivity by the full width at half maximum (FWHM) of the resonance (Fig. 3.1c).

Thus there are two key approaches for optimizing the figure of merit in a plasmonic sensing geometry: reducing the resonance linewidth (or FWHM), and increasing the peak shift by boosting the local field-enhancement. In general, plasmon oscillations in nanoparticles experience damping arising from two contributions: intrinsic damping due to electron-electron collisions and impurity scattering in the metal, as well as radiation damping due to the direct decay of the collective oscillations into photons. Utilizing noble metals for the resonant nanoparticles helps to reduce intrinsic damping. However, radiation damping, which constitutes the dominating effect for particles larger than a few tens of nanometers, cannot easily be overcome in simple plasmonic systems.^{55,56}

By arranging multiple plasmonic particles into a defined geometry, coupling effects may happen and can significantly reduce the linewidth of the plasmonic resonance.⁵⁷ One way to achieve this is to couple a broad dipolar plasmonic resonance to a spectrally narrow quadrupolar mode, which cannot be excited from the farfield. The coupling of two such modes can lead to a narrow spectral feature in the otherwise broad dipolar lineshape, a behavior known as the plasmonic analogue of electromagnetically induced transparency (EIT). Due to its reduced linewidth,

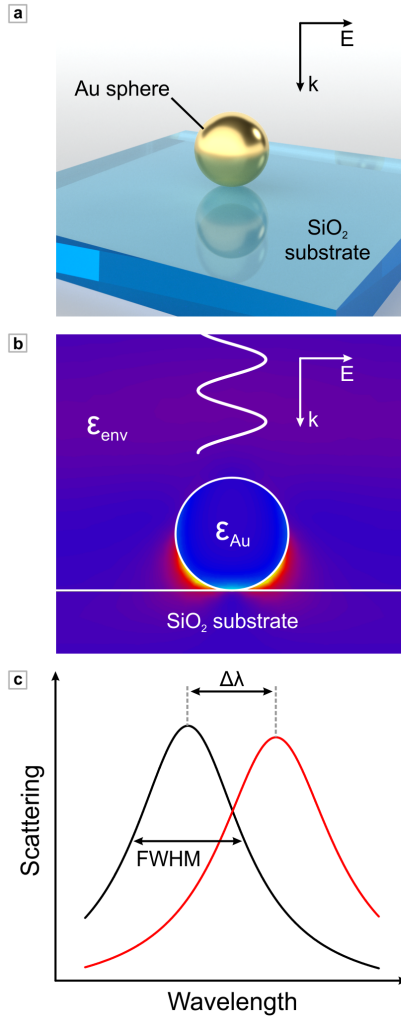


Figure 3.1: Principles of plasmonic sensing. (a) A simple plasmonic sensing geometry, consisting of a gold nanosphere on a glass substrate. The system is excited by a linearly polarized electromagnetic wave with electric field vector E and wave vector k . (b) Calculated energy density of the electric field for the described sensing geometry. The dielectric functions of the sphere and the environment are given by ϵ_{Au} and $\epsilon_{env} = n_{env}^2$, respectively. (c) Exemplary scattering spectra for the plasmonic system. Upon change of the refractive index in the environment by some value Δn , the resonance undergoes a wavelength shift $\Delta\lambda$.

this distinctive asymmetric lineshape (also referred to as a Fano resonance) exhibits a greatly increased FOM compared to simple dipolar plasmonic structures in the same spectral range.^{58–60}

To increase the electromagnetic field-enhancement, plasmonics has taken cues from classical antenna theory. In triangular “bowtie” nanoparticle geometries, the electromagnetic fields can be enhanced and concentrated at the tips of the structure. By utilizing complex Yagi-Uda antenna designs on the nanoscale, efficient and directed energy transfer between the far-field and the near-field can be realized.^{61,62} Using the coupling between, e.g., two rod-type nanoantennas can further enhance the near-fields compared to single antenna elements. When decreasing the distance between the two rods, the electromagnetic fields can be confined to a progressively smaller volume, leading to extremely high enhancement factors, only limited by fabrication tolerances and quantum mechanical tunneling effects below sub-1 nm gaps.^{63–65}

When such highly sensitive plasmonic structures are adapted for sensing applications, two main concepts for the detection of gases and chemical reagents emerge: in direct sensing configurations, the reagents actively influence the plasmonic entity, changing its material properties and in turn its optical response, whereas in indirect sensing schemes, the plasmonic structure is located adjacent to some reagent-sensitive material and simply probes the dielectric changes in that system.⁶⁶

One experimental issue connecting both sensing schemes is the correlation of gas or reagent concentration changes with changes in the optical response. To facilitate this analysis, one commonly extracts a single “sensor signal” value from the full spectral response. Depending on the system under consideration, observables such as the intensity at a given wavelength, the resonance position, or the resonance peak’s full width at half maximum (FWHM) can be tracked in relation to environmental changes. This allows for straightforward performance comparison between plasmonic sensor designs with different structural and configurational parameters.

In the following, this chapter will review both direct and indirect sensing schemes, covering a wide technological range from

plasmonically functionalized thin films through engineered chemically grown particles composed of multiple materials all the way up to complex nanostructured geometries. The presented sensor devices are selected to showcase the wide array of reagents that can be investigated using plasmonic systems as well as the most versatile and high-performance complex plasmonic nanoprobos. By combining highly sensitive nanodevices with novel reagent-specific materials, plasmonic sensors can be used to investigate a plethora of chemically and biologically significant reagents, with nanometer spatial resolution and possibly down to the single molecule level.

3.1 THIN FILMS WITH EMBEDDED PLASMONIC PARTICLES

One straightforward approach to optical sensing is the use of thin films of reagent-sensitive material deposited on a substrate. Such films combine robust fabrication via standard evaporation or sputtering techniques with simple optical transmission or reflection measurements for read-out.^{67,68}

In order to enhance the sensor performance and tailor the optical response of such thin films, small plasmonic particles can be added using co-deposition or multi-step processes. When considering thin films with embedded plasmonic particles, two main concepts can be distinguished. In plasmonically enhanced systems, small noble metal particles in the thin film act simply as light concentrators and probes to enhance the dielectric changes in the surrounding material. In catalytically enhanced systems, gold nanoparticles in direct contact with, e.g., transition metal oxide films can substantially increase the catalytic activity of such composite systems. Here, the optical response is often caused by charge transfer processes between the transition metal oxide and the embedded Au nanoparticles. In the following, we will first focus on two examples of catalytically enhanced thin-film systems.

Carbon monoxide sensing with plasmonically functionalized thin films

Due to its high toxicity, sensitive and reliable detection of carbon monoxide is vital for industrial process and environmental monitoring applications. Ando et al. have demonstrated a plasmonically functionalized Au-CuO nanocomposite film for CO sensing, fabricated by first depositing Au particles on a substrate via DC sputtering and then covering them with a CuO film via pyrolysis.⁶⁹ Figure 3.2a shows a transmission electron microscope (TEM) image of the nanocomposite film, where small Au particles of average diameter 24 nm surrounded by a CuO matrix can be clearly identified.

The authors performed absorbance measurements at a temperature of 300 °C and observed a plasmonic absorbance peak at a wavelength of around 800 nm. The magnitude of this peak

increased substantially upon exposure of the film to 1000 ppm and 1 vol.% CO in dry air (Fig. 3.2b). In addition, when calibrating their sensor device with various concentrations of CO in dry air, the authors found a linear relation between the absorbance change and the logarithm of the CO concentration over a wide range from 50 to 10000 ppm CO in dry air (Fig. 3.2c), allowing for straightforward quantitative sensing.

A similar approach for the detection of CO was presented by Sirinakis et al., who used gold nanoparticles embedded in an yttria-stabilized zirconia (YSZ) matrix.⁷⁰ Their device was fabricated using radio frequency magnetron co-sputtering followed by an annealing process and optical characterization was performed in a quartz transmission cell surrounded by a tube furnace (Fig. 3.2d).

The authors observed a pronounced Lorentz-like absorbance peak at a wavelength of around 600 nm, which spectrally narrowed and blueshifted upon CO exposure. This change allowed the authors to detect concentrations ranging from 0.1 to 1 vol.% CO in dry air at a temperature of 500 °C (Fig. 3.2e). However, they observed no change in the optical response when exposing their sample to CO in nitrogen carrier gas. The authors attributed this behavior to the reactivity of the YSZ film to oxygen, since switching from nitrogen carrier gas to dry air already introduced a broadening and redshift of the plasmon resonance in their system (Fig. 3.2f).

This allowed them to explain the blueshift and narrowing of the plasmon resonance through charge transfer into the Au nanoparticles caused by the oxidation of CO and the corresponding reduction of the YSZ matrix at high temperatures. This behavior makes the system by Sirinakis et al. a prime example of catalytically enhanced sensing with plasmonically functionalized thin films.

Hydrogen sensing with plasmonically functionalized thin films

Other than carbon monoxide, hydrogen detection is an additional safety factor in large-scale industrial chemical processing.⁷¹ Hydrogen forms a combustible mixture with air at concentrations

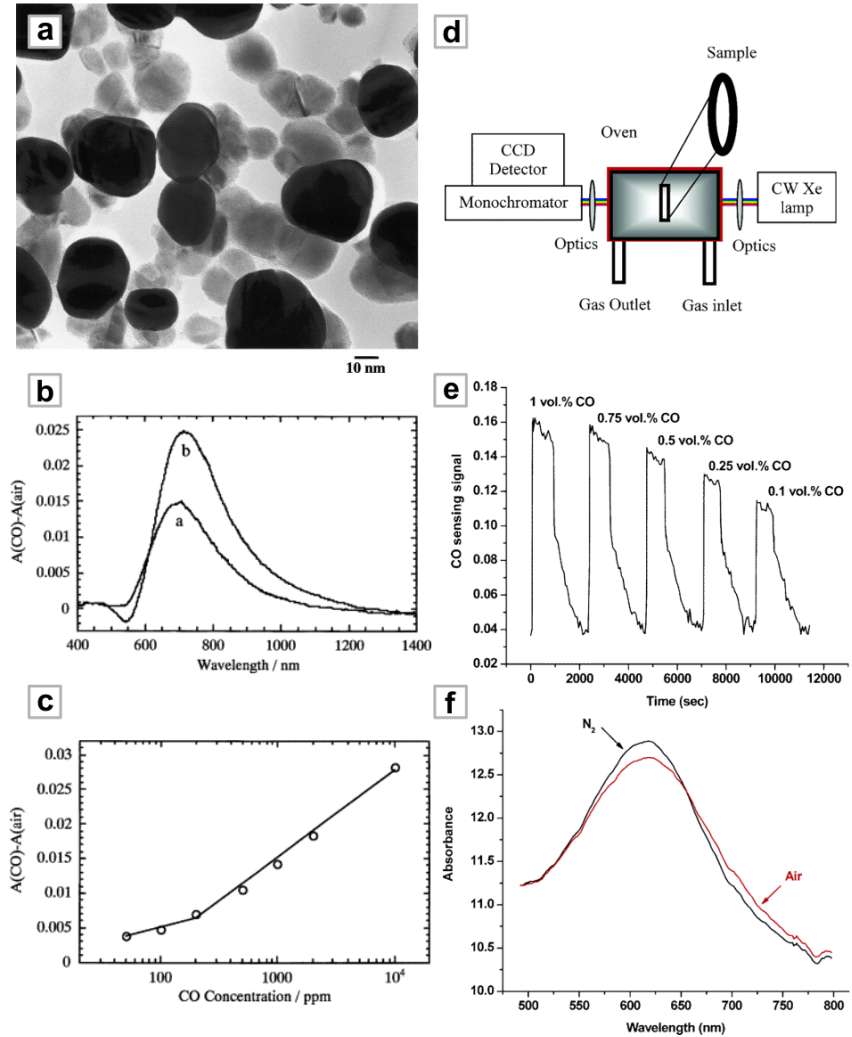


Figure 3.2: Carbon monoxide sensing with plasmonically functionalized thin films. (a) Transmission electron microscope image of a Au-CuO nanocomposite film. (b) Relative CO-induced absorbance change of the Au-CuO composite film. (c) Correlation between CO concentration and relative absorbance change. (d) Schematic of a setup used for high temperature CO sensing experiments. (e) Sensing signal response curve of the Au-YSZ nanocomposite film at 500 °C. (f) Absorbance of the Au-YSZ nanocomposite film in N_2 and air at 500 °C.

ranging from 4 vol.% to 76 vol.%, which can be ignited easily with sparks or at a sufficiently high temperature. Therefore, sensitive hydrogen detection is a cornerstone of alternative energy concepts such as water splitting or, in more general terms, solar-to-chemical energy conversion.⁷²

In this framework, Buso et al. have utilized a SiO₂ matrix containing Au and NiO nanoparticles for sensitive detection of hydrogen, where the SiO₂ matrix was chosen due to its high specific surface area.⁷³ High-resolution TEM images in Fig. 3.3a show the evenly distributed Au particles embedded in the SiO₂ host material, surrounded by finely dispersed crystallite NiO particles.

In optical measurements, the authors found a plasmon resonance peak at a wavelength of 563 nm, which underwent a drastic blueshift of 22 nm when exposing the sensor device to 1 vol.% H₂ in dry air. This pronounced change in the optical behavior (Fig. 3.3b) could not be sufficiently explained in terms of catalytic charge transfer into the Au particle, which led the authors to classify their system as a case of plasmonically enhanced detection of hydrogen.

There was, however, a second sensing pathway when exposing the sensor device to CO with a weaker but still measurable response (Fig. 3.3b). The authors assumed an injection of electrons from the NiO crystallites into the Au nanoparticles during CO exposure and subsequent oxidation, which led to the observed changes in the plasmonic response. Thus, their system combined both plasmonically and catalytically enhanced approaches for detecting hydrogen and carbon monoxide.

In a further study on this system, Dharmalingam et al. investigated Au-YSZ nanocomposite films with varying sizes of the embedded Au particles for detection of CO and H₂.⁷⁴ To achieve the desired parameter variation, the authors fabricated their samples using layer-by-layer physical vapor deposition (PVD), where Au was deposited first to form small islands on the substrate and then covered with YSZ (Fig. 3.3c).

They then exposed the film to different concentrations of H₂ and CO at a temperature of 500 °C and monitored the spectral changes of the film's plasmon resonance peak at a wavelength of around 580 nm. Calibration curves for several Au nanoparticle

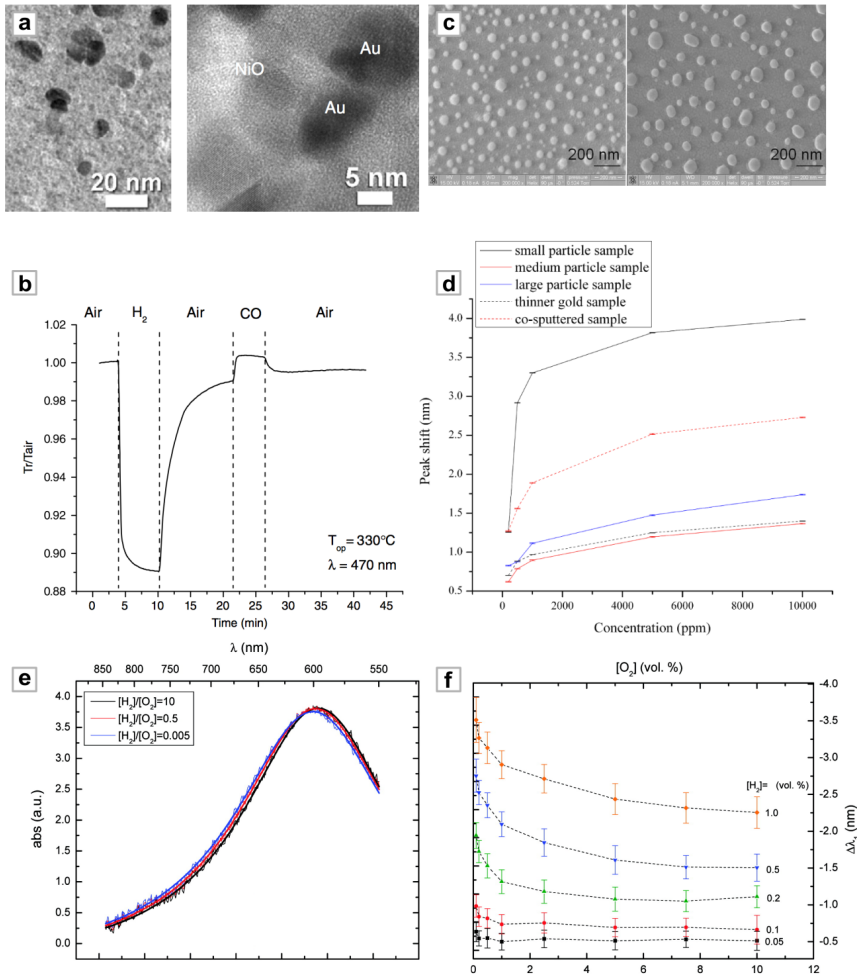


Figure 3.3: Hydrogen sensing with plasmonically functionalized thin films. (a) Cross-sectional and high-resolution TEM images of a SiO₂ matrix containing Au and NiO nanoparticles. (b) Dynamic optical response of a film containing 6% Au exposed to cycles of 1 vol.% H₂ in air and 1 vol.% CO in air. (c) SEM images of small-particle and medium-particle Au-YSZ nanocomposite films. (d) Hydrogen sensing calibration curves for nanocomposite samples with different particle sizes and preparation methods. (e) Absorbance spectra and Lorentzian fits for a Au-YSZ film under various redox conditions at 500 °C. (f) Change in plasmon resonance position as a function of O₂ concentration upon exposure to various concentrations of H₂.

configurations are shown in Fig. 3.3d. The authors found that the film with the smallest Au particles (mean crystallite size of approx. 50 nm) yielded the largest response to hydrogen exposure (Fig. 3.3d).

When comparing this response to a co-deposited nanocomposite film, where the Au particles were embedded in an YSZ matrix, they obtained an enhancement of the sensing performance by a factor of 1.5. However, this enhancement is accompanied by a decrease of the sensitivity to CO.

Still, the study by Dharmalingam et al. outlines how sensitivities and selectivity in Au-YSZ nanocomposite films can be tuned by a straightforward variation of one of the structure parameters, accelerating the development of integrated sensor chips for multiple reagents.

Au-YSZ can also serve as a broader model system for the investigation of electrochemical reactions in nanocomposite geometries, as demonstrated by the work of Rogers et al., who monitored the optical response of Au nanoparticles embedded in an YSZ matrix during H₂ exposure.⁷⁵ However, by simultaneously tuning the concentration of H₂ and O₂, they were able to achieve much better control over the electrochemical reactions occurring in the nanocomposite film.

They studied hydrogen to oxygen ratios in nitrogen carrier gas ranging from 10 (1 vol.% H₂, 0.1 vol.% O₂) to 0.005 (0.05 vol.% H₂, 10 vol.% O₂) and found clear influence of the mixing ratio on the optical response (Fig. 3.3e). When comparing the spectral shifts in their nanocomposite system for different H₂ and O₂ concentrations, the authors made two key observations: an increase of the H₂ concentration generally led to a blueshift and a narrowing of the plasmon resonance, whereas an increase of the O₂ concentration led to a redshift and a broadening (Fig. 3.3f).

This behavior could be explained by reaction-induced charge transfer between the oxygen ions in the YSZ matrix and the Au nanoparticles, where the blue- and redshifts were associated with charge injection and removal, respectively. Taking a further step, the authors were able to correlate the plasmon resonance position (and thus the square root of the charge density in the Au nanoparticles) with the gas mixing ratio through an electrochemi-

cal model, paving the way towards the all-optical interrogation of different oxygen ion transport and charge transfer mechanisms.

Chemical sensing in harsh and corrosive environments

In recent years, industrial energy production has experienced an increasing shift from traditional fossil-based technologies towards renewable sources. However, large-scale petrochemical processing is still a vital step in the production of a multitude of products ranging from plastics to pharmaceuticals. Many important petrochemical reactions take place at high temperatures and in otherwise harsh or corrosive environments, which requires constant and reliable process monitoring. Due to their durability, sensitivity, and all-optical readout, plasmonically functionalized thin films are well positioned to detect a variety of reagents in such challenging environments.

Towards this goal, Ohodnicki et al. have utilized an Au/TiO₂ nanocomposite film for the detection of hydrogen at temperatures as high as 850 °C.⁷⁶ The authors prepared their nanocomposite through sol-gel deposition techniques and obtained a TiO₂ matrix with a well-controlled amount of dispersed Au crystallites (Fig. 3.4a). TiO₂ was chosen due to its reactivity to a variety of gaseous reagents combined with excellent thermal stability.

They then examined the sensing performance of their device by exposing it to 4 vol.% H₂ in N₂ carrier gas at temperatures of 600 and 850 °C while recording the transmittance changes close to the plasmon resonance position at a wavelength of 625 nm (Fig. 3.4b). The authors observed pronounced, reversible and reproducible transmittance changes for both temperatures and found that the response time of their system could be reduced from 33 to only 3 minutes by increasing the temperature from 600 to 850 °C.

This rapid and reproducible response makes the Au/TiO₂ system suitable for chemical process monitoring, especially at high temperatures associated with advanced petrochemical processing or reactions in solid oxide fuel cells.

Besides high-temperature chemical monitoring devices, sensors for the detection of reagents in harsh or corrosive environments also play a pivotal role in controlling large-scale chemical

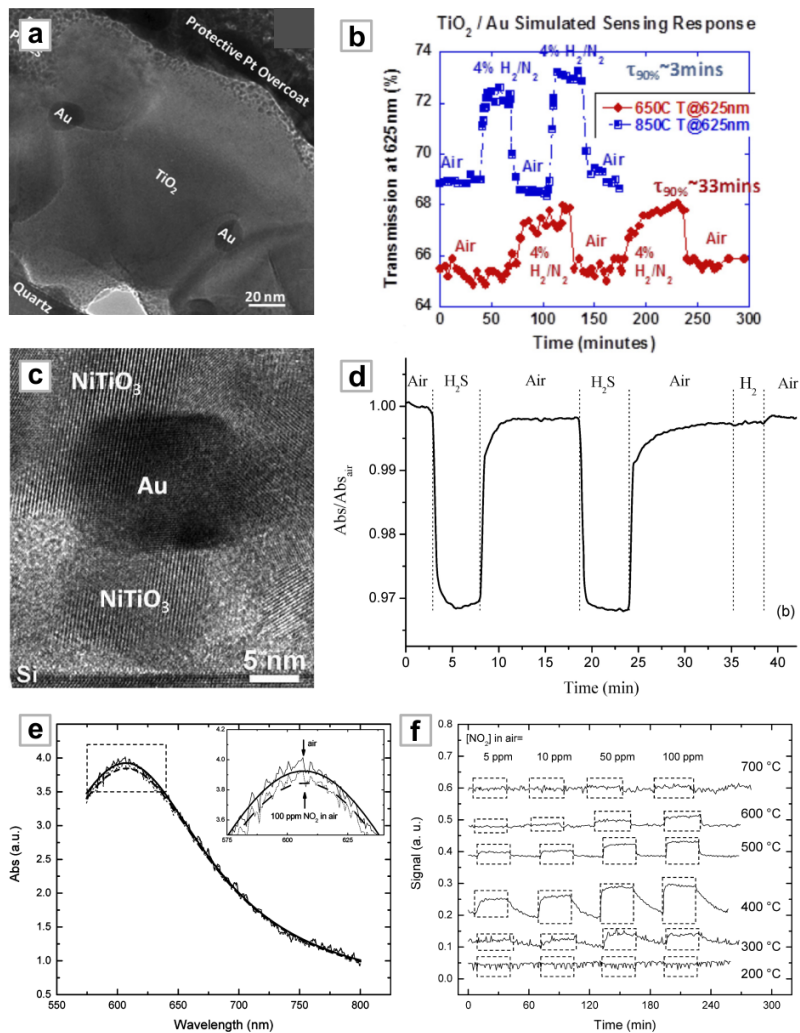


Figure 3.4: Sensing in harsh and corrosive environments. (a) Cross-sectional TEM images for an Au/TiO₂ nanocomposite thin film. (b) Sensing response of an Au/TiO₂ film to 4 vol.% H₂ in different environmental conditions. (c) Bright-field TEM images of an Au-70TiO₂-30NiO nanocomposite film. (d) Dynamic response of the Au-TiO₂-NiO nanocomposite film to gas concentrations of 0.01 vol.% H₂S and 1 vol.% H₂ in air. (e) Absorbance spectra and Lorentzian fits for an Au-YSZ film exposed to air and 100 ppm NO₂ in air. (f) Sensor signal intensity over time for a Au-YSZ film exposed to air (signal decrease) and 5, 10, 50, and 100 ppm NO₂ in air (signal increase) at 200, 300, 400, 500, 600, and 700 °C.

processing plants. Hydrogen sulfide (H_2S) is a prominent example for a toxic and corrosive gas that is produced in chemical reactions ranging from natural gas manufacturing to food production.

Della Gaspera et al. utilized a TiO_2 -NiO film with embedded Au nanoparticles for the detection of H_2S down to the parts per million (ppm) range.⁷⁷ The authors produced the films using a sol-gel method with a subsequent annealing step at 500-600 °C and examined three composition ratios of the TiO_2 -NiO system: 70 TiO_2 -30NiO, 50 TiO_2 -50NiO, and 30 TiO_2 -70NiO.

Bright-field TEM imaging of an Au-70 TiO_2 -30NiO nanocomposite film showed that annealing at 600 °C could result in the formation of NiTiO_3 islands in addition to the NiO and TiO_2 phases (Fig. 3.4c).

In gas sensing experiments, the authors exposed the three nanocomposite films to 100 ppm H_2S and 1 vol.% H_2 in air and monitored the absorbance change at resonance (Fig. 3.4d). They found that the Au-70 TiO_2 -30NiO film yielded the best dynamic behavior with large absorbance changes as well as quick response times. The sample also showed only a negligible response to H_2 versus H_2S , even at a concentration ratio of 100:1, demonstrating the excellent selectivity of the device.

So far, this chapter has mainly covered sensing applications for chemical process engineering. However, the monitoring of exhausts released into the environment is equally important. Many combustion processes release large amounts of nitrous oxides (NO_x), which contribute to the formation of acid rain and degrade water quality on a global scale. Thus, the detection of NO_x close to the source of formation in, e.g., a turbine jet engine is crucial for the development of low-emission machinery.

In this context, Rogers et al. extended their previous work on Au/YSZ nanocomposites towards the detection of NO_x in small amounts and at temperatures between 500 and 800 °C.⁷⁸ They prepared their nanocomposite using co-magnetron PVD with a subsequent annealing step and obtained films with an average grain size of approx. 28 nm for both Au and YSZ crystallites. The film was then exposed to different ppm range concentrations of NO_2 in air and the optical absorbance change was recorded for

different temperatures. When comparing the absorbance spectra for 100 ppm NO₂ in air with air at a temperature of 500 °C, a redshift and a broadening of the plasmon resonance could be observed (Fig. 3.4e).

The authors attributed this behavior to the removal of electrons from the Au nanoparticles, caused by oxygen ion production during the dissociation of NO₂ on the Au-YSZ nanocomposite. To further characterize the temperature dependence of the sensor response, they exposed their sensor device to concentrations of 5, 10, 50, and 100 ppm NO₂ in air at different temperatures ranging from 200 to 700 °C. To simplify analysis, the authors subtracted the optical spectra during gas exposure from the “baseline” spectrum in air and defined their sensor signal as the difference between maximum and minimum of the resulting curve (Fig. 3.4f).

They found the highest sensor signal change for a temperature of 400 °C whereas the best trade-off between magnitude of the signal and response time was observed at a temperature of 500 °C, with a sensitivity down to 5 ppm NO₂ in air. Furthermore, they were able to resolve concentrations of 50 ppm NO₂ in air in a wide temperature range from 300 to 700 °C, which makes their design ideally suited for industrial NO₂ monitoring.

3.2 ENGINEERED NANOPARTICLES AND SMART DUST

Highly engineered or “smart dust” nanoparticles offer many exciting possibilities for the detection of chemical or biological reagents.⁷⁹ Furthermore, the combination of multiple materials in complex core-shell nanoparticles and the use of advanced synthesis procedures allow for new functionalities as well as increased flexibility in structure design.^{80–82}

Implementing this concept for plasmonic gas sensing, Ghodselahi et al. have demonstrated the use of Cu@CuO core-shell nanoparticles for the detection of carbon monoxide.⁸³ The authors first prepared hexagonal Cu nanoparticle arrays on a glass substrate through co-deposition of RF-sputtering and RF-PECVD, and subsequently oxidized them under airflow to obtain the CuO shell structure. This yielded uniform Cu@CuO core-shell nanoparticles with a thickness of 35 nm and a mean lateral dimension of 10 nm. To demonstrate the carbon monoxide sensitivity of their system, the authors recorded absorbance spectra of their sample during exposure to different flow rates of CO.

In ambient air, they observed a pronounced plasmon resonance peak at around 600 nm, which underwent a spectral redshift and an increase in absorbance for increasing CO flow rate (Fig. 3.5a). Spectral redshifts of approximately 3 nm were observed for a low flow rate of 1.61/h, with a maximum value of approx. 8 nm and saturation-like behavior for flow rates in the 101/h range (Fig. 3.5b).

This response could be attributed to CO adsorption on the CuO shell, which lead to a dielectric change in the active material and thus to a spectral shift of the plasmon resonance in the Cu. Since CO molecules are only adsorbed on the particle surface, the CuO shell could potentially be cleaned via a low-temperature annealing step in air. This would reduce sensor performance degradation and enable long-term environmental monitoring applications.

Apart from different metals and oxides, smart dust nanoparticles can also be capped with biological species to facilitate the detection of diverse reagents. Vasileva et al. have demonstrated the use of starch-stabilized silver nanoparticles to detect hydro-

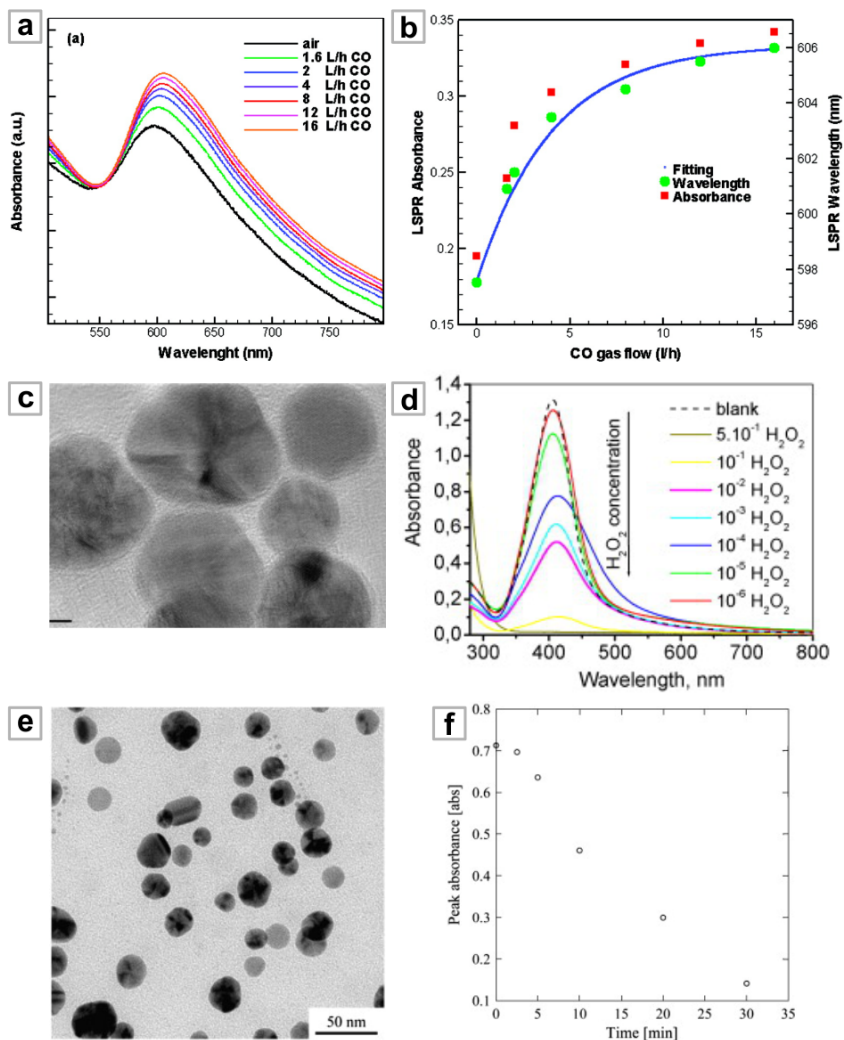


Figure 3.5: Sensing with complex core-shell nanoparticles. (a) Absorbance spectra of Cu@CuO core-shell nanoparticles under air and various CO gas concentrations. (b) LSPR absorbance (left) and LSPR wavelength (right) versus CO concentration. (c) TEM image of starch-stabilized silver nanoparticles for hydrogen peroxide detection. (d) Absorbance spectra of the Ag nanoparticle solution 15 min after the addition of hydrogen peroxide solution for different H_2O_2 concentrations. (e) TEM image of PVP-coated silver nanoparticles in water. (f) Absorbance at resonance over time after the addition of 1 mM hydrogen peroxide.

gen peroxide (H_2O_2).⁸⁴ Hydrogen peroxide plays an important role in the human body, where it is a key factor for oxygen metabolism, enzymatic breakdown of glucose or lactose, and oxidative stress.⁸⁵

In their experiments, the authors designed a green synthesis procedure employing only soluble starch, silver nitrate, D-glucose, and sodium hydroxide to obtain an aqueous dispersion of nanoparticles with a mean diameter of 14.4 nm and excellent uniformity. Importantly, they performed ultrasonication and controlled alkalization of the reaction medium to tailor the size and shape of their Ag particles (Fig. 3.5c). A key feature of their synthesis approach is the use of soluble starch as a capping agent, which eliminated the need for toxic chemicals in the reaction process and still allowed for sufficient control over particle morphology.

When added to the nanoparticle dispersion, H_2O_2 acted as an active oxidant, leading to the degradation of the starch-stabilized silver particles. The authors could correlate this degradation with the absorbance strength of the silver particles' plasmon resonance and thus were able to reliably differentiate H_2O_2 concentrations ranging from 10^{-1} to 10^{-6} mol/l (Fig. 3.5d).

A different bio-inspired approach for detection of H_2O_2 has been demonstrated by Endo et al.⁸⁶ They used silver nanoparticles in solution to obtain a pronounced plasmonic response, but coated them with polyvinylpyrrolidone (PVP) to improve their stability towards other reagents (Fig. 3.5e). Exposure to H_2O_2 led to an aggregation of the PVP-coated Ag nanoparticles and a subsequent decrease of the absorbance strength of the plasmon resonance at a wavelength of around 405 nm.

The authors investigated this behavior in more detail by introducing 1 mM H_2O_2 into a vial of PVP-coated Ag nanoparticles while tracking the absorbance over time (Fig. 3.5f). They again observed a strong decrease of the peak absorbance, with a large enough effect to be visible by naked eye. Thus, such coated nanoparticles could be employed as cheap and biocompatible color markers for medical and pharmaceutical applications.

Due to their unique properties, plasmonic smart dust particles can sensitively probe localized structural features such as size,

shape, material, and morphology.^{87,88} Furthermore, the efficiency of many physical, chemical and catalytic processes depends crucially on such nanoscale properties. This is especially true for large-scale catalytic hydrogen generation and storage, a key component of green energy production which may facilitate a move away from present, fossil-based technologies.

Palladium constitutes an ideal model system for hydrogen dissociation and subsequent absorption processes in metals.^{32,36,89,90} During catalytic loading, hydrogen molecules are first chemisorbed on the Pd surface, followed by near barrierless dissociation and subsequent diffusion of atomic hydrogen into the lattice. When increasing the hydrogen concentration, palladium undergoes a phase transition from a mobile, solid solution α -phase to a palladium hydride (PdH) β -phase. This transition causes both an expansion of the Pd lattice as well as a pronounced change in the dielectric function.

To study the influence of the localized particle geometry on this reaction, Tang et al. investigated the hydrogen uptake trajectories for individual Au/Pd core-shell particles with different shapes, faceting, and Pd shell thickness.⁹¹ The authors employed a synthesis method designed for particles with high quality but low uniformity to obtain a mixture of triangular plates, decahedrons, and icosahedrons (Fig. 3.6a). This allowed them to study nanoparticles with different sizes and shapes from the same synthesis process, aiding in reproducibility.

The authors first studied hydrogen-induced shifts of the plasmon resonance for an Au/Pd core-shell triangular plate particle and found a pronounced spectral redshift on the order of 25 nm (Fig. 3.6b). Both this result and similar measurements on icosahedrons were found to be in good agreement with numerical simulations, taking into account the dielectric function change from Pd to PdH. However, when investigating decahedral nanoparticles, the authors measured a pronounced spectral blueshift upon initial H₂ exposure (Fig. 3.6b), which could not be accounted for in numerical simulations using a simple Pd/PdH transition.

This contrasting behavior was attributed to two chemical transformations that occur during hydrogen exposure: the interdiffusion of Au and Pd, which leads to an effective decrease of the

Au particle size and thus a blueshift, and the formation of palladium silicide due to an reaction of the nanoparticles with silicon atoms of the substrate below. Both effects were found to be especially pronounced in nanoparticles with thicker Pd shells, allowing for the straightforward differentiation of the particle species. Thus, the plasmonic resonance of individual smart dust nanoparticles can serve as a sensitive probe for H₂ storage properties and metal support interactions in nanocatalytic systems, revealing geometry-dependent properties that are not accessible via standard ensemble measurements.

An ideal application for plasmonic smart dust nanoprob es is the catalytic generation of hydrogen, which is a key prerequisite for renewable energy production. Here, Seo et al. investigated the photocatalytic decomposition of lactic acid for hydrogen generation, using platinumized cadmium sulfide (Pt/CdS) nanocubes.⁹² In order to enable in-situ monitoring of the produced H₂ gas, they integrated gold domains into the nanocube reactors and recorded time-resolved dark-field scattering spectra from single structures (Fig. 3.6c).

When their nanoreactors were illuminated with white light, photons that match the optical band gap were absorbed in the CdS shells, leading to the generation of photoelectrons. These electrons can transfer to the Pt part and react with protons from the surrounding solution to produce H₂ gas.

During the reaction, the authors observed a gradual blueshift of the plasmonic resonance with a maximum value of 14 nm combined with a decrease of the scattering amplitude (Fig. 3.6d). This was found to be consistent with a change of the local environment close to the gold probe from 10% lactic acid in water ($n = 1.342$) to hydrogen gas ($n = 1.000$), taking into account that the Au probe has an average distance of 20 nm from the active Pt surface.

As expected, the time-resolved spectral resonance position followed a saturation behavior, reaching the maximum blueshift after around 10 minutes (Fig. 3.6e). By performing further analysis on their spectral time trace data, the authors were able to estimate the hydrogen generation from a single nanoreactor particle at around 1300 molecules per minute, showing that the use of

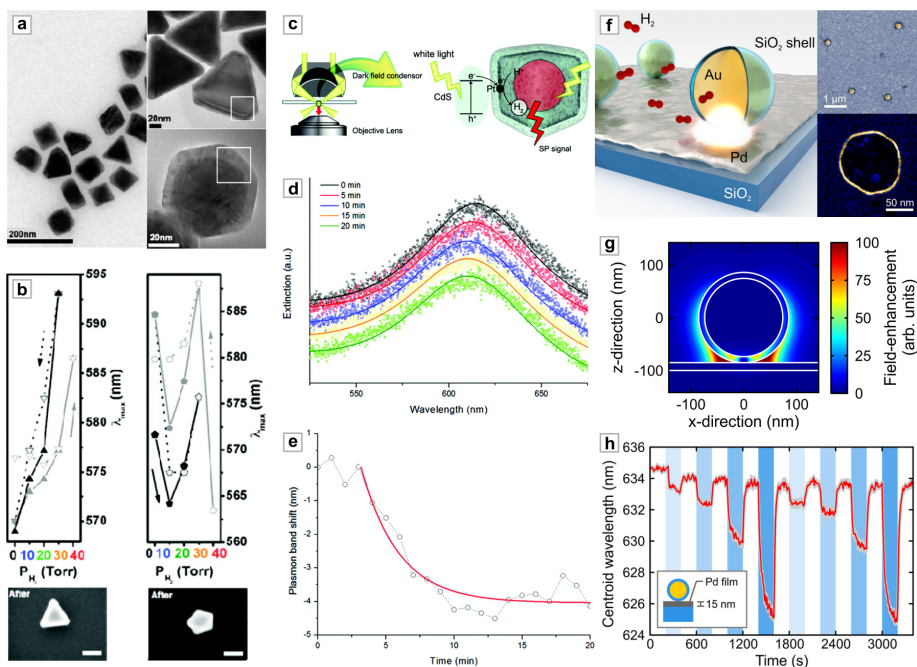


Figure 3.6: Complex smart dust nanoparticles for hydrogen and chemical sensing. (a) Low- and high-resolution TEM images of Au/Pd core-shell nanocrystals (b) Plasmon resonance shift upon hydrogen uptake and release for a single Au/Pd core-shell triangular plate (left) and decahedron (right). (c) Schematic diagram of single-particle measurement and detection on a single Au@Pt/CdS catalyst particle. (d) Extinction spectra of a single Au@Pt/CdS cube along the reaction progress. (e) Plasmon resonance shift during reaction for the same cube. (f) Schematic of plasmonic probing of local chemical reactions using smart dust nanoparticles (left). Exemplary element-resolved TEM and SEM images of the probing platform (right). (g) Electric near-field distribution at resonance. The intense near-fields are strongly localized at the touching point between the smart dust particle and the Pd film. (h) Time-resolved centroid wavelengths in response to hydrogen uptake and release for a single smart dust particle situated on a 15 nm Pd film.

smart dust probes can yield detailed information on local reaction kinetics from non-invasive far-field measurements.

In order to extend the presented concepts to the detection of chemical or catalytic processes in realistic material systems and environmental conditions, there is a need for a versatile sensing platform that can probe arbitrary surfaces and morphologies. To achieve this, we utilized silica shell-isolated gold nanoparticles to monitor local chemical reactions in real time.⁹³ A detailed discussion of this sensor geometry can be found in section 4.2.

Generally, smart dust nanoparticles can focus incident light into subwavelength hot spots of the electromagnetic field and optically report minute environmental changes at their pinning sites on the probed surface during reaction processes (Fig. 3.6f, left). Furthermore, the smart dust particles can easily be dispersed on target surfaces via drop-coating and allow all-optical readout via standard dark-field spectroscopy (Fig. 3.6f, right).

As a model system, we investigated the hydrogen dissociation and subsequent absorption in adjacent palladium thin films. A key feature of our particles is the ultrathin SiO₂ shell with a thickness of 10 nm (Fig. 3.6f, right), which both separates the Au core from direct contact with the probed agents and produces high localized field-enhancements (Fig. 3.6g). We then exposed a “dust on film” sample consisting of smart dust nanoprobe on a 15 nm Pd film to concentrations of 0.5, 1, 2, and 3 vol.% hydrogen in nitrogen carrier gas. We were able to observe different concentration steps as clear spectral blueshifts in the optical scattering response of single smart dust particles, with a maximum value of around 8 nm for 3% H₂ (Fig. 8h).

To check the ability of our sensor platform to resolve localized morphology changes, we investigated the “film on dust” system, where the smart dust particles were covered with a highly curved Pd film via tilted angle evaporation and found pronounced redshifts for all concentrations. This shows how the smart dust probing platform can transform small localized morphology changes into a complete reversal of the spectral shift direction in the far-field optical response. In the future, such techniques could combine two-dimensional imaging and spectroscopy to locally map chemical and catalytic reactions on a subdiffraction-limit scale.

3.3 LARGE-AREA NANOSTRUCTURED SENSOR CHIPS

Synthesis- and deposition-based approaches enable the reliable and high-throughput fabrication of plasmonic nanosensor devices. However, in order to produce large-area sensor chips with a pre-defined spatial arrangement of plasmonic elements, other fabrication methods such as soft-imprint lithography, nanosphere lithography, or (to some extent) electron-beam lithography often need to be implemented.^{5,6}

As a first example of nanosphere lithography, Wang et al. utilized ordered gold nanoparticle arrays to study the chemical adsorption of mercury vapor on the Au surface.⁹⁴ They fabricated the particle arrays by evaporating 2 nm chromium (Cr) and 40 nm Au through the interstitial voids of a densely packed monolayer of polystyrene (PS) nanospheres, followed by sonication in ethanol to remove the PS spheres from the substrate. This yielded triangular gold nanoparticles with a hexagonal spatial arrangement, which could be transformed into more circular nanodisks by a subsequent annealing step (Fig. 3.7a).

The authors then exposed their sample to 15 ppm of mercury vapor delivered by nitrogen flow and monitored the shift of the plasmon resonance peak over time. They found a clear monotonic spectral blueshift from 565 to 560 nm, which saturated after 2 hours and reached 85 % of the maximum value after around 30 minutes (Fig. 3.7b). This adsorption time was found to be shorter than in the case of an extended Au film, where only 67 % of the maximum response was obtained after 30 minutes.⁹⁵

In addition, the authors were able to regenerate their sensor chip using a heating step at 300 °C for 30 minutes, resulting in a return of the plasmon resonance position to the original value. The blueshift was attributed to the formation of an adsorbed mercury shell on the hemispherical Au nanoparticles, which could be clearly observed as a volume increase in AFM measurements, leading to a change of the effective refractive index and thus the observed spectral shifts.

Ma et al. used a structurally similar system for the detection of chloroform vapor, a prime example among the volatile organic compounds that play a role in both industry and medical diag-

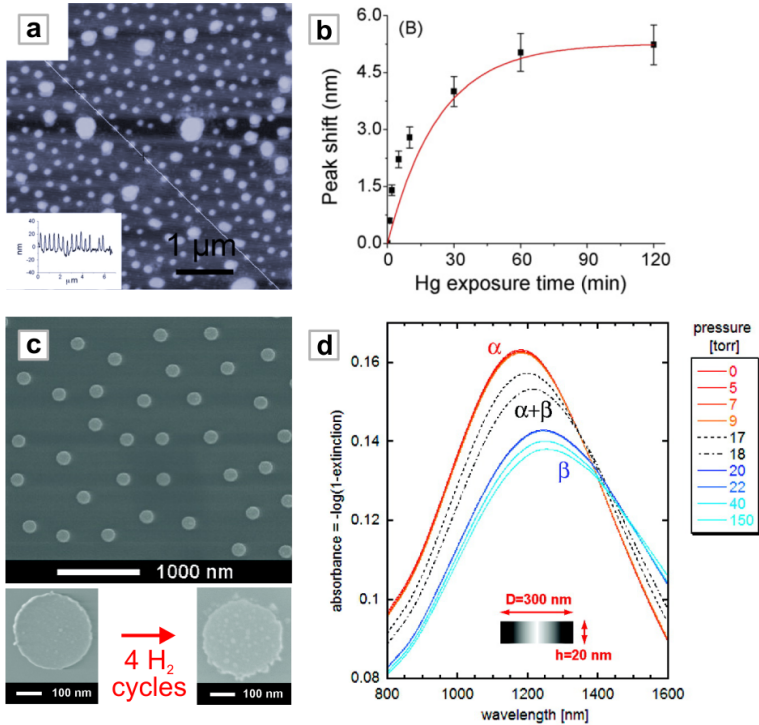


Figure 3.7: Large-area nanostructured sensor chips. (a) AFM image of ordered gold nanoparticle arrays prepared using nanosphere lithography. (b) Plasmon resonance wavelength shifts of the gold nanoparticle arrays at different times after exposure to mercury vapor. (c) SEM image of a Pd nanodisk array used for hydrogen sensing (top) and degradation of the system after several exposure cycles (bottom). (d) Series of measured extinction spectra for the nanodisk array at successively higher hydrogen pressures.

nostics.^{96,97} Their sensor device consisted of an array of triangular silver nanoparticles, covered with a poly(methyl methacrylate) (PMMA) transduction layer which provided the specific reagent sensitivity.⁹⁸

For fabrication, the authors utilized nanosphere lithography followed by spin-coating of the PMMA layer to produce high-quality ordered triangular nanoparticle arrays over large areas. PMMA was chosen as a chloroform sensitive material due to its excellent long-term stability, low optical loss, and transparency in the visible spectrum. In optical extinction measurements, the system exhibited a clear plasmon resonance at a wavelength of around 670 nm, which decreased in magnitude upon exposure to increasing concentrations of chloroform vapor.

Compared to this pronounced response in extinction magnitude, the authors found only small changes in the resonance wavelength for the different chloroform concentrations. This spectral behavior was found to be consistent with chloroform-induced swelling in the PMMA layer. When switching on the chloroform vapor flow, the system reached the saturation value of maximum extinction change after a fast response time on the order of 10 s and the system returned to the initial state 300 s after switching off the flow.

Finally, the authors examined the cross-sensitivity of their sensor device and found only negligible responses for exposures to benzene, toluene, ethanol, propyl alcohol, or hexane. This shows that their system can be utilized as a stable, reliable, and selective chloroform sensor for health and safety or industrial uses.

One key application of large-area nanostructured sensor chips was first demonstrated by Langhammer et al., who utilized palladium nanodisks to perform hydrogen sensing experiments and to study the hydrogen-induced phase transition from palladium (Pd) to palladium hydride (PdH) on the nanoscale.³³ This transition causes both a strong change of the dielectric function and an expansion of the Pd lattice, allowing it to be observed in resonant plasmonic systems.

To achieve this, the authors fabricated a disordered array of supported Pd nanodisks with a diameter of 300 nm using hole-mask colloidal lithography (Fig. 3.7c, top). They then measured

extinction spectra for different hydrogen partial pressures ranging from 0 to 150 Torr. The initial plasmon resonance peak at a wavelength of around 1200 nm underwent a pronounced redshift as well as a broadening and a decrease of the total extinction cross-section for increasing hydrogen pressure (Fig. 3.7d).

By correlating the peak shifts with the hydrogen partial pressures, the authors were able to obtain hydrogen absorption and desorption trajectories comparable to the well-know pressure-composition isotherms that characterize the phase transition in the bulk Pd-H system, showing that the nanoscale phase behavior can be effectively retrieved from optical measurements. They also found that it was crucial to use relative spectral shifts instead of absolute peak positions for the derivation of the pressure-composition isotherms, since repeated hydrogen loading and unloading cycles led to irreversible changes in the Pd nanostructures (Fig. 3.7c, bottom).

Theses changes are due to the phase-transition-induced 10% volume increase of the Pd lattice and the associated mechanical stress.³² For use in highly stable industrial sensor devices, this hydrogen-induced structural deterioration can be overcome by, e.g., alloying Pd with nickel (Ni) and by sandwiching the resulting material in between optimized capping and buffering layers.⁹⁹

The presented nanostructured sensor chips exhibit excellent homogeneity over large areas as well as high performance and can thus serve as the reagent-sensitive element in simple, all-optical, and industry-compatible sensor devices. This enables their use in a variety of applications, especially in the field of environmental monitoring, where high numbers of identical sensor elements are needed.

3.4 COMPLEX GRATING-BASED PLASMONIC HYDROGEN SENSORS

In order to further improve the performance of plasmonic sensor devices, many recent designs have moved from simple plasmonic resonators towards complex coupled or hybrid nanostructures.^{57,100–102} Coupled plasmonic systems provide a way to tackle two main limiting factors for the sensitivity of such devices: the linewidth (and thus the quality factor) of the plasmon resonance and the background signal close to the resonance position.

One approach to reduce the resonance linewidth is to place an array of plasmonic nanowires on top of a photonic waveguide to form a metallic photonic crystal slab.^{103–106} To obtain sensing functionality, Nau et al. used Au nanowires on top of a gasochromic WO_3 waveguide, which undergoes a strong modification of its optical properties when exposed to hydrogen gas.¹⁰⁷ The authors also incorporated an ultrathin (2 nm) catalytic Pd layer between the wires and the waveguide to facilitate the splitting of molecular hydrogen gas into atomic hydrogen for diffusion into the WO_3 waveguide (Fig. 3.8a).

When the system is excited perpendicular to the nanowires, the associated plasmon resonance can couple to the quasiguided mode of the WO_3 waveguide, resulting in the formation of a polariton-type coupled system. In extinction measurements, the upper and lower branch of the polariton can be associated with two pronounced maxima in the spectrum. Additionally, the coupling between the broad plasmon peak and the narrow waveguide mode leads to the formation of a sharp extinction dip between the maxima, which is ideally suited for sensing due to its low FWHM. Upon hydrogen exposure, the optical properties of the WO_3 layer change drastically, which in turn causes pronounced changes in the extinction spectrum of the complete metallic photonic crystal slab.

In their sensing experiments, the authors exposed their sample to a constant gas flow with a predefined ratio of H_2 to N_2 flow rates, allowing them to precisely set the hydrogen concentration. Extinction measurements were taken 100 s after each change of the H_2 concentration to allow the system to reach equilibrium.

In TM polarization, the authors observed a pronounced response of the extinction dip at a wavelength of 674 nm when going from 0 vol.% H₂ to 20 vol.% H₂, with an extinction change of 247 % and a resonance blueshift of 13 nm (Fig. 3.8b).

These results exemplify how the combination of a chemically sensitive waveguide with plasmonic elements can lead to versatile and high-performance sensor geometries. Furthermore, by replacing the Au nanowires with other reactive materials, metallic photonic crystal devices can be expanded to detect two reagents simultaneously, enabling rapid multiplexing.

A different way to obtain narrow spectral features suitable for sensing applications is the coupling of incident light to an array of apertures in an optically thick metal film. In optimized geometries, this leads to a transmittance much greater than predicted from classical aperture theory, a phenomenon known as extraordinary optical transmission (EOT).^{108–110}

In this context, Maeda et al. utilized the infrared transmittance through an array of rectangular subwavelength holes in a palladium film to sensitively detect hydrogen.¹¹¹ The structures were fabricated using electron-beam lithography, metal sputtering, and wet-chemical lift-off to produce hole arrays with a periodicity of 1.1 μm, a length of 0.8 μm, and varying aspect ratios (length/width) from 1 to 2.6 (Fig. 3.8c, aspect ratio 1.6).

In Fourier-transform infrared (FTIR) measurements, the authors found a pronounced transmittance peak that could be tuned from a wavelength of 4 μm up to 5 μm with increasing aspect ratio. Upon exposure to a concentration of 2 vol.% hydrogen, they observed a decrease of the transmittance as well as a spectral redshift of 0.2 μm for a fabricated hole array with an optimal aspect ratio of 1.6. This behavior was confirmed by numerical simulations of the sensing performance, which included both the dielectric change associated with the Pd/PdH transition and the hydrogen-induced expansion of the Pd lattice.

The authors were able to reproduce the plasmon resonance positions for all experimental values of the aspect ratio and found spectral redshifts for both the dielectric change and the lattice expansion, adding up to a total redshift consistent with the experimental data. This shows that, compared to simple Pd patches,

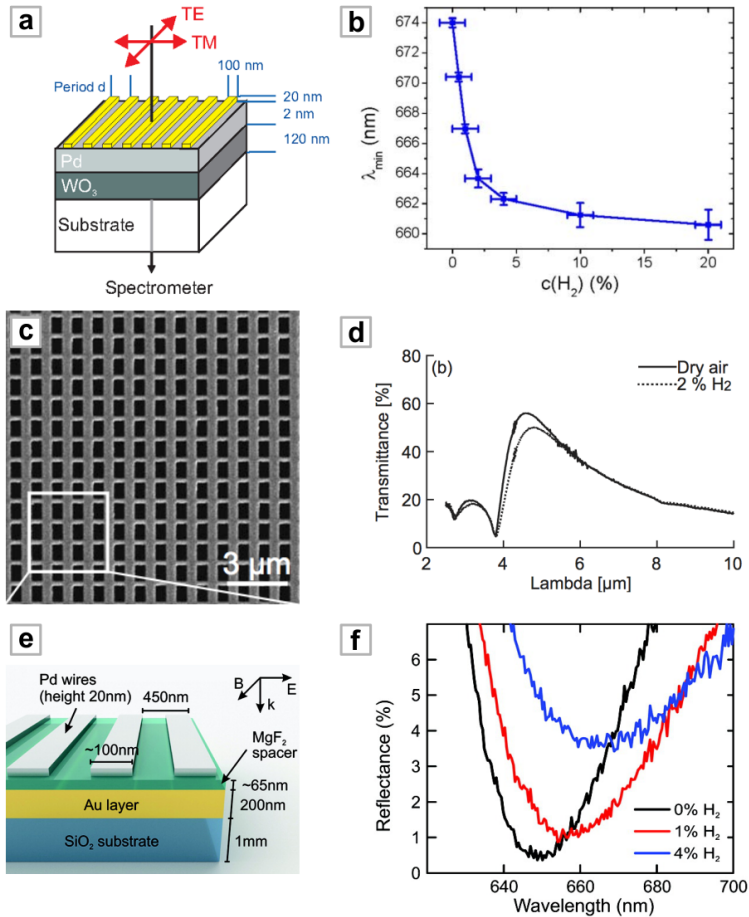


Figure 3.8: Complex grating-based plasmonic hydrogen sensors. (a) Schematic of a metallic photonic crystal slab which incorporates WO_3 as the waveguide layer material. (b) Wavelength shift of the extinction dip in TM polarization for various H_2 concentrations. (c) SEM image of a subwavelength Pd hole array. (d) Transmittance change for a hole array with an aspect ratio of 1.6 when exposed to 2 vol.% H_2 in dry air. (e) Schematic of the palladium-based perfect absorber hydrogen sensor. (f) Reflectance spectra of an optimized perfect absorber structure in N_2 and when exposed to 1 and 4 vol.% H_2 in N_2 .

the use of EOT structures can provide sharp spectral features with large reagent-specific responses and can thus enable highly sensitive sensor devices.

Plasmonic perfect absorber structures, designed to fully absorb incident light of a certain predefined wavelength, can be utilized to reduce the background signals commonly associated with intensity-based sensing approaches. We applied this concept to gas sensing by utilizing a palladium-based perfect absorber structure to detect hydrogen.²³ A detailed discussion of this sensor geometry can be found in section 5.1.

The plasmonic system consisted of an array of Pd nanowires stacked above a dielectric (MgF_2) spacer layer and a gold mirror, which ensures zero transmittance through the structure (Fig. 3.8e). By carefully tuning the width of the Pd wires and the height of the dielectric spacer layer, we were able to tailor both the effective electric permittivity ϵ and the magnetic permeability μ of our structure. This enabled us to match the optical impedance $z = \sqrt{\mu/\epsilon}$ of the coupled system to the vacuum value, resulting in zero reflectance and thus an absorbance of unity.

Following a numerical optimization of the design, the structures were fabricated using electron-beam lithography, thermal evaporation, and wet-chemical lift-off. In optical measurements, we observed a pronounced reflectance dip with a minimum value of $R_0 = 0.5\%$ at the resonance wavelength of $\lambda_0 = 650 \text{ nm}$, which corresponds to an absorbance $> 99\%$. Exposure of this sample to 1 and 4 vol.% H_2 in N_2 carrier gas led to a strong increase of the reflectance at resonance combined with a spectral redshift (Fig. 3.8f).

For the 4 vol.% concentration, which constitutes the explosion threshold of hydrogen in air, a maximum reflectance value of 4.9% at λ_0 and a spectral redshift of 19 nm were observed. Since the initial reflectance at resonance was designed to be practically zero, this translated to a very large relative reflectivity change of $\Delta R_{\text{rel}} = (R_{\text{H}_2} - R_0)/R_0 = 8.8$, an increase of one order of magnitude over conventional thin-film geometries.¹¹²

3.5 ANTENNA-ENHANCED SENSOR GEOMETRIES

Plasmonic nanoantennas can focus incident light into intense hot-spots of the electromagnetic field, making them an essential building block for applications ranging from single molecule fluorescence enhancement to nanoscale photodetection.¹¹³⁻¹¹⁵

The strong nearfields also enable the high sensitivity of such structures towards refractive index changes in, e.g., the nanoscale gap of a plasmonic dimer antenna.^{116,117} Extending this towards catalytic systems, Liu et al. utilized the concept of antenna-enhancement for hydrogen sensing by placing a small palladium disk in the nanofocus of a triangular gold nanoantenna.³⁴

Compared to previous experiments that studied, e.g., resonant plasmonic nanodisks with diameters in the 200 to 300 nm range, the authors were able to examine the hydrogen uptake and release trajectories of Pd particles down to 60 nm in size. The Pd/PdH transition in such small particles is very challenging to detect optically, since the high intrinsic damping of Pd causes the Pd nanoparticles to exhibit a very low optical response at visible wavelengths. Hybrid antenna/disk structures were fabricated using two-step electron-beam lithography, and precise alignment between the two exposure processes was achieved through the use of gold alignment marks. This allowed for the reliable positioning of the Pd disk adjacent to the triangular Au antenna with inter-particle gaps down to 10 nm.

The authors first exposed this optimized sample to controlled cycles of hydrogen gas while recording the optical scattering response from a single antenna/disk structure. They observed a pronounced plasmonic scattering peak at a wavelength of 638 nm, which underwent a spectral redshift of up to 9 nm for exposure to a hydrogen concentration of 16 Torr, equivalent to a concentration of 2 vol.%. When purging the system with nitrogen, a net redshift of 4 nm remained, demonstrating the presence of hysteresis in a single nanoscale Pd/PdH particle.

In a subsequent second exposure cycle, the deterioration of the Pd/PdH particle associated with the hysteresis behavior led to somewhat lower redshifts (Fig. 3.8a). Also, an increase of the antenna-nanoparticle distance caused a severe drop of the sens-

ing performance, again elucidating the important role of strong plasmonic field-enhancement.

The crucial influence of antenna shape was demonstrated by replacing the triangular nanoantenna with a simple Au rod antenna. In this geometry, the authors found that the spectral shifts were roughly half compared to those of the triangular system (Fig. 3.9b), showing that the sharp tip of the single bowtie antenna is essential to obtain an intense nanofocus and consequently high sensitivity.

To investigate the exact reason for the experimentally observed spectral shifts, we performed numerical simulations on the discussed nanoantenna-enhanced sensor geometry.¹¹⁸ A detailed discussion of this study can be found in section 4.1. The hybrid nanoantenna system was modeled using geometrical parameters extracted from the experimental SEM micrographs as well as optical constants for Au and Pd/PdH from literature, and the scattering response of single antenna/disk sensor devices was calculated using a commercial finite element (FEM) electromagnetic field solver. This allowed us to investigate the two main features of the Pd/PdH transition, the dielectric change and the lattice expansion, independently from each other.

We started our investigation by isolating the hydrogen-induced dielectric change, which is the dominant effect for less complex Pd-based sensor geometries.^{119–121} However, when changing the dielectric function of the disk from Pd to PdH, we observed a small blueshift of 3 nm instead of the expected pronounced redshift of 9 nm from experiment. To model the effect of lattice expansion, both the diameter and the height of the Pd nanodisk were scaled with a factor s , ranging from 1.00 (no expansion) to 1.04 (maximum expansion from literature.³²) This led to a linear redshift of the plasmon resonance peak, with a maximum value of 13 nm for a scaling of 1.04 (Fig. 3.9c). By combining this scaling with the dielectric function of PdH, we were able to fully reproduce the experimental results.

Additionally, the two competing spectral effects exhibited a markedly different scaling behavior: the blueshift associated with the dielectric change in the Pd remained mostly constant at 3 nm, whereas the redshift induced by the disk's scaling could be tuned

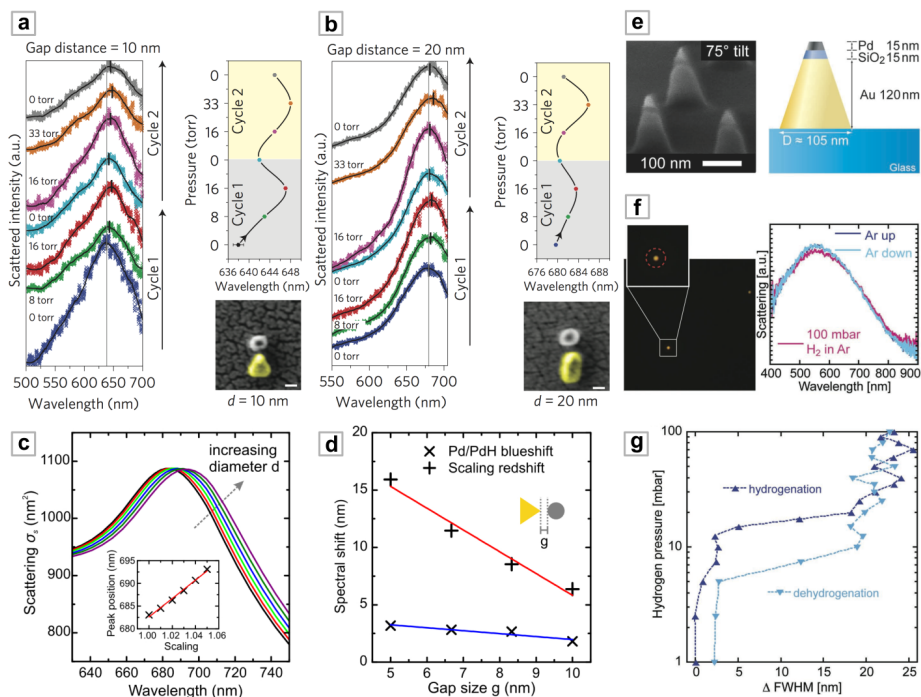


Figure 3.9: Antenna-enhanced sensor geometries. (a) Optical scattering measurements and plasmon resonance shifts for a single palladium-gold triangle antenna during two hydrogen uptake and release cycles. (b) Hydrogen-dependent measurements for a single palladium-gold rod antenna. (c) Numerically calculated single particle scattering spectra for different diameters of the Pd disk next to the triangular Au antenna (initial gap size $g = 7$ nm). (d) Resonance shifts due to the Pd/PdH transition and the growing of the Pd disk for different initial gap sizes g . (e) SEM image and schematic depiction of a 120 nm high, truncated Au nanocone with a 15 nm SiO₂ spacer layer and a Pd particle on the tip. (f) Dark-field optical image of a single nanocone (left) and its spectral response to 100 vol.% Ar, 10 vol.% H₂ in Ar, and 100 vol.% Ar (right). (g) Corresponding optical isotherm of the nanocone system during hydrogenation.

via the gap size (Fig. 3.9d). Furthermore, it was found that, in contrast to the single antenna systems, a double rod antenna geometry yielded spectral shifts comparable to a double bowtie geometry, elucidating how the strong field-enhancement in the feed gap can become dominant over the shape of the constituent elements.

Still, the precise relative positioning of particles with different material properties and the required multi-layer processing pose significant challenges for high-throughput fabrication. To alleviate this, Langhammer et al. have utilized hole-mask colloidal lithography to fabricate truncated gold nanocones with functionalized tips to detect the hydrogen sorption and desorption kinetics of palladium and magnesium (Mg) nanoparticles.³⁵

Au nanocone antennas with different truncation height and consequently tip sharpness were fabricated and subsequently covered with a SiO₂ spacer layer and the reactive material in question. For a nanocone height of 120 nm, a 15 nm spacer layer, and a 15 nm thick tip, the authors were able to obtain an antenna-enhanced system with a Pd particle only 30 nm in size (Fig. 3.9e), a factor of 2 smaller than in the experiment by Liu et al.³⁴ Still, the authors were able to detect the optical scattering response from single nanocones and could observe clear and reversible shifts of the plasmon scattering peak when exchanging the gaseous environment from 100 vol.% Ar to 10 vol.% H₂ and back to Ar (Fig. 3.9f).

To further study the phase-transition behavior in the Pd nanoparticle, complete isotherms for hydrogenation and dehydrogenation were recorded at different temperatures. Especially, the authors chose to track the full width at half maximum (FWHM) of the plasmon peak vs. the hydrogen partial pressure instead of the more common spectral shift or peak intensity change, allowing them to observe a clear hysteresis behavior from a single 30 nm Pd particle coupled to a Au nanocone antenna (Fig. 3.9g).

Using Van't Hoff analysis, they were able to extract the enthalpy and entropy of hydride formation from the isotherm measurements, indicating a destabilization of the PdH phase compared to the bulk material. Furthermore, the authors extended the nanocone concept to the study of the hydrogenation kinetics

of a single Mg nanoparticle. To prevent alloying and to isolate the Mg particle from neighboring materials, it was placed between two titanium (Ti) layers, with a thin catalytic Pd layer placed at the top of the structure. This system configuration allowed the authors to trace a full hydrogenation isotherm for a single Mg nanodisk with a diameter of only 35 nm, demonstrating the versatility of their detection scheme.

By implementing such advanced, high-throughput fabrication methods, complex plasmonic sensing geometries can be transitioned from high-resolution single-particle spectroscopy towards large-scale technological applications, allowing for the sensitive, robust, and cost-effective detection of a variety of reagents and chemical processes.

SINGLE PLASMONIC NANOPROBES FOR SENSITIVE TRACE GAS DETECTION

4.1 SPECTRAL SHIFTS IN ANTENNA-ENHANCED HYDROGEN SENSING GEOMETRIES

One of the main driving forces of plasmonics research is the realization of plasmonic sensing in ultra-small volumes.^{8,122–124} Initially, this was led by the promise of obtaining spectroscopic fingerprints of only few molecules in surface enhanced Raman scattering (SERS).

More recently, the development of coupled bright and dark plasmonic structures has allowed the production of more sensitive geometries that even allow for the sensing of minute refractive index changes in very small volumes.¹⁴ In both cases, the large field-enhancements obtained near the surface of resonant metallic structures are the enabling effects.

In general, these resonant metallic structures can be regarded as optical nanoantennas,^{61,125} and the sensed material as equivalent to an antenna-driven circuit in electronics. This view gives rise to the recognition that sensing cannot only be carried out on dielectric substances but also on non-resonant metallic structures. This is especially useful in cases where particles are too small to have a significant scattering cross-section^{34,126} or where the inherent damping of the metal prevents strong plasmonic resonances. The latter is the case in the optical detection of hydrogen in palladium.¹²⁷

This section discusses the nature of spectral shifts in antenna-enhanced hydrogen sensing geometries consisting of a gold bow-tie antenna next to a palladium nanodisk.* The presented investigation is carried out through extensive finite element (FEM)

* This section is adapted from A. Tittl et al., *Spectral shifts in nanoantenna-enhanced hydrogen sensors*, *Optical Materials Express* **2**, 111–118 (2012). Reprinted with permission. Copyright 2012 Optical Society of America.

simulations and it is found that the hydrogen-induced spectral behavior of the system is governed by two competing effects: a small blueshift caused by dielectric changes in the palladium and a much stronger redshift due to an expansion of the palladium lattice. The presented findings enable the accurate numerical characterization and especially the optimization of sensitive antenna-enhanced hydrogen sensors.

The optical detection of hydrogen is of particular interest for two applications: the detection of explosive mixtures of hydrogen with air at concentrations ranging from 4 to 75 vol.%, and the investigation of loading/unloading kinetics of hydrogen in nanostructured materials, e.g., for fuel cell applications. Many examples of plasmonic hydrogen sensing have already been proposed.¹²⁸ Palladium (Pd) serves as an ideal material for realizing these two goals since it is one of the simplest model systems for the incorporation of hydrogen in metal lattices.³²

In order to investigate palladium kinetics on minute length scales and for very low concentrations, a move from conventional designs relying on extended films¹²⁹ or arrays of plasmonic elements¹¹¹ towards single structures is desirable.¹³⁰ However, the use of, e.g., simple single Pd nanodisks is precluded by the large intrinsic damping and the resulting broad resonance profile as well as low scattering efficiency. Antenna-enhanced geometries can overcome these problems by coupling a highly resonant antenna to the system under investigation which can greatly enhance nanoscale optical effects.^{126,131}

The application of this approach to hydrogen sensing has been demonstrated experimentally by Liu et al. through the coupling of a single gold bowtie antenna to a Pd nanodisk.³⁴ Unfortunately, in their paper no theoretical simulations of optical spectra were included. However, numerical modeling is crucial for the efficient design and optimization of an optical sensor geometry. Furthermore, simply using the dielectric functions for Pd and hydrided Pd given by Vargas et al.¹²⁷ in simulations will result in a spectral blueshift upon hydrogen exposure. Contrary to this, Liu et al. experimentally observed a redshift.

In the following, theoretical modeling and numerical simulations are used to understand the underlying physics responsible

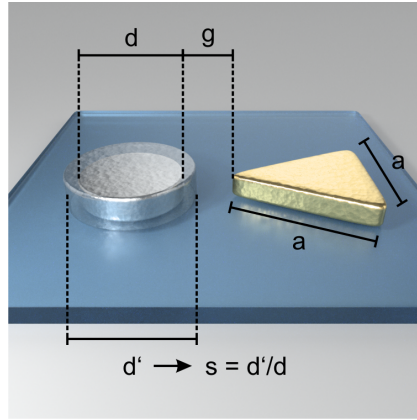


Figure 4.1: Schematic view of the system under consideration. Pd disk with diameter $d = 60$ nm and height 40 nm situated next to a single gold bowtie antenna with side length $a = 108$ nm and height 40 nm.

for the observed spectral shifts and resolve the apparent discrepancy. By not only including the index of refraction change but also the volume expansion of Pd, for the first time, we are able to model the sensing behavior of the experimentally investigated Pd disk and gold antenna system. In addition, we show how adding a second antenna arm can substantially improve the sensing performance.

The antenna enhanced system under consideration is shown in Fig. 4.1a and consists of a single gold bowtie antenna (side length $a = 108$ nm, height 40 nm) separated by a gap g from a Pd disk (diameter $d = 60$ nm, height 40 nm) on a SiO_2 substrate.

The system is similar to the one in Ref.³⁴, where the authors manufacture this structure using electron-beam lithography and record dark-field scattering spectra of single antenna-enhanced sensor elements. In the absence of hydrogen they find a strong scattering maximum associated with the antenna-resonance at a wavelength of 638 nm. When exposed to a concentration of 1 vol.% hydrogen in nitrogen, the resonance undergoes a redshift of 5 nm as well as a strong decrease of the scattering amplitude and significant broadening. An increase of the concentration to 2 vol.% in nitrogen yields a total redshift of 9 nm as well as fur-

ther broadening. The observed effect is mostly reversible, showing some hysteresis due to the hydrogen loading/unloading.

When Pd is exposed to hydrogen gas, the molecules are split at the surface and atomic hydrogen enters the Pd lattice. At low concentrations the hydrogen forms a solid solution in the host lattice, the so-called α -phase. For higher concentrations a less mobile palladium-hydride (PdH) β -phase with increased lattice parameter is formed. Starting from impurities or lattice defects the β -phase forms domains and for very high concentrations most of the system is converted, leading to a pronounced increase of the lattice constant by as much as 4%.³² In the following, PdH will always refer to the hydride system with a H/Pd atomic ratio of 0.82 as given in literature.¹²⁷

Concurrent to the hydride-formation the dielectric function of Pd is also modified. This is caused by an electron transfer from the hydrogen atoms to the electronic system of Pd, changing the density of states at the Fermi-surface.³⁰ This change substantially modifies both the real and imaginary part of the dielectric function of Pd.

A qualitative explanation for the effect of antenna-enhanced hydrogen sensing is that the hydrogen-induced changes of the dielectric function and the lattice constant of Pd are enhanced by the antenna resonance, leading to a redshift. In order to obtain a more quantitative understanding and enable optimization of this sensor structure, detailed numerical analysis is desirable.

The numerical analysis has been performed using the HFSS (High-frequency structure simulator, ANSYS Inc.), a commercial finite element (FEM) electromagnetic field solver. Pd, PdH and gold are described using tabulated refractive index data given in literature.^{127,132} The permittivity of the SiO₂ substrate is taken as 2.25. The footprint of the single gold bowtie antenna is a regular triangle with side length $l = 116$ nm where the corners are rounded with 5 nm radius, resulting in an effective bowtie side length of $a = 108$ nm.

The top edge of the bowtie as well as of the cylinder is rounded with 2.5 nm radius. The whole system is surrounded by a perfectly matched layer (PML) where the substrate extends into the PML. The detector was placed parallel to the substrate surface

at 1500 nm distance and spans a solid angle Ω . The integrated differential scattering cross-section σ_s used in the following discussion is given by

$$\sigma_s(\Omega) = \frac{\iint_{A_{\text{det}}} \mathbf{S}_s \cdot \hat{\mathbf{n}} \, dA}{|\mathbf{S}_{\text{inc}}|} \quad (4.1)$$

where the surface integration is performed over the detector area A_{det} with surface normal $\hat{\mathbf{n}}$. Here \mathbf{S}_s and \mathbf{S}_{inc} are the Poynting vectors of the scattered and incident fields, respectively.

The main advantage that simulations offer compared to experiments is the possibility to study different effects related to material property changes independently from each other. We start with the change of dielectric function for a gap size of $g = 5$ nm in the top row of Fig. 4.2. The first surprising result is that a change of the dielectric function of the disk from Pd to PdH results in the expected amplitude decrease and spectral broadening but combined with a blueshift of 3 nm instead of a redshift.

What looks like a contradiction to the experimental results of Ref.³⁴ can be resolved by considering the hydrogen-induced lattice expansion in the Pd disk. It can be modeled in a simple way by multiplying both the diameter and the height of the disk with a scaling factor s . Due to the large field-enhancement in the area between the antenna and the disk (Fig. 4.3a), the system should be extremely sensitive to the decreasing gap size associated with this scaling.

Figure 4.3b shows the influence of scaling on the antenna resonance for a gap size of 7 nm. We observe a redshift linear in scaling that reaches a maximum of 7 nm for a value of $s = 1.04$ while the scattering amplitude and linewidth remain mostly constant. The scaling parameter ranges from 1.00 to 1.05, chosen in accordance with PdH values of $s = 1.038$ given in literature.³²

The two competing effects of dielectric function mediated blueshift and lattice expansion induced redshift can be clearly identified in Fig. 4.2. Whereas the dielectric change causes a blueshift of 3 nm and a strong broadening of the resonance, the scaling by a factor of $s = 1.04$ induces a redshift of 13 nm. The superposition of these contributions results in a total redshift of 10 nm with a

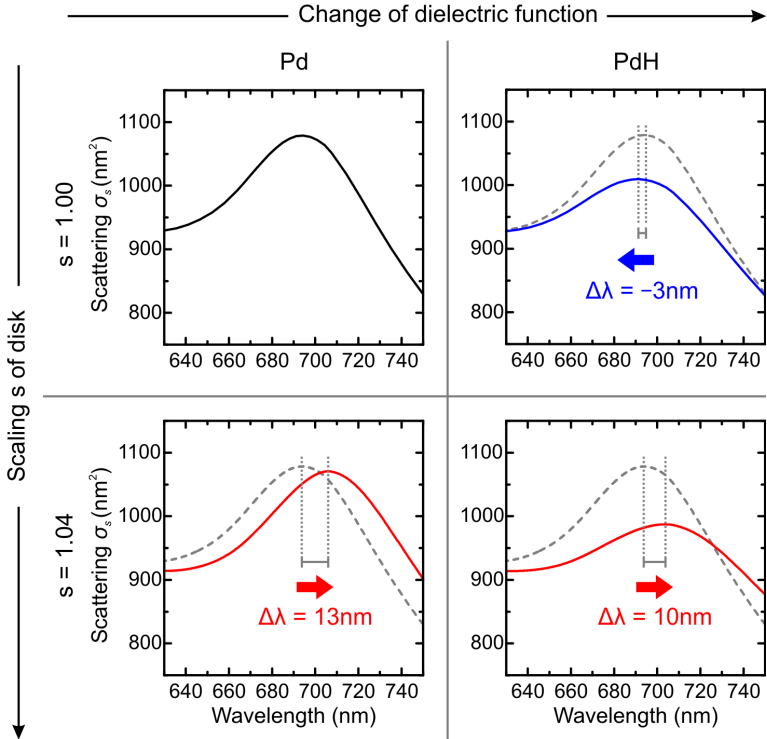


Figure 4.2: Calculated scattering spectra for two values of the dielectric function of the Pd disk and scaling factor s , respectively. The gap size g before scaling is fixed at 5 nm. A change of the dielectric function from Pd to PdH blueshifts the antenna resonance by 3 nm, whereas scaling the Pd disk with a factor of $s = 1.04$ causes a redshift of 13 nm. The superposition of these two competing effects yields a total redshift of 10 nm.

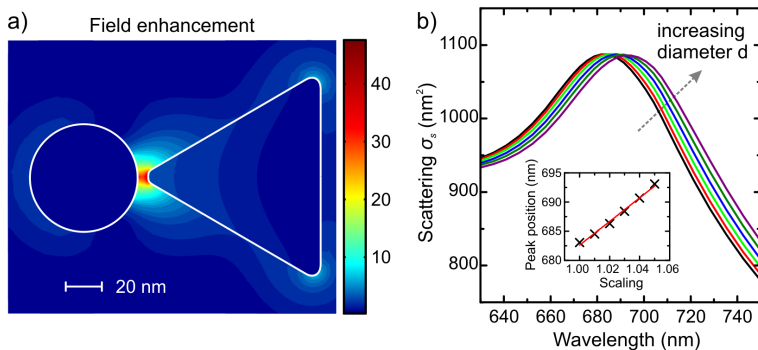


Figure 4.3: (a) Calculated enhancement of the electric field on a plane parallel to the substrate through the center of the bowtie. (b) Calculated single particle scattering spectra for different antenna disk diameters and a gap size $g = 7$ nm. Note the linear redshift of the antenna resonance with increasing scaling factor s .

simultaneously broadened lineshape. This behavior agrees very well with the experimental data in Ref.³⁴.

To examine the influence of gap size on the magnitude of these two effects we calculated scattering spectra for different gap sizes and the parameter cases described in Fig. 4.2. A markedly different scaling behavior of the two competing effects can be observed in Fig. 4.4. Whereas the blueshift induced by the dielectric change in the Pd remains mostly constant at 3 nm, the redshift associated with the disk's scaling can be tuned by changing the gap size. This scaling behavior enables the tailoring of the total hydrogen-induced redshift.

Although we are able to numerically reproduce the direction of hydrogen-induced spectral shifts and the concurrent resonance broadening, there are still differences in magnitude between our simulated results and the experimental data reported in Ref.³⁴. These differences are most probably due to deviations in gap size between the antenna and the disk as well as strain effects between the structures and the substrate which are neglected in our numerical calculations.

Still, our approach allows us to numerically explore optimized nanoantenna-enhanced hydrogen sensor geometries. A straightforward way to increase the sensitivity is to add a second antenna

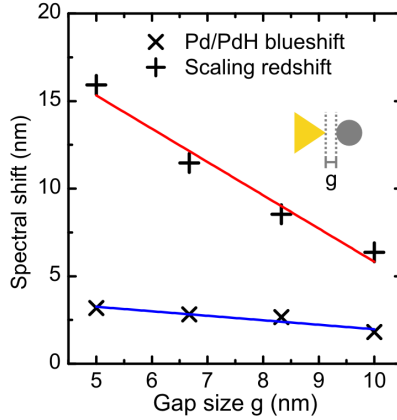


Figure 4.4: Extracted spectral shifts due to the Pd/PdH transition and the growing of the Pd disk for different initial gap sizes g . Whereas the Pd/PdH-induced blueshift remains mostly constant at 3 nm, the magnitude of the scaling-induced redshift can be tuned by varying the gap size.

arm to the current design. To demonstrate this, we simulate a Pd nanodisk in the center of a full bowtie antenna (Fig. 4.5a).

Figure 4.5b shows that the total hydrogen-induced redshift is more than doubled by adding a second bowtie antenna opposite the first. However, this addition also redshifts the resonance by 52 nm and thus requires a different figure of merit to accurately compare the two designs. Since the full width at half maximum (FWHM) of our simulated spectra is difficult to determine due to the asymmetric lineshape, we calculate and compare the $\text{FOM}_\lambda = (\Delta\lambda/\Delta n)/\lambda_0$ in analogy to the $\text{FOM}^* = (\Delta I/\Delta n)/I_0$ defined by J. Becker et al. for plasmonic sensing using nanoholes.¹³³ In our case, λ_0 is the resonance position and the refractive index change can safely be set to $\Delta n = 1$ for the purpose of comparing similar hydrogen sensing geometries.

We obtain values of $\text{FOM}_\lambda = 1.4 \cdot 10^{-2}$ for the single bowtie and $\text{FOM}_\lambda = 3.5 \cdot 10^{-2}$ for the double bowtie geometry with an enhancement factor of 2.4. This strong enhancement can be understood in terms of the field enhancement in both geometries (Fig. 4.3a and 4.5a). Although the maximum enhancement is similar for both systems, the double-bowtie geometry includes two

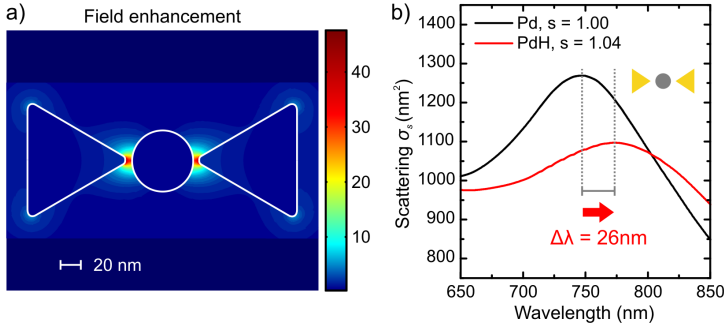


Figure 4.5: (a) Calculated enhancement of the electric field on a plane parallel to the substrate through the center of the double-bowtie system. (b) Calculated scattering spectra for a double-bowtie geometry with center Pd disk and a gap size of $g = 5$ nm. A significant enhancement of the total redshift can be observed.

hot spots of the electric field where the system is highly sensitive to the scaling of the center disk. This field concentration in the feed gap of an antenna pair is responsible for the strongly increased redshift that we observe.

Interestingly, this increase of the spectral shift should be even more pronounced in an antenna geometry that does not exhibit field focusing behavior on its own.

To explore this, we consider a gold cutwire (cuboid) antenna (width 60 nm, length 97 nm, height 40 nm) separated by a gap of $g = 5$ nm from the palladium disk. The length of the cutwire was chosen to match its resonance position to the single bowtie results from Fig. 4.2.

Since the field hot spots of a single cutwire antenna are located at its corners away from the Pd disk,³⁴ we expect a decreased spectral shift compared to the single bowtie geometry. Figure 4.6a shows that the cutwire system indeed exhibits a much lower redshift of 5 nm when moving from Pd to PdH and scaling the disk by a factor of $s = 1.04$. This is again in excellent agreement with the experimental results.

However, when considering a double-cutwire geometry by adding a second antenna arm to the system, we observe a large redshift of 28 nm (Fig. 4.6b), comparable to the double-bowtie geom-

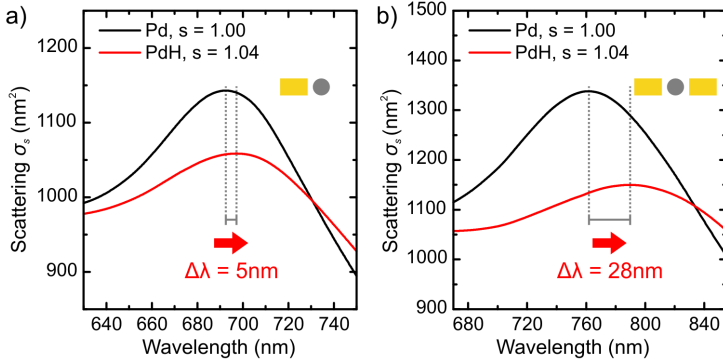


Figure 4.6: (a) Calculated scattering spectra for a cutwire antenna situated next to a Pd disk with a gap size of $g = 5$ nm. (b) Calculated scattering spectra for a double-cutwire geometry with center Pd disk and a gap size of $g = 5$ nm. A significant enhancement of the total redshift comparable to the double-bowtie geometry can be observed.

etry. This shows that in contrast to single antennas, spectral shifts in double-antenna geometries are governed less by the shape of the antenna and more by the field enhancement created in the feed gap between the two antenna arms.

In summary, we have numerically investigated hydrogen-induced spectral shifts in antenna-enhanced hydrogen sensing geometries and found two competing effects: a blueshift attributed to the change of the dielectric function in Pd that is mostly unaffected by changes in gap size and a lattice-expansion induced redshift that can be tailored by changing the gap size. The insight we gained into the behavior of this system enables us to accurately model antenna-enhanced hydrogen sensors. The numerical characterization of structures with an added second antenna arm shows that this is a straightforward way to improve the sensing performance. Our modeling allows further optimization beyond simple antenna geometries and thus paves the way towards the realization of extremely sensitive plasmonic hydrogen sensors.

4.2 PLASMONIC SMART DUST FOR PROBING LOCAL CHEMICAL REACTIONS

Locally probing chemical reactions or catalytic processes on surfaces under realistic reaction conditions has remained one of the main challenges in materials science and heterogeneous catalysis.

Where conventional surface interrogation techniques usually require high-vacuum conditions or ensemble average measurements, plasmonic nanoparticles excel in extreme light focusing and can produce highly-confined electromagnetic fields in sub-wavelength volumes without the need for complex near-field microscopes.

This section introduces an all-optical probing technique based on plasmonic smart dust for monitoring local chemical reactions in real time.* The silica shell-isolated gold nanoparticles which form the smart dust can work as strong light concentrators and optically report subtle environmental changes at their pinning sites on the probed surface during reaction processes.

As a model system, we investigate the hydrogen dissociation and subsequent uptake trajectory in palladium with both “dust-on-film” and “film-on-dust” platforms. Using time-resolved single particle measurements, we demonstrate that our technique can in-situ encode chemical reaction information as optical signals for a variety of surface morphologies. The presented technique offers a unique scheme for real-time, label-free, and high-resolution probing of local reaction kinetics in a plethora of important chemical reactions on surfaces, paving the way towards the development of inexpensive and high-output reaction sensors for real-world applications.

Conventional probing methods often rely on ultra-high vacuum conditions.^{134,135} Scanning tunneling microscopy, for example, offers a unique tool to gain insight into well-defined reaction systems, but has difficulties to provide pervasive information at realistic reaction conditions. Surface-enhanced Raman spectroscopy is a powerful alternative to characterize the kinet-

* This section is adapted from A. Tittl et al., *Plasmonic smart dust for probing local chemical reactions*, *Nano Letters* **13**, 1816-1821 (2013). Reprinted with permission. Copyright 2013 American Chemical Society.

ics of chemical reactions.¹³⁶ However, the interpretation of Raman spectra can be time-consuming as trace contaminants may contribute additional peaks. Tip-enhanced Raman spectroscopy (TERS) allows for the investigation of arbitrary substrates.^{137,138}, but suffers from weak Raman scattering signals^{139,140} Also, the fabrication of robust, reproducible, and highly enhancing tips is still challenging. Thus, there is a critical unmet need for sensitive, robust, and easy to implement techniques to probe local chemical reactions while they occur under diverse environmental conditions.

Plasmonic nanoparticles can concentrate light into a nanoscale volume, converting incident optical radiation into highly localized electromagnetic fields at a prescribed spot with subdiffraction-limit size.⁶¹ In recent years, plasmonics has also branched out into other research fields, tackling intriguing problems in pharmacology, biology, and chemistry, among others.^{9,128,141}

Particularly, large near-field enhancements have been shown to significantly increase the efficiency of photocatalytic water splitting for hydrogen production, laying the groundwork for solar to chemical energy conversion.¹⁴² Burning hydrogen produces no pollutants, making it ideal for clean energy storage and conversion in an economy increasingly based on green fuels. Consequently, safe chemical hydrogen storage requires the sensitive and reliable detection of hydrogen uptake in such materials.¹²⁸

The plasmonic smart dust used in this study consists of chemically grown SiO₂ shell (10 nm) isolated Au nanoparticles (150 nm). To produce the complex core-shell nanoprobles, Au nanoparticles with a target diameter of 150 nm were first synthesized by a two-step seed-mediated growth method. Starting from seed Au nanoparticles with a diameter of 40 nm prepared using a standard citrate reduction method, the seeds were grown to a diameter of 150 nm using HONH₃Cl as a reducing agent at room temperature.

The obtained 150 nm Au nanoparticles were used for the subsequent silica coating process.¹⁴³ Typically, a certain amount of freshly prepared aqueous solution of 0.5 mM (3-Aminopropyl) triethoxysilane (APTES) was added to the Au sol under vigorous magnetic stirring in 20 minutes. Then the pH of a 0.54 wt.%

sodium silicate solution was adjusted in the range of 10.3 to 10.5 using 0.2 M H_3PO_4 solution added upon fast shaking. 2.8 ml of the acquired sodium silicate solution was added to the Au sol under stirring at room temperature.

Five minutes later, the mixture was placed in a 100 °C water bath with continuous stirring. After 60 min, the same amount of pH adjusted sodium silicate solution was again added to the sol and the mixture was continually heated for another 60 min, after which the mixture was cooled in an ice bath to stop the reaction.

Figure 4.7b presents an exemplary transmission electron microscopy (TEM) image of such a smart dust nanoparticle. The energy-filtered TEM image using the Si L-edge of the same particle is shown in Fig. 4.7c in which the Au core and the SiO_2 shell can be nicely distinguished. The key virtue of our plasmonic smart dust is its uniform and ultra-thin SiO_2 shell, which allows the Au core to generate strong electromagnetic near-fields and simultaneously protects it from the chemical environment.

The scattering spectra of single plasmonic smart dust particles are recorded in-situ by dark-field microscopy. Importantly, the ultra-thin SiO_2 shell of the smart dust separates the Au core from direct contact with the probed agents. This constitutes a clear advantage of our platform over TERS-based methods that require complex tip-to-sample approaches, whereas our smart dust can simply be spread onto a catalytic or reactive surface.

Our method also allows for simultaneous imaging of chemical processes at different reaction sites, combining indirect plasmonic sensing³⁴ and the highly uniform core-shell nanoprobe previously developed for SERS enhancement.¹⁴³ Furthermore, the smart dust particles can work as resonant antennas whose plasmon resonance can be tuned to the excitation wavelength of a probing laser.

To demonstrate the versatility of our approach for diverse surface morphologies, two representative probing platforms are investigated: “dust-on-film”, where the plasmonic smart dust is dispersed on a thin Pd film, and “film-on-dust”, where the smart dust is covered with a highly curved Pd film. In both cases, careful dilution and drop-coating of the smart dust yield sam-

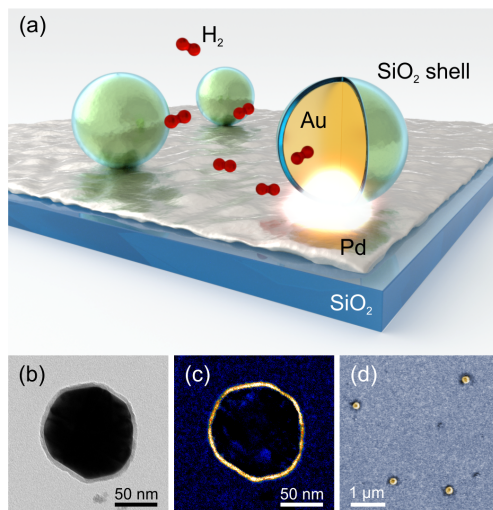


Figure 4.7: Plasmonic probing of local chemical reactions. (a) Sketch of the probing platform. Plasmonic smart dust (shell-isolated Au nanoparticles) are spread on a thin Pd film to locally probe diffusion of atomic hydrogen in Pd. (b) Exemplary TEM bright-field image of a smart dust nanoparticle deposited on a carbon membrane. (c) Energy-filtered TEM image using the Si L-edge of the same nanoparticle. The orange color indicates the presence of Si. The homogeneity of the ultra-thin SiO₂ shell is excellent. (d) Exemplary SEM image of the smart dust deposited on a 15 nm thick Pd film via drop-coating. The particle separations are ideal for single-particle spectroscopy.

ples with inter-particle distances suitable for single-particle spectroscopy (Fig. 4.1d).

We first investigate the “dust-on-film” platform as shown in the inset of Fig. 4.8a. Here, the smart dust nanoparticles are dispersed on a thin Pd film, which resides on a quartz substrate. After placing the sample in a stainless-steel reaction chamber, the concentration of hydrogen during the reactions is controlled by tuning the ratio of high-purity hydrogen and nitrogen gas through mass-flow controllers.

The hydrogen uptake processes are probed in-situ by recording the scattering spectra of single smart dust particles using a Nikon TE2000UE inverted microscope combined with a Roper Scientific SP-2500i spectrograph and a Peltier-cooled PIXIS 256E

CCD-camera. Spectra were taken in transmission and using linearly polarized incident light. The samples were placed into a home-built titanium sensor chamber connected to a mass-flow system that allowed for the precise control of the hydrogen concentration in the chamber. All presented experimental spectra were taken with an integration time of 8 s, with one spectrum recorded every 10 s.

Figure 4.8a shows the complete time-resolved optical response of a single smart dust particle on a 15 nm Pd film at different hydrogen concentrations. Upon introducing hydrogen into the reaction chamber at concentrations as low as 0.5 vol.%, the resonance of the smart dust particle at roughly 600 nm shows an immediate response both in intensity and wavelength position, indicating the onset of hydrogen molecule dissociation and subsequent atomic hydrogen diffusion into the Pd.

More specifically, the plasmonic resonance shifts to the blue and its intensity increases. Hydrogen uptake in Pd leads to a phase transition, turning it into more semiconductor-like than metal-like, which is manifested in a pronounced change of the dielectric function.^{32,127}

Due to the strong electromagnetic near-fields associated with the plasmon excitation, the smart dust particle can capture this information arising from the chemical reactions at its specific location and converts it into optical spectral changes. As a result of the evanescent nature of particle plasmons, the smart dust particle works as a point probe which only conveys the hydrogen uptake information in a confined subwavelength sensing volume at its location. The information beyond this sensing volume is fully discarded, making it an ideal local reaction reporter.

To test the ability of our plasmonic smart dust for resolving different hydrogen contents in Pd, the sample is repeatedly exposed to hydrogen concentrations ranging from 0.5 vol.% to 3 vol.%. As shown in Fig. 4.8a, different hydrogen concentrations can be identified as intensity changes of the plasmonic resonance, with response times on the order of seconds. The observed fast reaction kinetics compared to bulk palladium systems are due to the shorter diffusion lengths associated with Pd thin films and nano-materials.¹⁴⁴ In general, higher hydrogen concentrations lead to

increased resonance intensity and spectral blue-shift of the resonance position.

To resolve the small spectral shifts associated with low hydrogen concentrations, we employ a centroid analysis method.¹⁴⁵ In contrast to simply tracking the scattering spectral maximum, the centroid method computes the “center of mass” of the scattering spectrum, providing a highly reliable way to determine the resonance wavelength position.

To carry out this analysis, we first chose a wavelength span of $S = 150$ nm approximately centered at the maximum of the scattering intensity $I(\lambda)$. The data in this range was then fitted using a polynomial $p(\lambda)$ of degree 20 in accordance with literature.¹⁴⁵ The centroid wavelength λ_c was then calculated using

$$\lambda_c = \frac{\int_{\lambda_0}^{\lambda_0+S} \lambda [p(\lambda) - p_0] d\lambda}{\int_{\lambda_0}^{\lambda_0+S} [p(\lambda) - p_0] d\lambda} \quad (4.2)$$

where λ_0 denotes the starting wavelength of the centroid span and $p_0 = p(\lambda_0)$ is a constant background that can be subtracted. In addition, a bootstrapping approach^{146,147} is used to estimate the statistical error (standard deviation) of the retrieved centroid wavelength position.

To demonstrate the spatially confined nature of our plasmonic probes, we alter the local environment of the plasmonic smart dust by using a thinner Pd film (10 nm). We compare the time-resolved centroid wavelength position changes under the same reaction conditions for samples with 10 and 15 nm Pd films, respectively (Figs. 4.9a,b). In both cases, clear shifts of the resonance position are observed upon hydrogen uptake and release. The 15 nm Pd sample displays a much more pronounced optical response compared to the 10 nm Pd sample at identical hydrogen concentrations. More specifically, the former exhibits a pronounced blue-shift as large as 8 nm at 3 vol.%, whereas the latter only leads to half of this blue-shift value.

A Pd film thickness change of 5 nm already suffices to induce a notable influence on the hydrogen storage behavior. In turn, this elucidates that our plasmonic smart dust can optically resolve the difference of hydrogen uptake processes arising from extremely

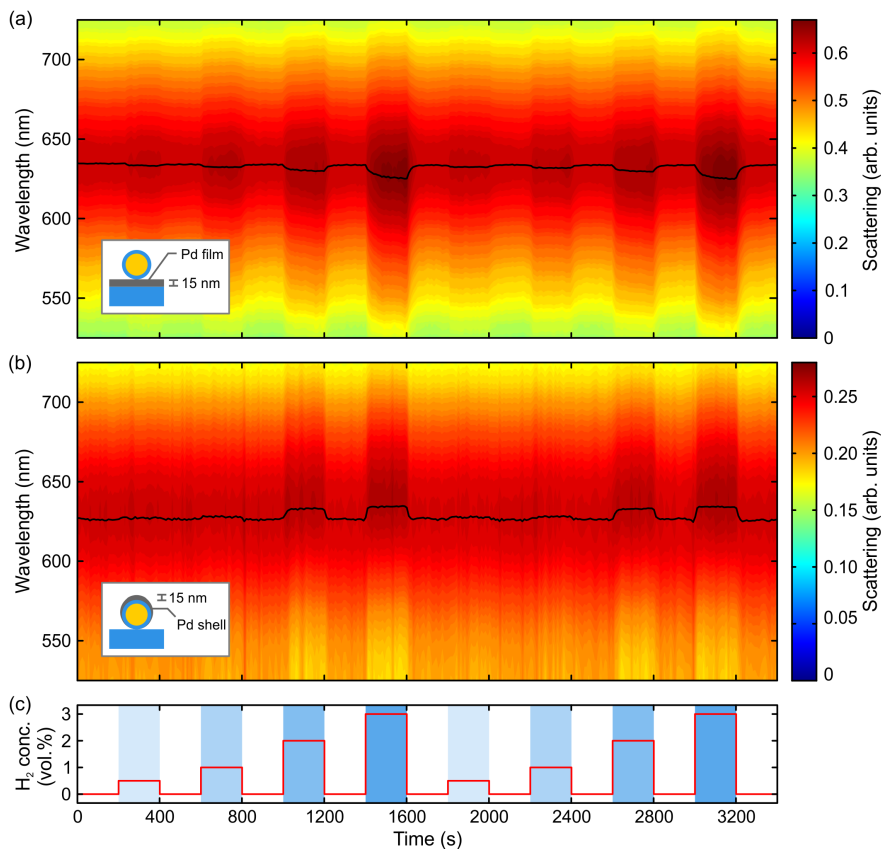


Figure 4.8: Optical trajectories of local hydrogen uptake and release. Color-coded spectral scattering intensity over time. (a) “dust-on-film”, single smart dust particle on a 15 nm Pd film. (b) “film-on-dust”, single smart dust particle covered by a 15 nm Pd film. In both cases, the black lines denote the centroid wavelengths and serve as guides to the eye. The plasmonic smart dust detects the local chemical reactions and converts the information into optical signal changes, which are manifested in resonance intensity and resonance position with a response time on the order of seconds. The single particle measurements are carried out using dark-field microscopy in real time. (c) Concentration of hydrogen in nitrogen carrier gas during the reactions.

small environmental changes at its probing site. This is of great importance for studies of heterogeneous catalysis, where local structural characteristics such as size, shape, geometry, and surface morphology of catalysts are crucial. For gaining a broader view, the plasmonic smart dust may be used to produce a local reaction map by pinning multiple nanoparticles at reaction sites of interest and optically monitoring spatially distinct local chemical reactions simultaneously.

To further demonstrate the ability of our plasmonic smart dust to probe local chemical reactions for more complex surface morphologies, we investigate the second sensor platform: “film-on-dust” (see the inset of Fig. 4.8b). The plasmonic smart dust is dispersed on a quartz substrate and a Pd film (15 nm) is evaporated on the nanoparticles through tilted angle evaporation, forming a highly-curved Pd surface on the particles. The sample is then placed in the reaction chamber. The experimental procedures are the same as those in Fig. 4.8a, and results are plotted in Fig. 4.8b and Fig. 4.9c for the same smart dust particle. All concentration steps are again clearly identified through the changes of the optical response.

The resonance intensity does not change as dramatically as that in the “dust-on-film” configuration. Still, the resonance exhibits a pronounced 8 nm red-shift at a hydrogen concentration of 3 vol.%. Strikingly, the direction of the spectral shift is reversed with respect to the “dust-on-film” case in Fig. 4.8a. Our plasmonic smart dust can therefore sensitively distinguish subtle changes at its probing site, yielding large associated optical changes.

This shows that our method can easily be adapted for a multitude of different surface morphologies and associated local chemical reactions. In addition, the low statistical error of the centroid wavelength position (standard deviation $\sigma = 0.13$ nm) together with a spectral shift of 1.5 nm at 0.5 vol.% hydrogen holds great promise for sensitively detecting low amounts of hydrogen in the ppm range.

To theoretically support our experimental observations, the scattering spectra of a plasmonic smart dust particle upon hydrogen uptake are calculated for the “dust-on-film” and “film-on-dust” platforms, respectively. The calculations were performed

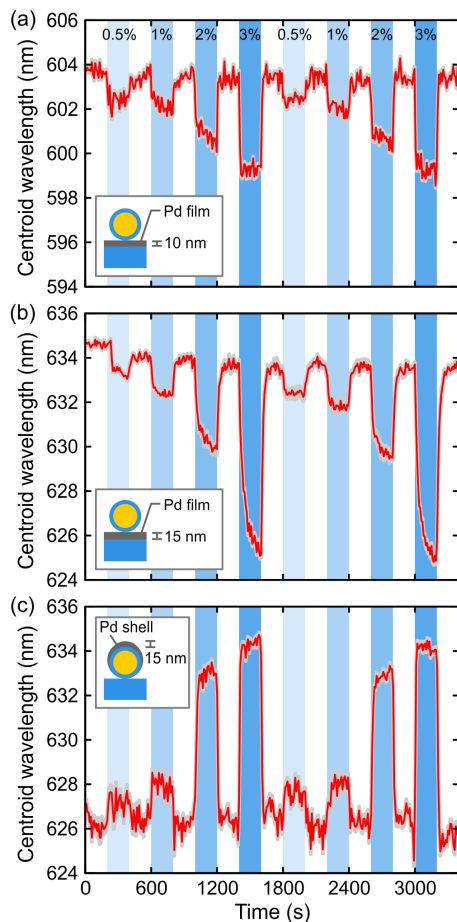


Figure 4.9: Experimental time-resolved centroid wavelengths in response to hydrogen uptake and release. (a) “dust-on-film”, single smart dust particle on a 10 nm Pd film. (b) “dust-on-film”, single smart dust particle on a 15 nm Pd film (same particle as in Fig. 4.8a). The minute 5 nm film thickness change can easily be resolved optically under the same reaction conditions. (c) “film-on-dust”, single smart dust particle covered by a 15 nm Pd film (same particle as in Fig. 4.8b). The spectral response shifts completely to the opposite direction compared to that in the “dust-on-film” platform. This underlines the suitability of our technique for studying local reactions on various surface morphologies. Gray areas behind the red curves denote the errors of the centroid analysis, estimated using a bootstrapping method. The statistical error (standard deviation) of the calculated centroid wavelengths is below $\sigma = 0.13$ nm in all cases.

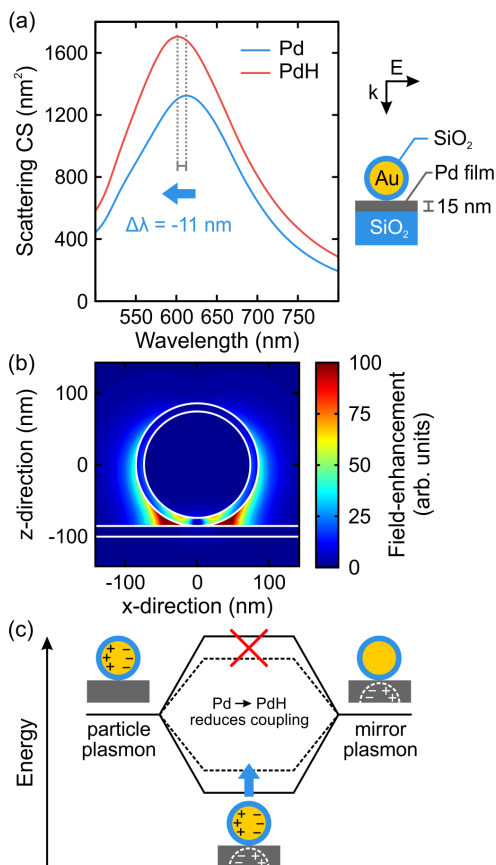


Figure 4.10: Numerical simulations for the “dust-on-film” platform. (a) Simulated scattering spectra for a single smart dust particle on an infinitely extended 15 nm Pd film before and after hydrogen uptake. A fully hydridized state PdH is used in the calculation to establish the maximum spectral shift in the reaction. A maximum blue-shift of $\Delta\lambda = 11$ nm together with a resonance intensity increase is predicted. (b) Electric near-field distribution at resonance. The intense near-fields are strongly localized at the touching point between the smart dust and the Pd film. (c) Hybridization model for interpreting the observed spectral blue-shift. The localized plasmon of the Au nanoparticle hybridizes with the induced mirror plasmon in the Pd film, leading to the observed bonding mode. The higher energy anti-bonding mode is not allowed in this configuration. When changing from Pd to PdH, the properties of the film become less metallic. This leads to weaker plasmonic coupling and therefore a reduced energy splitting, resulting in a resonance blue-shift.

using a commercial implementation of the method of moments (MoM) based on the surface equivalence principle (FEKO 6.2, EM Software & Systems-S.A.).

The infinite multilayered substrate was taken into account using the planar Green's function formalism. The linearly polarized incident plane wave propagates perpendicular to the sample surface and arrives from top. The integrated differential cross-section σ_s is defined as the scattered power into the solid angle $\Omega(\theta, \varphi)$ with $\theta = [170, 180]$ and $\varphi = [0, 360]$ normalized to the incident power flux. Optical constants for Pd and Au are taken from literature.^{127,132} The numerical results for the "dust-on-film" configuration are shown in Fig. 4.10a.

In the case of a 15 nm Pd film, a clear spectral blue-shift of $\Delta\lambda = 11$ nm together with an increase of the resonance intensity is predicted when changing the dielectric function of the film from pure Pd to fully hydrided Pd, i.e., PdH.¹²⁷ In the experiment, the blue-shift is around 8 nm at a hydrogen concentration of 3 vol.%, which is still below the fully hydrided state. Thus, the numerical calculations neatly confirm the trend of the spectral changes in response to hydrogen uptake in the experiment.

The highly localized nature of our plasmonic nanoprobe becomes evident from the simulated electric near-field distribution at resonance (Fig. 4.10b). Intense near-fields are strongly concentrated around the touching point of the smart dust particle with the Pd film, allowing for the interrogation of local reactions with high spatial resolution. When linearly polarized light impinges on a smart dust nanoparticle, it excites an oscillating particle plasmon in the Au core. This charge distribution induces the oscillation of a mirror plasmon in the underlying Pd film. The particle and mirror plasmons mix and hybridize, resulting in a lower-energy bonding mode and a higher-energy anti-bonding mode (Fig. 4.10c). The latter cannot be observed due to the parity of the mirrored charge distribution.¹⁴⁸

When transitioning from Pd to PdH upon hydrogen uptake, the real part of the Pd film's dielectric function becomes less negative,¹²⁷ giving rise to a less metallic character of the film and thus weaker coupling between the particle and mirror plasmons. This leads to reduced plasmonic mode-splitting and the bond-

ing mode shifts to a higher energy or, when considering wavelengths, to the blue. The reduction in metallic character during the Pd/PdH transition also explains the increase in the scattering amplitude due to increased light transmission through the film.

Numerical results for the “film-on-dust” platform are shown in Fig. 4.11a. We again compare the scattering spectra for the Pd and PdH cases. In contrast to the “dust-on-film” platform, a resonance red-shift of $\Delta\lambda = 10$ nm upon hydrogen uptake is predicted and the resonance intensity increases only slightly due to the lack of a fully closed Pd film, which is in excellent agreement with the observations in our experiment.

The electric near-field distribution at resonance is again calculated for this configuration (Fig. 4.11b). Unlike the “dust-on-film” platform where a clear focusing of the near-fields at the base of the nanoparticle is observed, the intense fields are localized more at the side surfaces of the smart dust particle, indicating strong interaction between the gold core and the curved Pd shell. For simplicity, we utilize a continuous Pd shell around the dust particle in our hybridization model (Fig. 4.11c).

Here, the particle plasmon of the smart dust particle hybridizes with the particle plasmon excited in the Pd shell, leading to a lower-energy bonding and a higher-energy anti-bonding mode. Due to the large intrinsic damping in gold at short wavelengths, the anti-bonding mode is not clearly observable in the wavelength range of interest. When changing the dielectric function of the shell from Pd to PdH, the shell plasmon shifts to a lower energy, leading to a red-shift of the bonding mode, which agrees well with the spectral shift trend in the experiment.

The presented single-particle platform enables simultaneous probing of chemical reactions at various surface morphologies and local reaction environments under identical reaction conditions. By combining two-dimensional imaging and spectroscopic techniques, synchronized mapping and chemical sensing on a subdiffraction-limit scale could be achieved.¹⁴⁹ Our method can be extended to investigate a plethora of chemical reactions on surfaces, ranging from the reduction and oxidation steps in fuel cells.^{150,151} to catalytic water splitting.¹⁵²

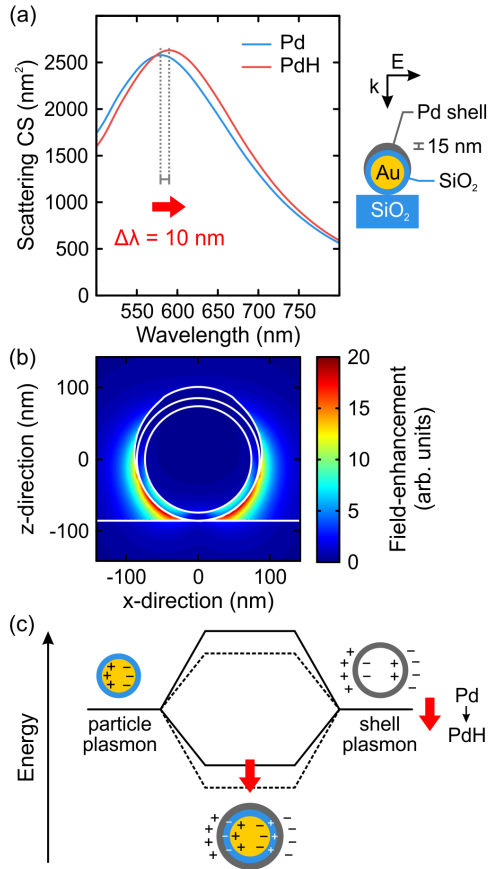


Figure 4.11: Numerical simulations for the “film-on-dust” platform. (a) Simulated scattering spectra for a single smart dust particle coated with a 15 nm Pd film. When changing the dielectric function of the shell from Pd to PdH, a red-shift of $\Delta\lambda = 10$ nm is predicted. The resonance intensity increase is not as large as that in Fig. 4.10a. (b) Electric near-field distribution at resonance. The electric near-fields are more localized at the side surfaces of the smart dust, indicating resonant coupling of the particle plasmons in the Au and Pd parts of the structure. (c) Hybridization model for interpreting the observed spectral red-shift. For clarity, a continuous Pd shell is utilized. The particle plasmon in the Au core hybridizes with the particle plasmon in the Pd shell, resulting in a lower-energy bonding mode and a higher-energy anti-bonding mode. When changing from Pd to PdH, the Pd shell plasmon shifts to a lower energy level, leading to a corresponding red-shift of the bonding mode.

4.3 DNA-ASSEMBLED BIMETALLIC PLASMONIC NANOSENSORS

Plasmonic hybrid nanomaterials are highly desirable in advanced sensing applications. Different components in these materials undertake distinct roles and work collectively. One material component may act as an efficient light concentrator and optical probe, whereas another provides specific chemical or biological functionality.

This section presents chemically synthesized DNA-assembled bimetallic plasmonic nanostructures and demonstrates their application for the all-optical detection of hydrogen.* Specifically, gold (Au) nanorods are functionalized with DNA strands, which serve both as linkers and seeding sites for the growth of palladium (Pd) nanocrystals and facilitate reliable positioning of Pd satellites around a Au nanorod at an ultrashort spacing in the nanometer range.

By monitoring dark-field scattering spectra of single Au-DNA-Pd nanorods during controlled cycles of hydrogen gas exposure, an unambiguous concentration-dependent optical response was observed. With this, our method enables, for the first time, the all-optical detection of hydrogen-induced phase-change processes in sub-5 nm Pd nanocrystals at the single antenna level. By substituting the Pd satellites with other functional materials, our sensor platform can be extended to detect a multitude of chemical and biological reagents, both in liquid and gaseous phases.

In recent years, plasmonics has led to tremendous progress in optical sensors on the single-particle level. Recently, advanced wet chemical methods have enabled the controlled synthesis of metal nanoparticles with various shapes, sizes, and configurations.^{153–156} Such metal nanoparticles possess remarkable material quality and are highly viable for industrial mass production.

In particular, metal nanoparticles composed of materials such as gold (Au) and silver (Ag) exhibit excellent plasmonic properties and have been widely applied for sensing low-level and label-free analytes in complex media due to their simple and

* This section is adapted from N. Li, A. Tittel et al., *DNA-assembled bimetallic plasmonic nanosensors*, *Light: Science & Applications* 3, e226 (2014). Reprinted with permission. Original article under creative commons attribution-noncommercial-sharealike 3.0 unported license

cost-effective sensing strategy.^{8,9,122} Traditionally, a sensing experiment is performed by tracking the resonance shift of a plasmonic nanoparticle in the presence of analytes, which alter its local environment. By combining multiple materials, biological or chemical functionality can be added to such well-established but mostly inert noble metal nanoparticle systems.

Building on the rapid progress in the field of novel nanomaterials, various metal nanoparticles with hybrid components have been developed. For example, Au-Ag core-shell nanoparticles were used to successfully map the sulfide content in live cells through irreversible Ag_2S formation.¹⁵⁷ Further applications of core-shell particles include the investigation of hydrogen catalytic processes in Au-Pd particles as well as the sensitive detection of carbon monoxide using a Cu-CuO geometry.^{83,91}

In the context of complex synthetic nanomachines, Al-Ga Janus nanoparticles were utilized for the creation of water-driven micromotors.¹⁵⁸ Additionally, approaches such as on-wire lithography¹⁵⁹ were used for the reliable fabrication of Au-Ni-Pt gap structures with nanometer precision.

Thus far, most hybrid metal nanomaterials have been based on direct contact between different material components, which can be detrimental when applied in plasmonic sensing because components with poor plasmonic properties can lead to increased damping in the hybrid system, yielding low sensitivity. To overcome this issue, DNA-based nanotechnology has been utilized for the fabrication of various metal nanoclusters and hybrid metal nanostructures.^{160–165}

Here, we utilize chemical synthesis to fabricate DNA-assembled bimetallic plasmonic nanoparticles, in which DNA serves as both the construction material and a natural spacer between the two metal components (Fig. 4.12a). Furthermore, we demonstrate that such bimetallic nanoparticles can be used for the all-optical plasmonic detection of hydrogen in real time.

In our system, the Pd nanocrystals act as a functional medium, which can absorb and release hydrogen. Previous experimental studies using single nanodevices have focused on catalytic reactions on extended Pd films⁹³ or in Pd nanodisks with diameters down to 30 nm.^{34,35} By contrast, our nanosensor devices achieve,

for the first time, the all-optical detection of hydrogen-induced phase changes in extremely small (sub-5 nm) Pd nanocrystals on the single-antenna level.

The catalytic reaction under investigation involves the chemisorption of hydrogen on the Pd surface, its near barrierless dissociation, and diffusion of atomic hydrogen into Pd to form palladium hydride.^{32,121} The Au nanorod concentrates strong electromagnetic fields near its surface, where the chemical reactions occur. Simultaneously, the Au nanorod acts as an optical probe that transforms the localized information of hydrogen absorption and desorption in Pd to the far field.

The preparation of our nano-optical sensor particles began with the synthesis of Au seeds, following a silver-assisted seed-growth or binary surfactant-assisted seed-growth procedure, depending on the sizes of the Au nanorods.^{153,156} DNA-assisted assembly and growth of the Pd satellite nanocrystals then proceeded, as illustrated in Fig. 4.12b.

First, the S-S bond in thiolated DNA was reduced by adding 10 μL of 100 mM tris (2-carboxyethyl) phosphine (TCEP) to 50 μL of 100 μM DNA solution, and the sample solution was incubated for 4 hours. Excessive TCEP was removed using a spin column. Subsequently, purified thiolated DNA sDNA-SH and its complementary strand com-sDNA-SH were obtained.

Freshly synthesized Au nanorods with the desired dimensions were then added to the purified sDNA-SH in a buffer solution. The molar ratio of sDNA-SH to Au nanorods was more than 2000:1. After 12 hours, the mixture was centrifuged, the supernatant was discarded, and the Au-sDNA-SH nanorods were suspended in a 1X Tris/Borate/EDTA (TBE) buffer containing 100 mM NaCl.

The buffered Au-sDNA-SH nanorods were then incubated with the complementary com-sDNA-SH and were annealed in PCR in a thermocycler from 45 $^{\circ}\text{C}$ to 25 $^{\circ}\text{C}$ over 12 hours. The mixture was then centrifuged twice, the supernatant was discarded, and the pellet was suspended in ultrapure water. The concentration of these Au-DNA conjugates was estimated using UV-Vis spectroscopy.

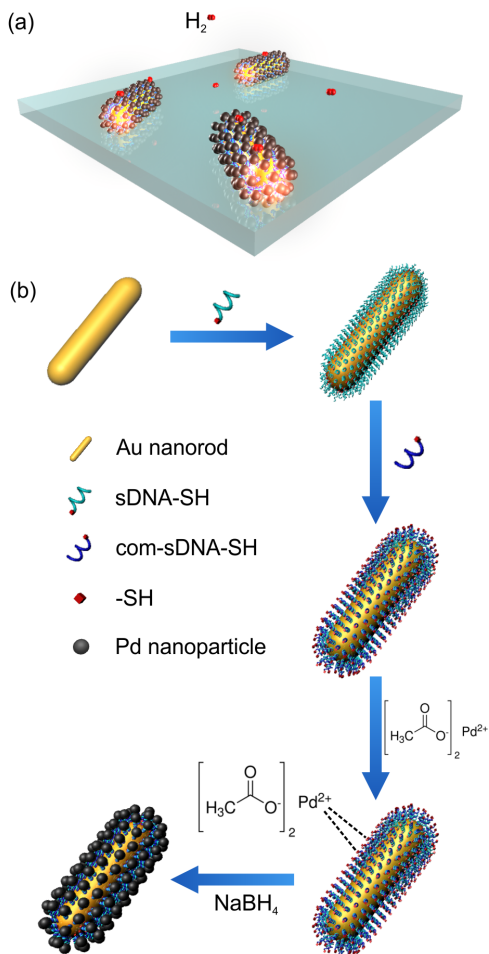


Figure 4.12: (a) Schematic of the DNA-assembled bimetallic nanosensor, which is composed of palladium (Pd) nanoparticles that are connected to a gold (Au) nanorod via DNA linkers. (b) Synthesis details for the self-assembled device.

The Au-DNA nanorods were then mixed with 20 μL of a freshly prepared 2.5 mM $\text{Pd}(\text{CH}_3\text{COO})_2$ solution and 20 μL of 1% polyvinylpyrrolidone (PVP). The mixture was stirred for 4 hours at room temperature and subsequently centrifuged three times at 5000 rpm for 5 minutes. Again, the supernatant was discarded and the pellet was suspended in ultrapure water. Finally, the mixture was reduced by 10 μL of 5 mM freshly prepared ice-cold NaBH_4 to obtain the Au-DNA-Pd hybrid nanoparticles.

To first assess the quality of our Au-DNA-Pd nanoparticles, transmission electron microscopy (TEM), scanning TEM (STEM), and elemental mapping using a FEI Tecnai F20 electron microscopy system were performed. The samples for TEM imaging were prepared by drop-casting 10 μL of the sample solution on a carbon-coated TEM grid.

Figure 4.13 presents the TEM images of the Au-DNA-Pd nanoparticles with different dimensions, demonstrating the high structural homogeneity of our synthesis method. The three batches of Au-DNA-Pd nanoparticles (labeled 1 to 3) have dimensions (length \times width) of 36 nm \times 12 nm, 46 nm \times 12 nm, and 98 nm \times 43 nm. The Pd nanocrystals are approximately 3-5 nm in diameter, as evident from high-resolution bright-field TEM measurements (Fig. 4.14a). In all cases, the individual satellite Pd nanocrystals are clearly visible at high magnifications.

Successful assembly of the different metal components was demonstrated using STEM imaging and elemental mapping of the Au-DNA-Pd nanoparticles from batch 1 (Fig. 4.14a). By filtering the STEM image with respect to the electron energy in the scanning beam, the elemental contributions of Au and Pd to the total signal could be quantified (Figs. 4.14b,c). A composite of the color-coded results for Au and Pd is presented in Fig. 4.14d, which clearly illustrates that small Pd satellite nanocrystals form a dispersive layer around the center Au nanorod. This finding proves the viability of our synthesis method for the precise and reliable creation of complex hybrid nanostructures.

To investigate the optical properties of our Au-DNA-Pd nanoparticles, UV-VIS spectra of the three nanorod batches, before and after the Pd growth, were measured (Fig. 4.15). For all three batches, the pronounced plasmonic absorbance peak red-shifts

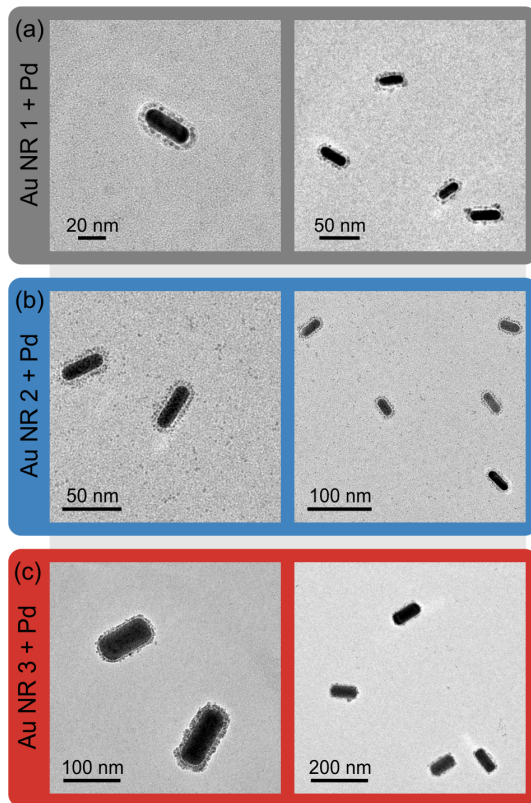


Figure 4.13: Transmission electron microscopy (TEM) images of the three batches of DNA-assembled nanosensors with different design dimensions.

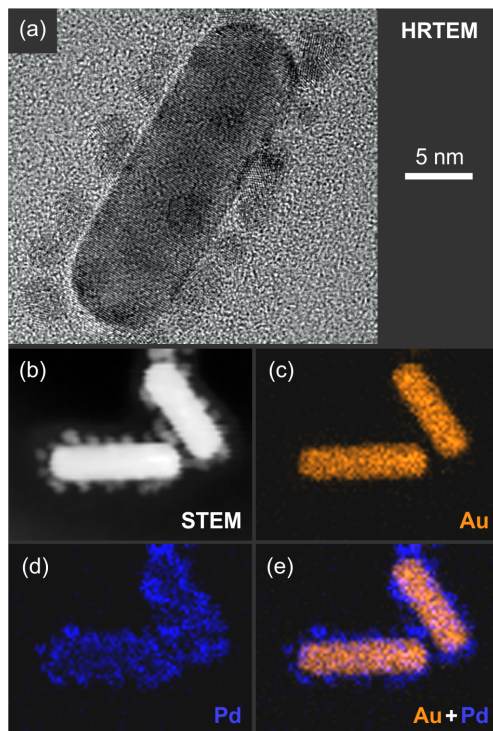


Figure 4.14: (a) High-resolution transmission electron microscopy (HRTEM) image of a Au-DNA-Pd nanorod from batch 1. The sub-5nm satellite Pd nanocrystals are clearly visible. (b) Scanning TEM image of two nanorods from batch 1. (c-e) Element-resolved (energy filtered) STEM images of the same nanorods.

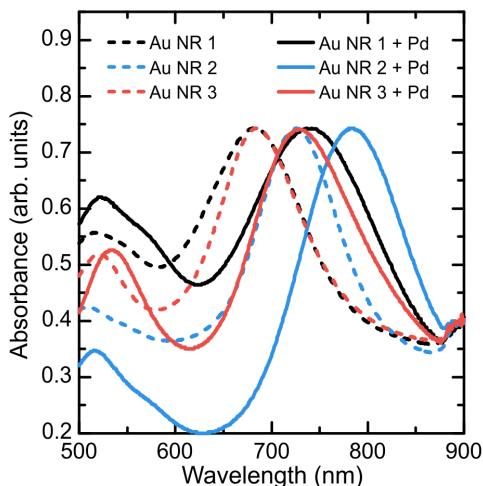


Figure 4.15: Ensemble absorbance spectra for three batches of Au nanorods of different design lengths, with and without DNA-assembled Pd nanocrystals (solid and dashed curves).

by approximately 50 nm after the growth of the Pd nanocrystals. The hybrid plasmonic nanoparticles clearly exhibit excellent wavelength tunability by controlling the the length and structural aspect ratio.

To move from the sensing behavior of a nanoparticle ensemble towards progressively smaller detection volumes, we utilize single-particle dark-field spectroscopy. In hydrogen-sensing experiments, we recorded the scattered light from single Au-DNA-Pd nanoparticles while cycling the gas concentration in a gas cell between pure nitrogen and different hydrogen concentrations in nitrogen carrier gas.

Time-resolved dark-field scattering spectra were recorded using a Nikon TE2000UE inverted microscope combined with a Roper Scientific SP-2500i spectrograph and a Peltier-cooled PIXIS 256E CCD-camera. Spectra were taken in transmission and using unpolarized incident light. The samples were placed into a home-built titanium sensor chamber connected to a mass-flow system that allowed for the precise control of the hydrogen concentra-

tion in the chamber. All experimental spectra presented here were taken with an integration time of 8 s, with one spectrum recorded every 10 s.

Figure 4.16a presents the scattering spectrum of a single plasmonic nanosensor particle P1 from batch 3 (length 98 nm \times 43 nm), which exhibits a pronounced peak centered at approximately 700 nm. Compared with the ensemble measurements in aqueous solution, the single particle resonance is slightly blue-shifted on the glass substrate.

To reliably track the resonance wavelength of the nanosensor over time, we employed a centroid detection method.^{93,145} This analysis technique computes the first moment, or center of mass, of the scattering spectrum, considering all the data points in a certain wavelength span. This procedure allows us to track small spectral shifts with high signal-to-noise ratios.

The resonance peak of nanosensor particle P1 undergoes a fast and reversible red-shift when exposed to hydrogen concentrations of 10, 20, and 30 vol.% H₂ in N₂ carrier gas, with response times on the order of seconds. Additionally, we observed a clear concentration dependent response, with spectral shifts ranging from 0.2 to 0.4 nm (Fig. 4.16b). When examining a second nanosensor particle on the same substrate, we again observed a clear concentration dependence optical response (Fig. 4.16c).

Although the magnitude of the spectral shifts is different, the qualitative behavior is similar. This difference in magnitude is due to small changes in local material distribution and can be further reduced by optimizing the synthesis process. Most importantly, we were able to, for the first time, detect the hydrogen-induced phase-change processes in extremely small Pd particles on the order of 3-5 nm at the single-antenna level.

In conclusion, we demonstrated a novel nano-optical single particle hydrogen sensor utilizing wet-chemical synthesis of Au nanorods with adjacent, DNA-assembled Pd nanocrystals. Our approach results in hybrid plasmonic nanoparticles with tunable particle dimensions and ultra-short Au-Pd distances on the order of several nanometers. The precise positioning of the Pd satellite nanospheres with respect to the Au nanorods was verified using energy-filtered scanning TEM measurements.

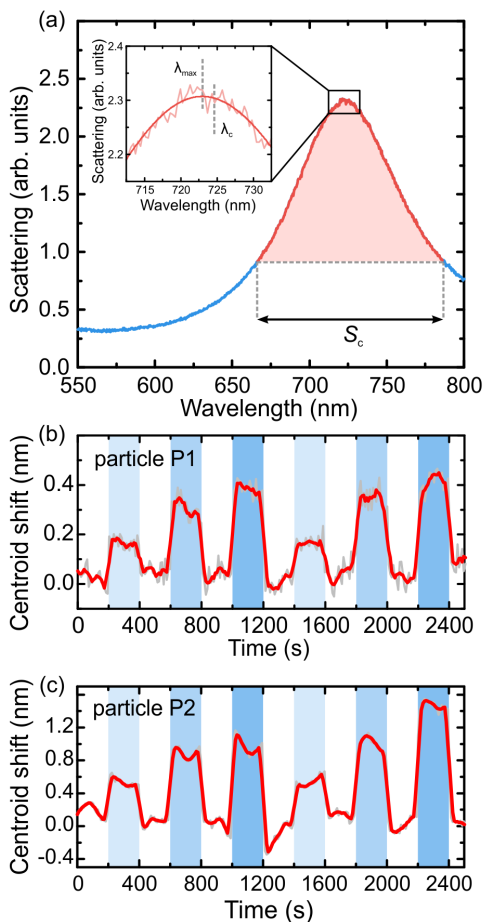


Figure 4.16: (a) Dark-field scattering spectrum of a single Au-DNA-Pd nanorod on a glass substrate. S_c indicates the wavelength span included in our centroid calculation. Comparison of the wavelength of the scattering maximum λ_{\max} and the centroid wavelength λ_c (inset). (b) Time-resolved sensing performance of the DNA-assembled nanosensor particle P1 when exposed to cycles of 10, 20, and 30 vol.% H_2 in N_2 and N_2 carrier gas. (c) Similar measurements on a second sensor particle P2 on the same substrate. The gray line represents the centroid wavelength from scattering spectra taken every 10 s with an integration time of 8 s. The red line is a running average over 5 data points.

As a next step, the number of Pd nanocrystals linked to each Au nanorod could be controlled by the amount and ratio of thiolated DNA and complementary strands. Additionally, we demonstrated that our Au-DNA-Pd nanoparticles exhibit an unambiguous concentration-dependent optical response to hydrogen exposure at the single particle level. Using appropriate satellite nanoparticle components, one could prepare hybrid plasmonic nanosensor devices with different functionalizations, enabling the reliable detection of a multitude of other gases for practical applications.

In the future, plasmon-assisted detection of transformations in nanoparticles of such small sizes will open the door toward investigations of size-dependent phase transitions on nanoscales below 10 nm.

PERFECT ABSORBERS FOR SENSING AND ACTIVE PLASMONICS

5.1 PALLADIUM-BASED PERFECT ABSORBER SENSOR

As introduced in section 2.3, sub-wavelength metallic nanostructures exhibit unique optical properties, which are dominated by localized surface plasmon resonances.¹³ Their resonance wavelength strongly depends on the shape, size, and material properties of the nanoparticles as well as on the dielectric function of the surrounding medium, enabling a multitude of applications in chemical and biological sensing.⁹

In recent years, plasmonic structures with large (or “perfect”) absorption in a certain wavelength range have attracted considerable interest. So far near perfect absorption has been realized experimentally in the GHz/THz range^{21,22} as well as in the near infrared.^{14,166} A design in the visible based on a sub wavelength hole array has so far only been studied theoretically.¹⁶⁷

This section presents the experimental realization of a palladium-based plasmonic perfect absorber at visible wavelengths and its application to hydrogen sensing.* The proposed design exhibits a reflectance $< 0.5\%$ and zero transmittance at 650 nm and the operation wavelength of the absorber can be tuned by varying its structural parameters. Exposure to hydrogen gas causes a rapid and reversible increase in reflectance on a timescale of seconds. This pronounced response introduces a novel optical hydrogen detection scheme with very high values of the relative intensity response.

We chose palladium because of the strong change of its optical properties upon hydrogen absorption. Due to hydrogen incorporation palladium undergoes a phase transition from a metal to

* This section is adapted from A. Tittl et al., *Palladium-Based Plasmonic Perfect Absorber in the Visible Wavelength Range and Its Application to Hydrogen Sensing*, *Nano Letters* **11**, 4366-4369 (2011). Reprinted with permission. Copyright 2011 American Chemical Society.

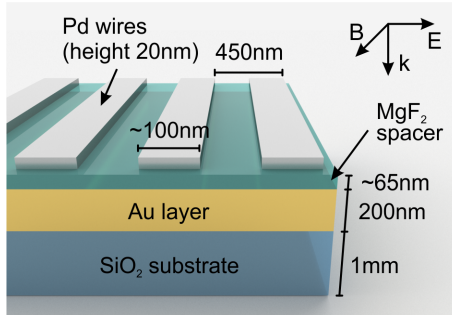


Figure 5.1: Sketch of the perfect absorber hydrogen sensor. Palladium nanowires are stacked above a gold mirror. The layers are separated by a MgF_2 spacer.

a metal hydride which leads to an expansion of the palladium lattice.¹⁶⁸ Additionally, the incorporation leads to a shift of the Fermi level of the conduction electrons³⁰ and therefore significantly changes the real and imaginary part of the dielectric function of palladium.

Optical detection is of particular interest since hydrogen forms an explosive atmosphere when it mixes with air at volume concentrations ranging from 4 vol.% to 76 vol.%. All-optical sensors minimize the risk of explosion and therefore are highly desirable for industrial and automotive applications.

Early optical hydrogen sensing schemes were based on the measurement of optical change in thin palladium films due to hydrogen incorporation.¹⁶⁹ Recently, several new types of hydrogen sensors based on nanoplasmonic effects have been proposed.^{33,34,111} In contrast to traditional plasmonic refractive index sensors, novel plasmonic sensing concepts utilize a hydrogen-induced frequency shift of the plasmon oscillations excited in palladium nanostructures.

In our perfect absorber structure we utilize the plasmonic response of palladium nanowires stacked above a 200 nm thick gold film. The two layers are separated by a 65 nm dielectric MgF_2 spacer layer as depicted in Fig. 5.1.

When light polarized perpendicular to the wires impinges on our structure, localized plasmon oscillations are excited in the palladium wires. The resulting charge distribution leads to the

antiphase oscillation of a mirror plasmon in the thick gold film below, giving rise to a circular current distribution and consequently a magnetic response of our structure.¹⁴ This leads to efficient coupling of the incident light into the structure where it is dissipated as heat in both the metallic components and the dielectric spacer layer.

In a simple model, the structure can be described as an effective medium with complex electric permittivity $\epsilon(\lambda)$ and magnetic permeability $\mu(\lambda)$. By carefully choosing the geometric parameters of the structure, both ϵ and μ can be adjusted such that its complex impedance $Z_{\text{struc}} = \sqrt{\mu/\epsilon}$ is matched to the vacuum impedance $Z_{\text{vac}} = 1$ (in cgs units) for a given wavelength λ_0 , resulting in zero reflectance. For more details on the working principle of plasmonic perfect absorbers see section 2.5.

In order to examine the optical properties of our structure we perform numerical calculations based on a scattering matrix approach.¹⁷⁰ The dielectric functions ϵ of palladium and gold are taken from tabulated data reported in literature.^{127,132} For the MgF₂ spacer layer $\epsilon = 1.97$ is assumed.

To obtain a cohesive picture of our design's absorptive characteristics, we compute reflectance spectra for a multitude of parameter combinations of the crucial geometric parameters wire width and spacer height. Wire height and periodicity are fixed at 20 and 450 nm, respectively. We then extract the lowest reflectance value as well as its spectral location from the resulting data. Figure 5.2a shows a color-coded plot of the lowest reflectance for every point of the parameter space. A region of minimal reflectance can be seen for wire widths around 100 nm and spacer heights around 60 nm.

Absorption remains $> 99\%$ for a fixed spacer height in this parameter range whereas the spectral location of the reflectance dip can be tuned from 630 to 820 nm by changing the wire width from 90 to 130 nm as shown in 5.2b. The minimum reflectance diagram also identifies regions that are not very sensitive to spacer height variations, which aids reliable fabrication.

The perfect absorber can be utilized as a sensor since hydrogen-induced changes of ϵ in the palladium wires result in an in-

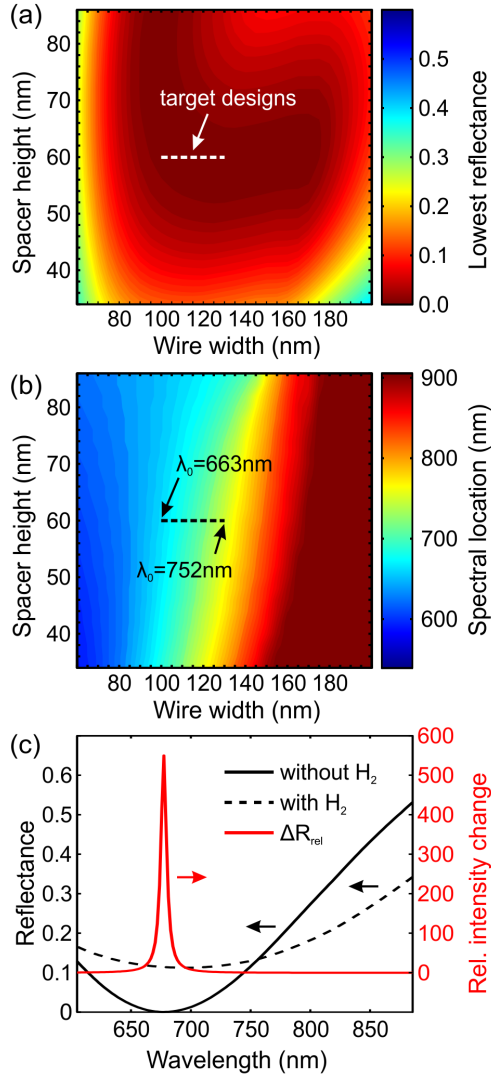


Figure 5.2: (a) Simulated lowest reflectance for different values of the structure parameters wire width and spacer height. A large number of value pairs suitable for utilization in a perfect absorber geometry can be identified next to the dashed line. (b) Simulated spectral location of the reflectance minimum. The spectral location of the perfect absorption can easily be controlled by varying the wire width. (c) Simulated response of the sensor structure to hydrogen exposure. High values of $\Delta R_{\text{rel}} = (R_{\text{H}_2} - R_0)/R_0$ can be achieved close to the spectral location of perfect absorption.

creased impedance mismatch and consequently in a reduction of the perfect absorption.

To investigate the response of one of the target structures to hydrogen exposure, we calculate reflectance spectra for palladium wires with a hydrogen content of 0% and 82%, which constitutes full hydrogenation.¹²⁷ The results together with the relative intensity change $\Delta R_{\text{rel}} = (R_{\text{H}_2} - R_0)/R_0$ are shown in Fig. 5.2c. Since the reflectivity at λ_0 is $R \approx 0$, very high ΔR_{rel} values of more than 500 can be achieved. This shows that our plasmonic structure offers a very large potential for hydrogen sensing.

It is important to note that our structure does not offer a completely angle-independent optical response. The reasons are the periodicity of 450 nm and the associated Rayleigh anomaly. However, since our sensor is designed to operate only at normal incidence, angle-independence is not required in our case.

We fabricated the samples under investigation in a multi-step process at cleanroom conditions. Starting from a clean substrate (Heraeus Infrasil) we subsequently deposited films of 200 nm gold and 65 nm MgF_2 at a pressure of 10^{-6} mbar using thermal evaporation. The spacer layer thickness of 65 nm was chosen to compensate for the material's granularity.

Palladium gratings with different widths of the wires at a fixed grating period of 450 nm were fabricated using a standard electron-beam lithography lift-off technique. The structure area size of the single fields is $300 \mu\text{m} \times 300 \mu\text{m}$. After evaporation of 20 nm palladium the lift-off procedure was performed in the solvent NMP. Scanning electron micrographs were taken to determine the period and width of the wires. In principle, these structures might also be fabricated over areas as large as square decimeters using interference lithography.¹⁷¹

In order to optically characterize our perfect absorber we measure the reflectance of the sample in the visible wavelength range. Collimated and linearly polarized white light from an arc source is focused to the single arrays using a microscope objective with numerical aperture $\text{NA} = 0.3$. Light reflected from the sample is separated from the incident light via a 50/50 beamsplitter cube and detected as a function of wavelength using a commercial spectrometer (Roper Scientific SP 2500i) with an attached Peltier-

cooled PIXIS 256E CCD camera. As a reference we use the reflectance of a plain gold mirror.

Figure 5.3a shows a minimal reflectance of 0.5% at $\lambda_0 = 650$ nm and thus near-perfect absorption for a wire width of 100 nm. This is in excellent agreement with the simulated behavior of the structure. The same sample is used for measuring time-resolved reflectance spectra in the presence of 0.5 to 4.0 vol.% H_2 in N_2 carrier gas (Fig. 5.3a).

For the 4.0 vol.% H_2 concentration, which represents the explosion threshold, we detect a maximum spectral shift of 19 nm and an increase of the reflectance at λ_0 from 0.5% to 4.9%. Due to the low values of the reflectance at resonance we obtain a large relative change of reflectivity $\Delta R_{\text{rel}} = (R_{H_2} - R_0) / R_0$ of 8.8. Compared to conventional thin film palladium hydrogen sensors¹¹² we can increase ΔR_{rel} by one order of magnitude.

To further characterize the sensor we measure the temporal response at a fixed wavelength of $\lambda_0 = 650$ nm during three sensor cycles where the hydrogen concentration was repeatedly changed from 0 to 4 vol.% as depicted in Fig. 5.3b. We are able to detect hydrogen concentrations down to 0.5 vol.% reliably and reproducibly.

To demonstrate the spectral tunability of the reflectance dip we examine samples with different widths of the palladium wires at a constant spacer height of 65 nm. For all samples we observe a reflectance $R_0 < 5\%$ while increasing the wire width from 90 nm to 130 nm. This results in a red shift of the reflection dip (Fig. 5.3c). Since for a fixed spacer height perfect impedance matching cannot be obtained for different wire widths, the modulation depth of the reflectance has a maximum for $w = 100$ nm and decreases with higher or lower widths. We can also observe an increase of the linewidth of the dip for higher wire widths.

To summarize, we have experimentally demonstrated that near-perfect absorption at visible wavelengths can be obtained using a simple design based on plasmonic palladium nanowires in combination with a dielectric spacer layer and a gold mirror. Our structure shows a reflectance of 0.5% which in combination with a complete suppression of transmission yields an absorbance of $A \approx 99.5\%$. The spectral location of maximum absorbance can

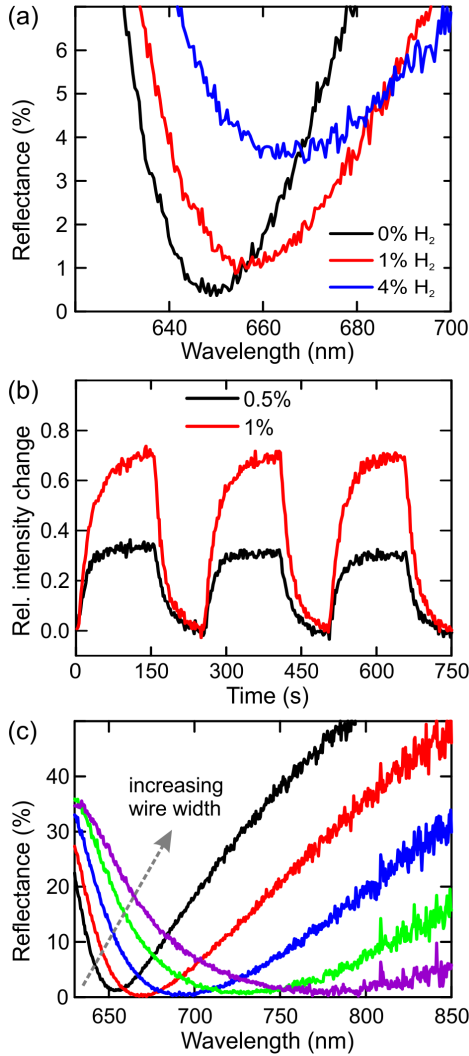


Figure 5.3: (a) Reflectance of the absorber for different hydrogen concentrations. Our sensor exhibits near-perfect absorption at 650 nm and hydrogen incorporation leads to a pronounced change of the reflectance spectrum. (b) The relative change of reflected intensity measured over time at the wavelength of perfect absorption λ_0 . Three cycles of hydrogen exposure for two different concentrations are shown. (c) Reflectance spectra for absorber samples with different wire widths and constant spacer height. The use of palladium is also optically advantageous, since its large losses lead to a rather broadband perfect absorber response.

be tuned over a range of approximately 100 nm by varying the width of the palladium wires.

Furthermore, we utilized our Pd perfect absorber structure for hydrogen sensing and were able to reliably detect concentrations down to 0.5% H₂ in air with response times in the range of seconds. Optimizing sample fabrication and measurements even further, this already pronounced response should enable extremely sensitive optical gas detection schemes down to the ppm range in the future.

5.2 IMPEDANCE MATCHING IN PLASMONIC PERFECT ABSORBERS

As demonstrated in the preceding section, plasmonic perfect absorbers can act as central building blocks for plasmonic sensing geometries, while simultaneously enabling a multitude of other applications ranging from spectroscopy to photovoltaic efficiency enhancement.^{14,24,25} A crucial requirement for such elements is the angle-independence of the absorptive performance.

This section presents the theoretical development and experimental verification of a quantitative model for the angular behavior of plasmonic perfect absorber structures based on an optical impedance matching picture.* To achieve this, we utilize a simple and elegant k-space measurement technique to record quantitative angle-resolved reflectance measurements on various perfect absorber structures. Especially, this method allows quantitative reflectance measurements on samples where only small areas have been nanostructured, for example by electron-beam lithography.

Combining these results with extensive numerical modeling, we find that matching of both the real and imaginary parts of the optical impedance is crucial to obtain perfect absorption over a large angular range. Furthermore, we successfully apply our model to the angular dispersion of perfect absorber geometries with disordered plasmonic elements as a favorable alternative to current array-based designs.

So far, detailed experimental studies on the underlying reason for the angular dispersion of plasmonic perfect absorbers at visible and near-infrared wavelengths are missing. This is associated with the fact that angle-resolved reflectance measurements with quantitative accuracy, especially in the infrared spectral range, are not easily performed, particularly in common FTIR microscopy setups. Samples where only small areas have been nanostructured, for example by electron-beam lithography, pose further challenges.

* This section is adapted from A. Tittl et al., *Quantitative Angle-Resolved Small-Spot Reflectance Measurements on Plasmonic Perfect Absorbers: Impedance Matching and Disorder Effects*, ACS nano **8**, 10885-10892 (2014). Reprinted with permission. Copyright 2014 American Chemical Society.

This problem is overcome by utilizing a k-space measurement approach to record large-angle and polarization dependent reflectance measurements on different perfect absorber geometries. Combining these results with extensive numerical modeling, we develop and verify a quantitative model for the angular behavior of plasmonic absorbers. Especially, we determine the imaginary part of the optical impedance in our plasmonic absorbers to be the key factor for angle-independent performance. One key advantage of our experimental method is the ability to measure the angular response of plasmonic samples with small structured areas, making it ideally suited for the investigation of nanoscale devices fabricated using electron-beam lithography.

To shed light on the angular absorptive performance of our systems, we examine the angle-dependent reflectance from four different perfect absorber designs in p-polarization (Fig. 5.4a,b). The experimental setup is depicted in Fig. 5.4c.

The perfect absorber sample is illuminated (red beam) and the corresponding reflected beam (light red beam) is collected by the objective. The back focal plane (which constitutes the Fourier plane¹⁷²) of the objective is imaged onto the entrance slit of a spectrometer mounted with a Princeton Instruments PIXIS 256E CCD (in the visible spectral range) or OMAV array (in the infrared). Using the spectrometer adds the ability to analyze the spectral response along with the angular response of the system.

The polar angles θ, φ are related to the k-space (Fourier plane) by the following relation:

$$\mathbf{k} = k_x \hat{\mathbf{x}} + k_y \hat{\mathbf{y}} = \frac{2\pi}{\lambda} \sin \theta \cos \varphi \hat{\mathbf{x}} + \frac{2\pi}{\lambda} \sin \theta \sin \varphi \hat{\mathbf{y}} \quad (5.1)$$

The measurement setup is aligned at $\varphi = 0$, with the polarization parallel to the incident plane as shown in Fig. 5.4a, so only the polar angle θ is resolved. In the case of samples in the visible range, the CCD camera resolves the full spectral-angular response of the sample in one single measurement. Generally, the angular range of this measurement is only limited by the numerical aperture of the objective. In the case of samples in the NIR spectral range, the OMAV array records the spectral response

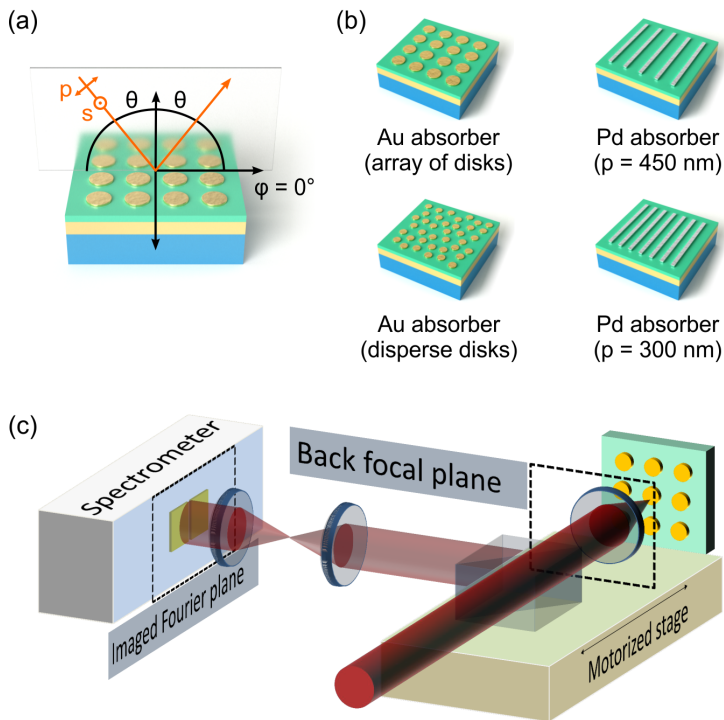


Figure 5.4: System under investigation (a) Schematic of the angle-dependent reflectance measurements discussed in this work. We can study the optical response for incident light parallel and perpendicular to the plane of incidence (p- and s-polarization). (b) Overview of the four investigated plasmonic perfect absorber structures. (c) Schematic drawing of the spectral-angular k-space experimental setup used to obtain quantitative large-angle reflectance measurements from our structures. The back focal plane of the lens, which is the Fourier plane of the illuminated sample, is imaged onto the entry slit of a spectrometer to obtain reflectance spectra for a large range of incident angles simultaneously.

only for a specific angle. Therefore, a motorized stage is used to scan the imaged Fourier plane on the spectrometer slit to resolve the full angular response of the perfect absorber.

This spectral-angular k-space imaging technique is easy to implement and can measure small area plasmonic structures efficiently and with high precision.¹⁷³ In our case, when using samples nanostructured by electron-beam lithography, only an area of $100\ \mu\text{m} \times 100\ \mu\text{m}$ is measured. We note that in most previous works, the optical response of perfect absorbers was commonly shown only for normal incidence, and no full angular characterization was demonstrated experimentally.

Particularly, perfect absorbers are usually measured using a goniometric approach, which requires tilting the detectors, the samples, or both. This approach is very sensitive to alignment errors and since each angle is measured separately, it requires very long measurement times. Also, typical goniometric reflection setups in commercial ellipsometers have minimum beam sizes in the millimeter range, making them unsuitable for measuring small area plasmonic structures. The angular resolution is also limited by the mechanical steps of the goniometric stage. With the spectral-angular k-space imaging technique, we can resolve the spectral-angular response of small-area samples without any alignment errors, with high spectral and angular resolution, and with a very fast measurement.

As a first demonstration of our method, we examine a well-known near-infrared perfect absorber design consisting of an array of gold (Au) nanodisks stacked above a magnesium fluoride (MgF_2) spacer layer and an Au mirror.¹⁴ In the original work, an absorbance of 99% was experimentally demonstrated at normal incidence. However, the angular dispersion was only investigated using numerical simulations.

The full angular dispersion of this perfect absorber design in a wide angular range from -36° to 36° (limited by the numerical aperture of the objective) is shown in Fig. 5.5a for a structure with disk diameter 330 nm, disk height 20 nm, periodicity 600 nm, spacer height 30 nm, and mirror height 200 nm.

We observe a clear reflectance dip at a wavelength of 1480 nm, with a minimum reflectance of around 2% and reflectance values

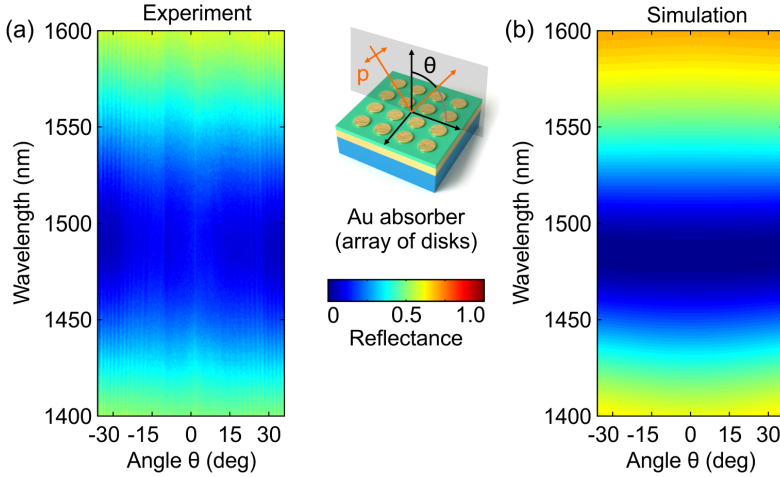


Figure 5.5: (a) Spectral angular reflectance measurements of the near-infrared Au-based perfect absorber. (b) Numerical simulation of the same system. The colorbar represents the reflectance with perfect absorption corresponding to zero reflectance (blue).

below 10% over the whole angular range. Thus, we experimentally verify, for the first time, the near angle-independence of this perfect absorber design.

To support our measurements theoretically, we perform numerical simulations using a scattering-matrix-based Fourier modal method.^{170,174} All structures are defined on a glass substrate ($n = 1.5$). The array-based Au perfect absorber consists of Au nanodisks (diameter 320 nm, periodicity 600 nm, height 20 nm) placed above a MgF₂ spacer layer (thickness 30 nm, $n = 1.38$) and an Au mirror (thickness 200 nm). Optical constants for Au were taken from literature.¹³²

The palladium-based perfect absorber design with large periodicity consists of a Pd wire grating (wire width 125 nm, periodicity 450 nm, wire height 20 nm), placed above a MgF₂ spacer layer (thickness 50 nm) and an Au mirror (thickness 200 nm). Optical constants for Pd are again taken from literature.¹²⁷ The palladium-based perfect absorber with small periodicity consists of a Pd wire grating (wire width 85 nm, periodicity 300 nm, wire height

30 nm), placed above a Al_2O_3 spacer layer (thickness 35 nm, $n = 1.75$) and an Au mirror (thickness 200 nm).

We find an excellent agreement between simulation and experiment, with a pronounced reflectance dip again at a resonance wavelength of 1480 nm (Fig. 5.5b). The angle-independence over the full range is also well reproduced. Still, we find a somewhat broader spectral response of the resonance in the experiment when compared to the simulations. This is most likely due to inhomogeneous broadening as well as additional grain boundaries introduced during the nanostructuring of the Au disks.

The performance and especially the angular dispersion of perfect absorbers can be well understood by considering an optical impedance matching picture. In general, a reflectance of zero in an optical element can be obtained by matching its optical impedance Z to the value of the surrounding space. In perfect absorbers, this impedance can be tuned by varying geometric parameters such as the size of the resonant structure or the thickness of the spacer layer. Since the thick metallic mirror below the structure ensures zero transmittance, perfect impedance matching consequently results in perfect absorption at a certain design wavelength.

The impedance of our structure can be calculated from the scattering parameter results of our numerical simulations using

$$Z = \sqrt{\frac{(1 + S_{11})^2 - S_{21}^2}{(1 - S_{11})^2 - S_{21}^2}} \quad (5.2)$$

where S_{11} and S_{21} denote the scattering matrix coefficients of normal incidence reflection and transmission in p-polarization, respectively. Due to the presence of the thick metallic mirror, S_{21} can safely be set to zero. It is important to note that the impedance $Z = Z' + i \cdot Z''$ is, in general, a complex value.

Figure 5.6 shows the simulation results for the real and imaginary parts of the optical impedance compared to the reflectance for the Au disk array-based perfect absorber. We can clearly observe that both the real and the imaginary parts are perfectly matched to the respective vacuum values of one and zero (in

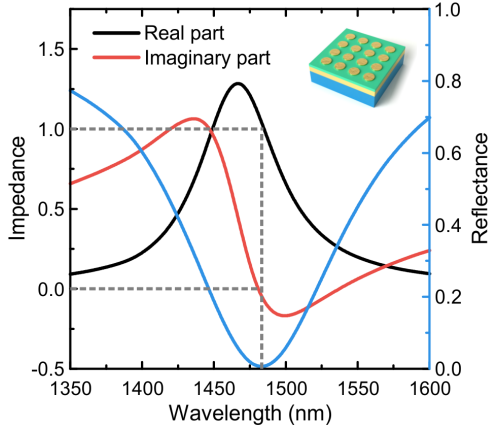


Figure 5.6: Numerical calculation of the reflectance and optical impedance of the Au disk array-based plasmonic perfect absorber from Fig. 5.5 at normal incidence. Both the real and imaginary parts of the optical impedance are perfectly matched to the vacuum values of one and zero, resulting in angle-independent perfect absorption.

cgs units) at resonance, resulting in angle-independent perfect absorption.

In nanostructured plasmonic absorber arrays, the main reason for a lack of angle-independence is a coupling of the absorber resonance to the first diffraction order associated with the grating periodicity of the array. For a given incident angle θ , this Rayleigh anomaly appears at wavelengths given by

$$\lambda_R = p \cdot (n_{\text{env}} + \sin \theta) \quad (5.3)$$

where p is the periodicity of the array and n_{env} is the refractive index of the surrounding medium or the spacer layer, respectively. The presence of the Rayleigh anomaly introduces additional impedance, causing a loss of the perfect impedance matching and thus reduced absorption.^{175–177} Consequently, the design of angle-independent perfect absorber structures requires sufficiently small periodicities to ensure adequate spectral separation between the particle plasmon mode and the Rayleigh anomaly for all required incident angles θ .

In this way, interaction between the grating mode and the perfect absorber resonance can be suppressed, leading to angle-independent absorbance. The spectral separation condition is neatly fulfilled in the Au absorber case. For a periodicity of $p = 450$ nm, and considering the interface of the spacer layer (MgF_2 , $n = 1.38$), the Rayleigh anomaly is found at $\lambda_R = 830$ nm, which is well away from the perfect absorber resonance position at $\lambda_0 = 1480$ nm.

However, the concept of spectral separation between Rayleigh anomaly and perfect absorber resonance does not allow to judge, in a quantitative way, whether a given perfect absorber design is angle-independent or not. In the following, we will show that perfect matching of the imaginary part of the impedance is crucial to obtain fully angle-independent perfect absorption.

To prove the reliability of this model, we will now focus on the more challenging concept of a perfect absorber in the visible wavelength range. To elucidate the influence of the grating mode, we compare two palladium-based (Pd) perfect absorbers with different periodicities. In both cases, the designs consist of Pd wires stacked above a dielectric spacer and an Au mirror that ensures zero transmission.²³

Figure 5.7a shows the spectral angular reflectance measurements of a Pd-based perfect absorber with periodicity 450 nm, wire width 100 nm, wire height 20 nm, MgF_2 spacer height 65 nm, and mirror thickness 200 nm. Even though the absorbance reaches a maximum of 95% at a wavelength of 720 nm at normal incidence, we observe a strong angular dispersion when moving to higher incident angles. Consequently, this design can only be used up to an acceptance angle of $\theta = \pm 14^\circ$ while maintaining an absorbance of $A > 90\%$. This result is again well-supported by our numerical simulations (Fig. 5.7b).

The angular optical response of a Pd-based perfect absorber with a smaller periodicity of 300 nm, wire width 85 nm, wire height 30 nm, Al_2O_3 spacer height 35 nm, and mirror thickness 200 nm is shown in Fig. 5.7c. For this optimized geometry, the angular dispersion is greatly reduced. The small periodicity design again offers very high absorbance of 98% at a wavelength of 690 nm, and maintains absorbance $A > 90\%$ for acceptance

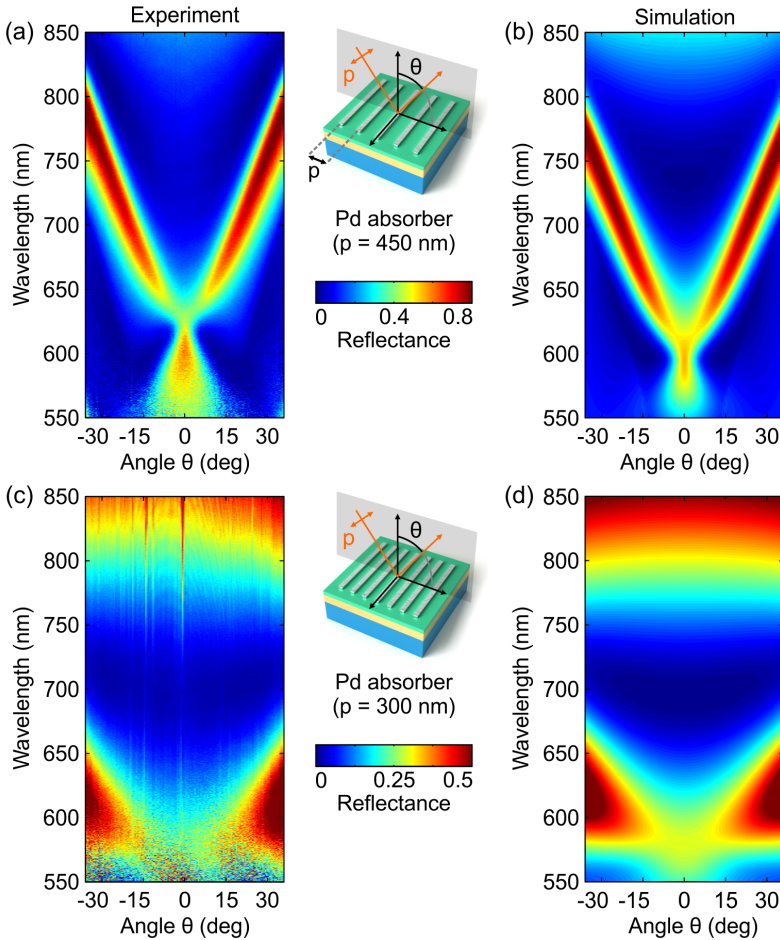


Figure 5.7: (a) Spectral angular reflectance measurements on a Pd-based perfect absorber in the visible wavelength range. The periodicity is $p = 450$ nm. (b) Numerical simulation of the same system. (c) Spectral angular reflectance measurements on a Pd-based perfect absorber in the visible wavelength range. The periodicity is $p = 300$ nm. Note the greatly reduced angle-dependence due to the smaller periodicity. (d) Numerical simulation of the same system.

angles up to $\theta = \pm 36^\circ$. This constitutes an increase of the acceptance angle by close to a factor of 2.5 over the absorber with larger periodicity, which is again in excellent agreement with our simulations (Fig. 5.7d).

The optical impedance matching model now allows quantification of the influence of grating modes on the angular behavior of the perfect absorber resonance. For the large periodicity case ($p = 450$ nm, Fig. 5.8a), only the real part of the optical impedance is perfectly matched to one, which ensures zero reflectance at normal incidence. However, there is pronounced mismatch of $\Delta Z'' = -0.2$ in the imaginary part of the impedance (in cgs units).

This indicates the presence of a grating mode close to the resonance, which causes the strong angular dispersion. The fact that the reflectance at normal incidence is near zero despite the impedance mismatch can be understood by calculating the reflectance as a function of the complex impedance $Z = Z' + i \cdot Z''$. Assuming near-perfect matching of the real part of the impedance ($Z' = 1$) and a small mismatch of the imaginary part ($|Z''| \ll 1$), this yields

$$R = \frac{(Z' - 1)^2 + (Z'')^2}{(Z' + 1)^2 + (Z'')^2} \approx \frac{(Z'')^2}{4} \approx 0. \quad (5.4)$$

Consequently, a small impedance mismatch of the imaginary part has only a negligible influence on the reflectance at normal incidence. When moving to larger angles, however, this mismatch quickly increases, leading to the observed strong angular dispersion.¹⁷⁸

In contrast, for the small periodicity case ($p = 300$ nm), both the real and the imaginary parts of the impedance are perfectly matched to the respective vacuum values of one and zero, resulting in “true” angle-independent perfect absorption (Figure 5b).

To further examine the transition from small to large periodicities, we examine a continuous transition from the $p = 300$ nm to the $p = 450$ nm case. To achieve this, we consider the small periodicity design from Fig. 5.7c, and introduce a gradual increase of the periodicity as the sole parameter variation (Fig. 5.9).

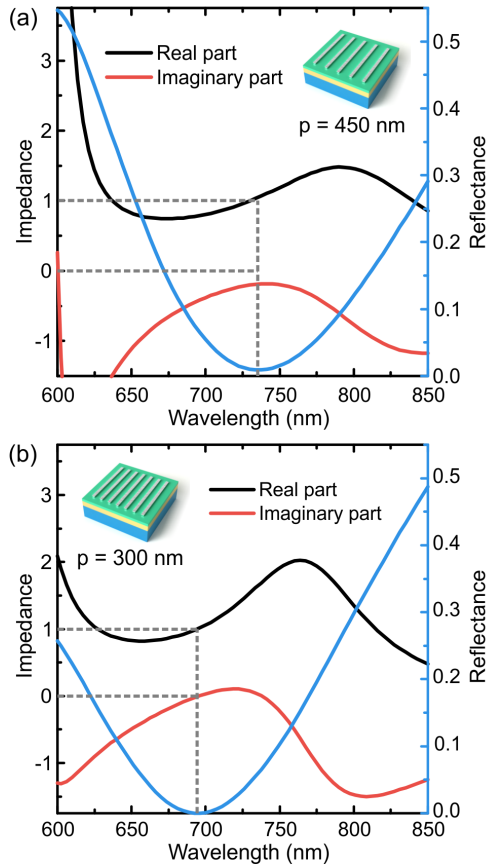


Figure 5.8: Numerical calculation of the reflectance and optical impedance of the two previously discussed Pd-based plasmonic perfect absorbers. (a) For a large periodicity of $p = 450$ nm, only the real part of the impedance is perfectly matched. The mismatch in the imaginary part indicates the presence of propagating modes and thus leads to stronger angle-dependence of the absorption. (b) For a small periodicity of $p = 300$ nm, both the real and imaginary parts of the optical impedance are perfectly matched to the vacuum values, resulting in angle-independent perfect absorption.

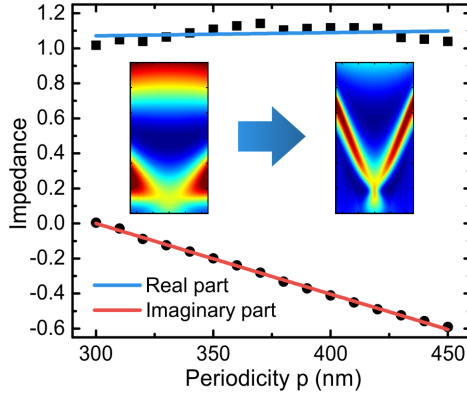


Figure 5.9: Impedance at resonance and at normal incidence of a Pd-based perfect absorber for increasing periodicity. The real part of the impedance remains mostly constant while the imaginary part moves away from the vacuum value of zero for larger periodicities.

The real part of the optical impedance remains close to one for the whole periodicity range while the imaginary part deviates strongly, reaching a maximum impedance mismatch of $\Delta Z'' = -0.6$ for the largest periodicity of 450 nm. Thus, even though the absorbance at normal incidence of this system remains very high ($A > 92\%$) for increasing periodicity, the angular behavior is strongly modified. This proves that the imaginary part of the optical impedance is a reliable design parameter and quantitative indicator for the angle-independence of array-based plasmonic perfect absorber geometries.

Thus, an array-based perfect absorber design which exhibits $R = 0$ at normal incidence as well as $Z'' = 0$ will not be strongly influenced by grating effects and should consequently provide the highest possible acceptance angles and, for most applications, the best performance.

One intriguing alternative approach for obtaining angle-independent perfect absorbers are systems where the plasmonic resonators are placed on the spacer layer in a disordered fashion rather than in an array. However, the numerical design and optimization of such structures is challenging due to the very large

computational domains associated with disordered systems. Consequently, we start our numerical design process with an array-based sample and optimize the geometry to obtain perfect absorption at the desired resonance wavelength. A disordered geometry with a similar surface coverage is then realized experimentally using colloidal nanofabrication.¹⁷⁹ For such disordered samples, our measurement method enables high-throughput characterization of the angular response of such structures at a wide range of operating wavelengths.

Figure 5.10a shows spectral angular reflectance measurement of a disordered Au-based perfect absorber with disk diameter 160 nm, disk height 20 nm, MgF₂ spacer height 40 nm, and mirror thickness 120 nm. Importantly, this Au-based absorber works in the red part of the visible spectral range, where the design of angle-independent perfect absorbers is challenging. The disordered Au nanodisks were produced using colloidal etching lithography (see SEM image in Fig. 5.10b, fabrication details can be found in Ref.¹⁷⁹).

In this system, we observe a high absorbance of $A = 92\%$ at a wavelength of 780 nm for normal incidence, which remains above 90% for acceptance angles up to $\theta = \pm 36^\circ$. The performance of the disordered design can be understood in terms of our impedance matching model by considering two determining factors: the local impedance matching of individual absorber elements, and the suppression of inter-particle coupling and grating effects via their spatial arrangement.

To first examine the local impedance matching, we calculate the optical impedance of an individual perfect absorber element consisting of one Au nanodisk stacked above a MgF₂ spacer layer and an Au mirror. This simulation is carried out using a FDTD approach (Lumerical FDTD Solutions). To this end, a single particle calculation employing a cubic 450 nm total-field-scattered-field source containing the complete absorber geometry (120 nm Au mirror, 40 nm MgF₂ spacer, and one single Au disk with diameter 160 nm and height 20 nm) is carried out.

The entire FDTD simulation domain spans a 5 μm side length cube bounded by perfectly matched layers. The boundaries of the scattered-field region, which coincide with the boundaries

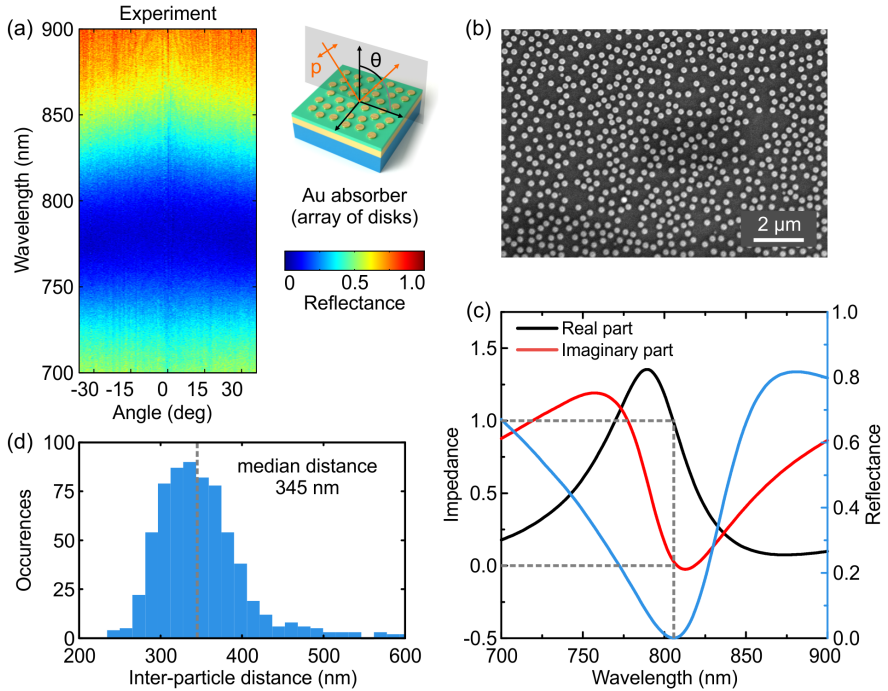


Figure 5.10: (a) Spectral angular reflectance measurements on a disordered Au-based perfect absorber in the 800 nm wavelength range. (b) SEM image of the disordered absorber structure. (c) Simulated reflectance and optical impedance of an individual Au disk perfect absorber element. Both the real and the imaginary parts of the optical impedance are perfectly matched to the vacuum values of one and zero. (d) Histogram of the median inter-particle distances extracted from the SEM image in b. We find a median distance of around 345 nm with a standard deviation of 140 nm. Due to the disorder and the spread of available periodicities, grating effects are effectively suppressed.

of the simulation domain, were chosen such that the fields at the Au mirror were already sufficiently decayed to ensure the convergence of the simulation. This isolates the absorptive performance of a single absorber element.

The impedance extracted from this simulation is thus equivalent to the impedance of a surface covered with non-interacting absorber elements of an average density of at least $1/(450\text{ nm})^2$, effectively excluding grating effects. The amplitude and phase of a normal incidence backward scattered wave were then extracted. In order to obtain the scattering matrix parameter S_{11} from this, we corrected for the propagation phase from the source to the absorber and back to the monitor. The impedance is then calculated according to Eq. (5.2).

The results of this simulation are shown in Fig. 5.10c. We find a distinct reflectance minimum close to the experimental resonance position, as well as perfect matching of the real and imaginary parts of the optical impedance to vacuum values of one and zero. Thus, when considered separate from possible grating contributions, our design should already exhibit excellent angle-independent performance.

Regarding the spatial arrangement of the individual absorber elements, there are two crucial requirements for angle-independence: The inter-particle distance needs to be large enough to prevent near-field coupling of adjacent resonators, and the spatial arrangement of the particles needs to deviate sufficiently from an exact array to suppress the formation of grating modes.

In our sample, the Au nanodisks form a disordered structure with a surface coverage of approximately 25%, corresponding to a half-pitch grating in the array case. To further quantify the particle distribution in our sample, we extract the locations of all nanodisks from the SEM image and find a median inter-particle distance of around 345 nm with a standard deviation of 140 nm (Fig.5.10d). Considering the strong decay of plasmonic near-fields on the order of several tens of nanometers, this yields mostly uncoupled single plasmonic absorber structures.^{180,181}

Together with the fabrication-induced disorder, the significant spread of inter-particle distances (which constitute different available periodicities) in the system leads to an effective suppression

of grating effects.¹⁸² Thus, the perfect impedance-matching of individual perfect absorber elements combined with a suppression of the grating contribution yields fully angle-independent performance.

In summary, we have developed and verified a quantitative model for the angular behavior of plasmonic perfect absorber structures based on the optical impedance picture. Using high-throughput angle-resolved reflectance measurements and numerical simulations, we have found that it is crucial to match both the real and imaginary parts of the optical impedance to vacuum values to obtain “true” angle-independent perfect absorption. Especially, we identified the imaginary part of the impedance as a reliable design parameter and quantitative indicator for the angle-independence of plasmonic perfect absorber geometries.

Our model was successfully verified for both array-based and disordered perfect absorber geometries in the visible and near-infrared spectral ranges, and can be easily extended towards other resonance wavelengths. The insights gained from the presented impedance model enable the rapid design of angle-independent plasmonic perfect absorber geometries, and will lead to a multitude of applications of absorbing elements with high acceptance angles in the future.

5.3 YTTRIUM NANOSTRUCTURES FOR RECONFIGURABLE ANTENNAS AND ABSORBERS

In a push towards novel applications, plasmonics research has recently focussed on moving from passive geometries towards nanophotonic devices with active control over the optical properties. One particular goal has been the development of plasmonic structures which can be reconfigured using external stimuli such as laser pulses, mechanical strain, heat, or electrical currents.

From a materials science point of view, this requires the replacement of commonly used but passive plasmonic materials like silver and gold with novel materials with active external control over their dielectric properties.

Phase change materials provide an ideal toolkit for the realization of such active nanodevices and several materials with heating- or laser-induced switching behavior such as vanadium-dioxide (VO_2)¹⁸³, gallium lanthanum sulphide (GLS)¹⁸⁴ or germanium antimony telluride (GST)⁵⁴ have already been investigated in the context of plasmonics.

Taking a somewhat different approach, Huiberts et al. discovered a switchable mirror effect in thin films of yttrium when exposed to hydrogen gas.³⁷ They demonstrated that a fully reflecting metallic yttrium mirror becomes dielectric and almost completely transparent after absorbing a sufficient amount of hydrogen. This work was expanded to the field of nanoparticles by Stepanov et al., who showed that hydrogenated spherical yttrium nanoparticles under ultrahigh vacuum conditions can have switchable Mie resonances.¹⁸⁵ However, no detailed studies of the reversible switching of yttrium under standard atmospheric conditions have been carried out.

In this section, we demonstrate the design, fabrication, and full optical characterization of reconfigurable YH_x nanoantennas, which exhibit a pronounced plasmonic resonance in their metallic YH_2 state.* The resonance wavelength and width can be

* Parts of this section are adapted from N. Strohfeldt, A. Tittl et al., *Yttrium Hydride Nanoantennas for Active Plasmonics*, *Nano Letters* **14**, 1140-1147 (2014). Reprinted with permission. Copyright 2014 American Chemical Society.

widely tuned through a straightforward variation of the antenna dimensions.

In contrast to the very small, bottom-up produced nanoparticles from Stepanov et al., we demonstrate antennas and antenna assemblies with large oscillator strength and varying size, showing custom-designed plasmonic properties in the near- and mid-IR spectral regions. The transition between metallic and dielectric yttrium hydride antennas is induced by simple hydrogen exposure from the gas phase under ambient atmospheric conditions and shows a drastic change of the spectral response.

Compared to other promising phase change materials used in plasmonic devices, yttrium dihydride has the advantage of comparatively low intrinsic damping and can therefore support plasmonic resonances itself, whereas the metallic phases of VO₂, GST, or GLS are known to exhibit only a weak plasmonic response, if any. Despite the advantage of much faster switching times, they can often be used only in hybrid plasmonic systems, i.e., in combination with gold or other good plasmonic metals.

However, the use of hybrid systems drastically lowers the optical switching contrast, since only the dielectric environment of the resonant material changes and not the antenna itself. Therefore, yttrium dihydride is a highly relevant and very promising alternative for plasmonic applications that require a high switching contrast and are less dependent on ultrashort switching times. Furthermore, as a metal, yttrium and its hydrides can be structured easily using standard nanofabrication techniques.

During hydrogen absorption, metallic yttrium (Y) transforms first into yttrium dihydride (YH₂, Fig. 5.11a), which has an even higher electrical conductivity than pure yttrium. This transition from a metal in hcp configuration into a fcc metal is non-reversible under normal conditions. Through further exposure to hydrogen, the material undergoes a second, reversible, phase change into yttrium trihydride (YH₃, Fig. 5.11b), a transparent semiconductor with hcp structure. More details on this phase transition can be found in section 2.5.2.

The transition from YH₂ to YH₃ induces strong and reversible changes in the dielectric properties that can be triggered at low partial pressures of hydrogen. Even though yttrium hydride thin

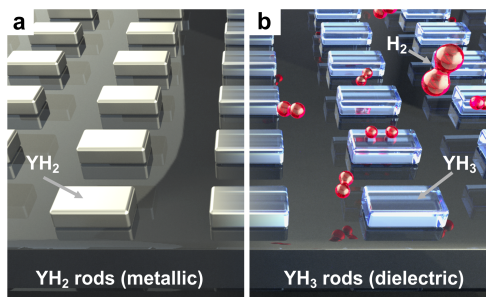


Figure 5.11: (a) Schematic drawing of a metallic yttrium dihydride (YH₂) nanorod array on a fused silica substrate in hydrogen-free environment. (b) Formation of dielectric yttrium trihydride (YH₃) nanorods under hydrogen exposure. (c) Exemplary SEM image of the fabricated YH₂ nanorods.

films exhibit a large hysteresis effect,¹⁸⁶ the ability to switch reversibly (in the sense that after a full hysteresis loop it returns to the original dihydride phase) from metal to a transparent semiconductor upon hydrogen absorption makes yttrium an attractive candidate for active plasmonic applications.

Moreover, due to the drastic change from metal to insulator, the plasmonic response vanishes completely when the yttrium is in the trihydride phase and recovers when switched back into the yttrium dihydride phase.

In order to demonstrate the functionality of such a switchable plasmonic system, we fabricate arrays of yttrium nanorods. We choose nanorods as a model system because they exhibit a strong plasmonic response and approximately dipole-like behavior and therefore constitute an ideal development platform for new plasmonic materials such as yttrium dihydride.

To realize this system experimentally, we prepare a PMMA mask on a fused silica substrate using a standard electron-beam lithography process. Afterwards, yttrium and platinum are evaporated onto the developed PMMA mask via electron beam assisted evaporation. Platinum on top of the yttrium rods serves as catalytic layer to dissociate the H₂ molecules into atomic hydrogen. Hydrogen can then be incorporated into the yttrium lattice to form the hydride states.

Catalytic materials such as platinum or palladium next to yttrium are necessary because yttrium itself is not able to catalytically dissociate H_2 molecules into atomic hydrogen. Additionally, the platinum cover prevents oxidation at the top surface of the yttrium rods. Such oxidation is common in transition metals like yttrium, which easily form an oxide layer (Y_2O_3) of several nanometers when exposed to oxygen.¹⁸⁵ This impedes hydrogen from penetrating into the particle volume. Although the thin layer of platinum introduces some additional damping to our system, the overall influence on the plasmonic response is weak.

Figure 5.12 shows typical extinction spectra of the different hydrogenation states of yttrium nanoantennas measured with a commercial Fourier transform infrared spectroscopy system (Bruker FTIR) and an incident electric field polarization parallel to the rods. Here, the rods have dimensions of $385\text{ nm} \times 160\text{ nm}$ and a height of 50 nm yttrium plus 6 nm platinum.

Pure yttrium is a metal with relatively low electrical conductivity¹⁸⁷ and therefore Y nanoantennas do not exhibit a distinct plasmonic response in the visible and near-IR spectral region (Fig. 5.12, grey dotted line). The decrease in extinction towards longer wavelengths can be attributed to the tail of a very strong and broad electronic resonance at about 3.1 eV (400 nm).¹⁸⁸

In contrast to Y, YH_2 is a good metal with a markedly different atomic and electronic structure.¹⁸⁵ To transform the yttrium into YH_2 , we expose our sample to $4\text{ vol.}\%$ hydrogen in nitrogen for 10 min . According to literature, this is more than sufficient to reach the dihydride and even the trihydride state.¹⁸⁷

However, the transition between yttrium and YH_2 is non-reversible at room temperature, whereas the second transition between YH_2 and YH_3 is fully reversible. Therefore the rods automatically settle in the YH_2 state after the hydrogen is turned off and equilibrium is reached.

The red line in Fig. 5.12 shows an extinction spectrum of such a hydrogenated rod array in the YH_2 state. The YH_2 rods have a clear extinction maximum at approximately 1720 nm that can be attributed to a localized surface plasmon resonance. This YH_2 state can be seen as the ground state of our switchable plasmonic structure, because the system will not return to the unhydrided

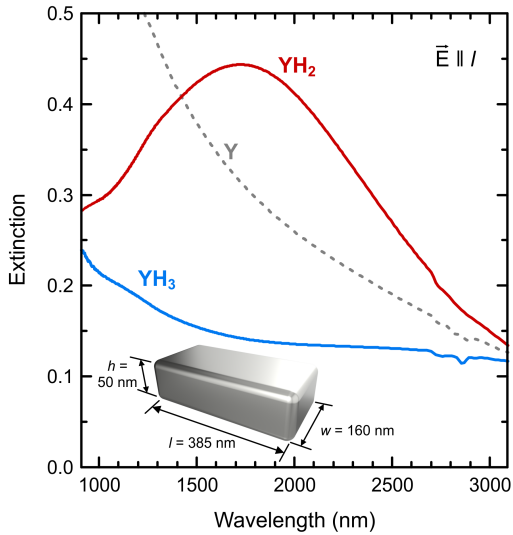


Figure 5.12: Extinction spectra of yttrium, YH_2 and YH_3 nanorods. The metallic YH_2 rods (red line) show a distinct particle plasmon resonance at 1720 nm. In contrast, the YH_3 rods (blue line) are almost transparent in the same spectral region. The increased extinction in Y nanorods (grey dotted line) towards lower wavelengths can be attributed to the tail of an electronic transition occurring at around 400 nm.

state without extremely harsh and destructive measures such as strong heating and ultra-high vacuum. Therefore the yttrium nanostructure can only be switched reversibly between the dihydride and trihydride phase. However, this does not constitute a disadvantage, since there is a large contrast in extinction between YH_2 and YH_3 (see Fig. 5.12).

When continuously exposed to hydrogen (in this case 5 vol.% H_2 in N_2 carrier gas at room temperature), the yttrium nanostructures switch into the trihydride phase within seconds. This dramatic change from a metal to a Mott-insulator also leads to a drastic change in the extinction spectrum. In fact, yttrium hydride is one of the few strongly correlated systems with a continuous Mott-Hubbard metal-insulator transition.¹⁸⁹

The particle plasmon resonance fully vanishes and the extinction spectrum becomes almost flat, as shown by the blue line in Fig. 5.12. This proves that it is possible to completely turn off the plasmon resonance by introducing only small amounts of hydrogen into the system.

The switching results in a relative extinction change at the peak wavelength (1720 nm) of almost 70 %, which translates to an absolute change in transmittance of 23 % that can easily be observed by the naked eye. Thus, such a nanorod system may serve as a versatile basic building block for active plasmonic devices with a variety of applications.

As a first example, a reconfigurable perfect plasmonic absorber in the near-infrared which utilizes yttrium as the active material is presented. The proposed design is shown in Fig. 5.13. The structure consists of square Au/Y nanostacks placed on top of a platinum (Pt) mirror. Compared to previous passive perfect absorber designs,¹⁴ the dielectric spacer layer in the absorber geometry is replaced with an yttrium nanopatch to obtain active control over the absorptive properties via the environmental hydrogen concentration.

Importantly, square gold nanoantennas are used on top of the nanostacks instead of a platinum layer as shown in Fig. 5.11. This allows for sharper resonances compared to Pt, which has much higher intrinsic damping. This change of the reaction environment necessitates the inclusion of a platinum mirror, which is

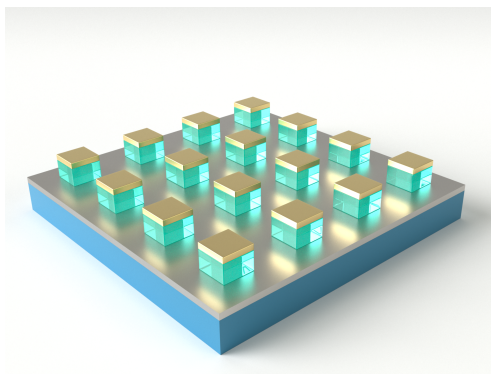


Figure 5.13: Proposed reconfigurable perfect absorber design. The structure consists of square Au/Y nanostacks placed on top of a platinum mirror.

required for the catalytic splitting of hydrogen molecules for subsequent diffusion into the yttrium lattice.

To obtain a functional design for this reconfigurable absorber concept, we again calculate reflectance spectra for a multitude of parameter combinations of the geometric parameters nanostack side length and ‘spacer height’, which denotes the thickness of the square Y nanopatch.

The heights of the square Au nanoantennas in the nanostack and the Pt mirror are fixed at 20 nm and 200 nm, respectively. Periodicity in both directions is 450 nm. Importantly, we perform this calculation with the yttrium already in the dihydride (YH_2) state, since the Y to YH_2 transition is irreversible at room temperature, as mentioned above.

The reflectance minimum in the wavelength range from 700 to 1750 nm is extracted from the full calculated reflectance spectra and shown, color coded, in Fig. 5.14. A region of minimum reflectance can clearly be identified for nanostack side lengths around 220 nm and spacer heights around 90 nm.

To further explore the possible switching contrast of our reconfigurable perfect absorber device, we calculate reflectance spectra for an optimized design for both the YH_2 and YH_3 state of the spacer nanopatch. Structure parameters are: nanostack

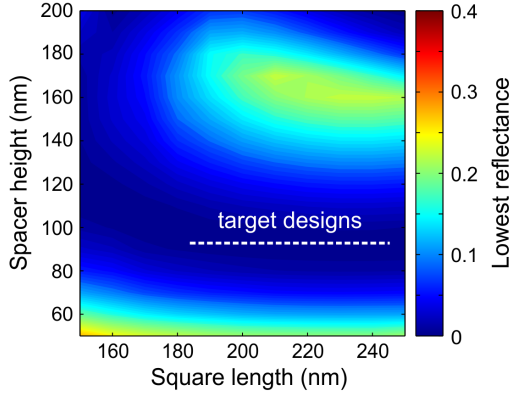


Figure 5.14: Numerical design of the reconfigurable perfect absorber device. Color coded simulated lowest reflectance values for different values of the square nanostack side length and spacer height are shown. A large number of parameter pairs suitable for perfect absorption in the near-infrared can be identified.

side length 210 nm, periodicity 450 nm, Au antenna height 20 nm, YH_2/YH_3 nanopatch height 90 nm, Pt mirror height 200 nm.

Focusing first on the YH_2 state, we find pronounced reflectance dip at a resonance wavelength of around $\lambda_{\text{YH}_2} = 800$ nm with a reflectance $R_0 < 1\%$, indicating near-perfect absorption (Fig. 5.15, red line). When moving from the dihydride (YH_2) to the trihydride (YH_3) state, the resonance undergoes a large spectral redshift of $\Delta\lambda = 600$ nm to $\lambda_{\text{YH}_3} = 1400$ nm while maintaining very high absorbance (Fig. 5.15, blue line). This leads to very large absolute reflectance contrast values of $\Delta R = 0.55$ and $\Delta R = 0.7$ at the YH_2 and YH_3 resonance wavelengths of λ_{YH_2} and λ_{YH_3} , respectively.

Due to the high absorbance $A > 95\%$ in both states combined with the pronounced spectral shift $\Delta\lambda$, our reconfigurable absorber design allows to switch between two distinct absorption bands in the near-infrared. This behavior is enabled by a conceptual advantage of such perfect absorber designs: the ability to obtain near-perfect absorptive performance for different Au nanoantenna configurations and a single thickness of the spacer nanopatch.^{14,23}

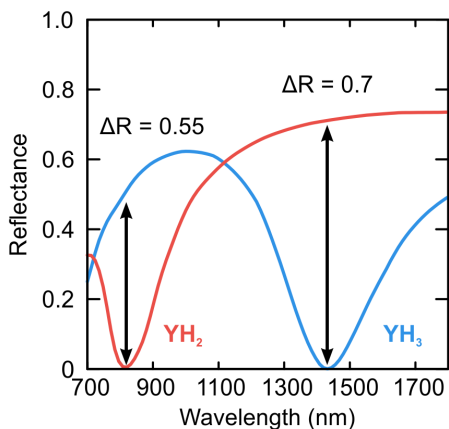


Figure 5.15: Calculated switching performance of the reconfigurable perfect absorber when going from the yttrium dihydride (YH_2 , red line) to the yttrium trihydride (YH_3 , blue line) phase upon hydrogen exposure. The resonance undergoes a pronounced redshift of $\Delta\lambda = 600\text{ nm}$ while maintaining very high absorbance. The side length of the nanostack is 210 nm and the height of the YH_2/YH_3 nanopatch is 90 nm.

Even though the presented design offers excellent optical performance, there are some challenges when trying to integrate it into a technologically viable device. First, switching between the two states requires a change of the environmental hydrogen concentration, which may require complex gas mixing and monitoring equipment. Second, whereas the transition from YH_2 to YH_3 occurs on the order of seconds, the relaxation of the system back into the YH_2 state can take several hours.¹⁸⁶ The hydrogen unloading process can be sped up by external heating or by applying vacuum, however, such approaches may not be feasible for every application.

Consequently, different active materials are needed to produce perfect absorber devices with faster switching dynamics of the optical absorption control. This topic is explored further in the next section.

5.4 SWITCHABLE MID-INFRARED PLASMONIC PERFECT ABSORBER FOR MULTISPECTRAL THERMAL IMAGING

Optical imaging devices in the mid-infrared play a key role for many technological applications in areas as diverse as thermography, surveillance, automotive safety, and astronomy. A fundamental enabling factor for the crucial technological importance of mid-infrared optical imaging devices are the atmospheric transmission windows in the 3-5 μm and 8-12 μm spectral ranges, allowing such devices to work independently of water vapor, dust, or other atmospheric disturbances.¹⁹⁰

Traditional microbolometer arrays utilize temperature sensitive pixels combined with a broadband absorbing layer to image spectrally uniform objects. To effectively detect and differentiate objects with distinct temperatures and corresponding peak blackbody emission wavelengths, spectrally selective absorptive coatings are needed.¹⁹¹ Further requirements for such absorbers are the ability to resolve several different wavelengths simultaneously, known as multispectral imaging,¹⁹² and the possibility of active control over the absorptive performance for band-selectivity, background-correction, and lock-in detection approaches.¹⁸⁴ As introduced in section 2.4, plasmonic perfect absorbers can provide important building blocks for efficient and highly selective absorbing elements with a variety of working wavelengths.

However, in order to use plasmonic absorbers in a microbolometer geometry, it is crucial to integrate the plasmonic structures on areas on the order of, or smaller than, the current industrial state of the art for microbolometer pixels in the 20 μm range.^{193,194} Furthermore, a suitable material system has to be chosen, which combines active optical control and full compatibility with standard industrial chip processing technology.

This section presents the design and experimental realization of a mid-infrared plasmonic perfect absorber with switchable absorption control and multispectral thermal imaging capability at sub-10 μm pixel sizes.* Our fully CMOS compatible design

* This section is adapted from A. Tittl et al., *A Switchable Mid-Infrared Plasmonic Perfect Absorber with Multispectral Thermal Imaging Capability*, *Advanced Materials*, DOI: 10.1002/adma.201502023 (2015). Reprinted with permission. Copyright 2015 WILEY-VCH Verlag GmbH & Co. KGaA.

incorporates arrays of square aluminum nanoantennas above a germanium antimony telluride (GST) spacer layer and an aluminum mirror. By tailoring the size of the resonant nanoantennas, we achieve efficient and wavelength-tunable absorption in the 3-5 μm atmospheric window with peak absorbance larger than 90%.

Utilizing the amorphous to crystalline phase transition in GST, our device offers band-selective active absorption control with strong reflectance contrast and a phase-change-induced spectral shift of up to 25%. Using pixels with spectrally distinct absorption bands on a single chip, our design achieves simultaneous multispectral and temperature-selective absorption, making it ideally suited for advanced imaging applications in materials science, chemistry, and defence.

The basic building blocks of our design are absorber pixels consisting of an array of square aluminum (Al) nanoantennas stacked above a $\text{Ge}_3\text{Sb}_2\text{Te}_6$ (GST-326) spacer layer and an Al mirror (Fig. 5.16a). Each absorber pixel is uniquely characterized by the side length d of the Al nanoantennas, which determines the resonance wavelength, and by the total size of the array, referred to as the pixel size.

In contrast to other hybrid absorber designs,^{195,196} we utilize Al instead of gold (Au) for the metal nanostructures and mirror to obtain a device which is fully compatible with industry standard complementary metal-oxide-semiconductor (CMOS) wafer-scale processing technology. Furthermore, the choice of Al avoids Au-GST interdiffusion, which impedes the GST phase transition in switching experiments.⁴⁷

Compared to previous thin-film-based approaches,^{51,183,197} the resonant plasmonic character of our device enables straightforward geometrical wavelength tunability by varying the antenna side length and allows our design to efficiently absorb radiation for a wide range of design wavelengths. In principle, there are two limiting factors for this geometrical tunability: the minimum structure size of the Al nanoantennas, as determined by the fabrication method, and the periodicity of the antennas, which needs to be small enough to prevent coupling of the grating mode to the absorber resonance.¹⁷⁸ Working within these constraints, a

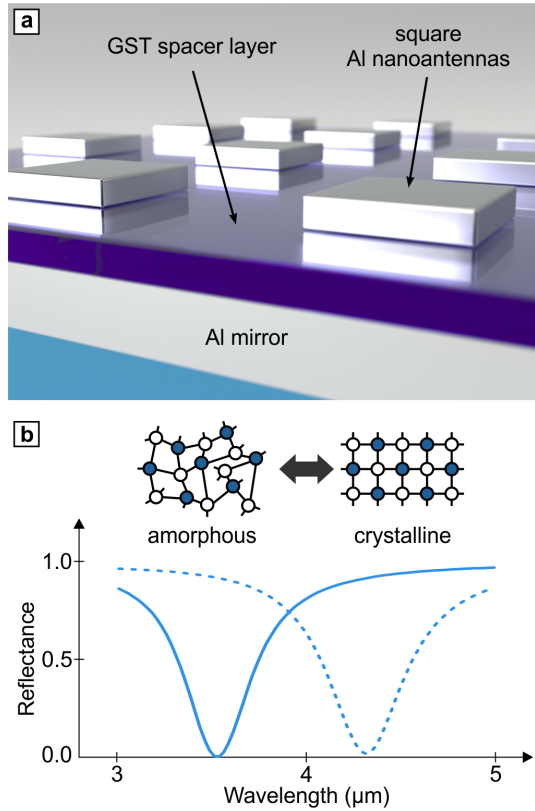


Figure 5.16: *Switchable plasmonic perfect absorber in the mid-infrared.* (a) Sketch of the switchable absorber device. Arrays of square aluminum (Al) nanoantennas are stacked above a spacer layer of the phase change material GST-326 and an Al mirror. (b) Working principle of our temperature-selective perfect absorber device. The amorphous to crystalline phase transition in GST and the associated refractive index change result in a pronounced resonance redshift.

tuning range from the near-infrared to the 8-12 μm long-wave infrared (LWIR) atmospheric window can easily be achieved with our design.

In particular, we optimize our absorber geometry to exhibit near-perfect absorption at a given wavelength in the 3-5 μm mid-wave infrared (MWIR) atmospheric window (Fig. 5.16b, solid line). The MWIR spectral range plays a key role in industry, since it covers wavelengths where objects with temperatures ranging from approximately 300 to 700 $^{\circ}\text{C}$ exhibit peak thermal emission. Thus, each individual absorber pixel with a given resonance wavelength will most efficiently absorb radiation associated with a corresponding temperature. Integrated as the absorbing layer on top of a microbolometer geometry, this results in an imaging device with sensitivity for thermal radiation ideally suited for applications in materials science, industrial process monitoring, and exhaust tracking.

To achieve the switchable, temperature-selective performance of our design, we utilize the amorphous to crystalline phase transition in GST-326, which is selected due to its lower mid-infrared losses compared to more common stoichiometries.^{54,198} As prominent examples of chalcogenide-based phase change materials, GST compounds are widely used in rewritable optical data storage.^{199,200} They can be stabilized in two different phases (amorphous and crystalline) at room temperature, which show significant contrast in their optical and electrical properties.⁴⁶

This non-volatility at room temperature constitutes a significant advantage over active optical devices based on vanadium dioxide,^{183,197} which undergoes a semiconductor-to-metal phase transition when heated above a transition temperature of 67 $^{\circ}\text{C}$ in bulk.²⁰¹ However, since vanadium dioxide requires constant heating above the transition temperature to maintain the material in its high-temperature state, it is not well-suited for incorporation in a microbolometer-targeted absorber device. Also, the previously reported vanadium dioxide absorber designs were intrinsically broadband, whereas our approach allows for narrowband and spectrally tunable absorption, even for the large acceptance angles associated with practical devices.¹⁷⁸

As a further benefit, the GST phase transition is reversible and can be induced by external heating or triggered optically on nano- and possibly even picosecond timescales.^{47–50} In recent years, these advantageous properties have enabled several active plasmonic devices based on GST.^{47,54,202} Electrical switching on very fast timescales is also possible.^{51–53}

In our design, the amorphous to crystalline phase transition and the associated strong refractive index increase cause a pronounced redshift of the perfect absorber resonance (Figure 1b, dashed line). Importantly, the high absorbance of our design is maintained for both phases of the GST spacer layer, allowing us to switch between two spectrally distinct mid-infrared absorption bands for a single antenna length. The spectral locations of the two bands can again be related to temperatures of thermal radiation, thus allowing for the temperature-selective performance of our device.

To first demonstrate wavelength-tunable and switchable perfect absorption in the mid-infrared, we fabricate $100\ \mu\text{m} \times 100\ \mu\text{m}$ absorber pixels consisting of Al nanoantenna arrays with varying antenna side lengths d , stacked above a 85 nm GST-326 spacer layer and a 100 nm Al mirror. The height and periodicity of the nanoantennas are fixed at 40 nm and 800 nm, respectively, for all devices presented in this manuscript. Figure 5.17a depicts the reflectance from two representative absorber pixels before (solid lines) and after (dashed lines) the heat-induced amorphous to crystalline transition, measured using a FTIR spectrometer with attached microscope.

Our design exhibits low reflectance and hence very high absorbance in the MWIR spectral range, with a peak absorbance value of at a wavelength of $3\ \mu\text{m}$. Furthermore, our design allows for the straightforward geometrical tuning of the resonance wavelength via a variation of the nanoantenna side length d . Figure 5.17b shows SEM images of the two nanoantenna arrays with antenna side lengths of $d = 400\ \text{nm}$ and $d = 450\ \text{nm}$, which correspond to resonance wavelengths of $2.75\ \mu\text{m}$ and $3\ \mu\text{m}$, respectively. Importantly, our design is not limited to these wavelengths, and full geometrical tunability of the perfect absorber

resonance over the whole MWIR spectral range is experimentally demonstrated in Fig. 5.20.

Furthermore, due to the incorporation of square nanoantennas and a low-periodicity impedance matched design,¹⁷⁸ our device offers full polarization independence and high absorptive performance for incidence angles up to 65° , as confirmed by numerical simulations of the system.

To obtain active control over the absorptive behavior, we induce the amorphous-to-crystalline phase transition in GST-326 by heating the sample above the phase transition temperature of 160°C .⁵⁴ Specifically, our samples are placed on a 180°C hot plate under nitrogen atmosphere for 30 minutes to avoid oxidation of the GST layer. When performing switching experiments in air, this effect may be avoided by covering the entire sample with a very thin 10 nm ZnS/SiO₂ capping layer.²⁰²

During the phase transition, the resonances undergo a pronounced redshift of up to $0.7\ \mu\text{m}$, or 25% of the resonance wavelength, while maintaining high absorbance. This behavior is caused by the strong refractive index increase of phase change materials such as GST-326 when going from the as-deposited amorphous ($n = 3.5$) to the crystalline ($n = 6.5$) phase.^{46,54} Because of the strong phase-change-induced spectral shift and the low full width at half maximum (FWHM) of approximately $0.5\ \mu\text{m}$, our absorber device exhibits a pronounced reflectance contrast of $\Delta R = 0.6$ at resonance.

Compared to recent GST-based thin-film approaches,⁵¹ our design can achieve resonant absorption with low FWHM over the full working range of the device, providing increased reflectance contrast. Additionally, the active absorption control and band-selectivity in our device represents a clear advantage over current passive mid-infrared absorber designs.^{203–206}

Common wavelength-tunable plasmonic perfect absorber devices are fabricated lithographically and feature nanostructured areas on the order of $100\ \mu\text{m} \times 100\ \mu\text{m}$. However, to enable advanced technological applications such as high-resolution imaging, plasmonic printing, color filtering, or novel displays,^{207–212} current plasmonic and nanooptical designs need to be imple-

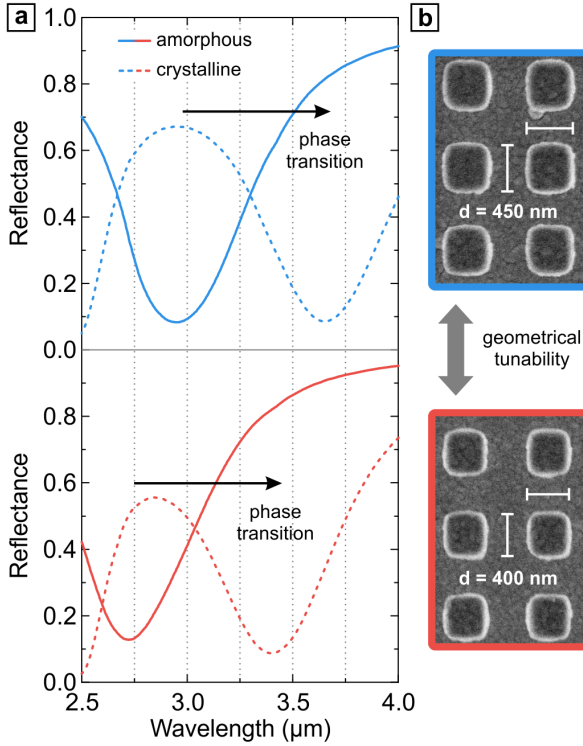


Figure 5.17: Wavelength-tunable and switchable absorption in the mid-infrared.

(a) Our design exhibits low reflectance and hence very high resonant absorption ($A > 90\%$) in the MWIR spectral range. Geometrical tunability of the resonance wavelength is achieved by varying the side length d of the resonant square Al nanoantennas, with larger antennas corresponding to higher resonance wavelengths. Structure dimensions are $d = 400 \text{ nm}$ (blue lines) and $d = 450 \text{ nm}$ (red lines). Full tunability of the resonance over the MWIR spectral range is demonstrated in Fig. 5.20. When heating the sample above the GST crystallization temperature of 160°C , the resonance undergoes a pronounced phase-change-induced spectral redshift of up to $0.7 \mu\text{m}$ while maintaining high absorbance (dashed lines). This results in a pronounced reflectance contrast of up to $\Delta R = 0.6$ at resonance for $d = 450 \text{ nm}$. (b) SEM images of the two representative perfect absorber devices with the GST spacer layer in the amorphous phase.

mented for pixel sizes approaching the device operating wavelength.

To prove the viability of the presented design for state-of-the-art microbolometer pixel sizes in the $20\ \mu\text{m}$ range,²¹³ we fabricate a checkerboard pattern composed of perfect absorber pixels with two distinct design wavelengths $\lambda_1 = 3.4\ \mu\text{m}$ and $\lambda_2 = 3.9\ \mu\text{m}$ (Fig. 5.18a). To achieve this dual-wavelength behavior, the individual absorber pixels incorporate arrays of square Al nanoantennas with antenna side lengths of $d = 400\ \text{nm}$ and $d = 500\ \text{nm}$, respectively, stacked above a $75\ \text{nm}$ GST-326 spacer layer and a $100\ \text{nm}$ Al mirror. Due to the difference in GST thickness, resonances are redshifted compared to the results for $100\ \mu\text{m}$ pixel size from Fig. 5.17.

We then image this pattern using a focal plane array (FPA) detector attached to a FTIR spectrometer, allowing us to record the full spectral response of a whole pattern simultaneously. In particular, spectroscopic infrared imaging of our perfect absorber devices (Fig. 5.18 to Fig. 5.21) was carried out with an IR microscope (Bruker Hyperion 1000) connected to a Fourier-Transform-Infrared (FTIR) spectrometer (Bruker IFS 66v/S) at the ANKA synchrotron light source (Angstrom Source Karlsruhe).

The described measurements were done with a globar to ensure a uniform illumination of the sample. The IR microscope was equipped with a liquid nitrogen-cooled mercury cadmium telluride (MCT) focal plane array (FPA) detector consisting of 64×64 elements with $40\ \mu\text{m}$ pixel pitch. A 36X magnification Schwarzschild- objective ($\text{NA} = 0.52$) was used to project a pixel size of $1.1\ \mu\text{m}$ in the focal plane, combined with a total field of view of $71\ \mu\text{m} \times 71\ \mu\text{m}$. A detailed characterization of the imaging setup is provided in literature.²¹⁴

Reflectance spectra of our perfect absorber design and a bare gold mirror were acquired between $2.5\ \mu\text{m}$ and $12.5\ \mu\text{m}$ with a resolution of $8\ \text{cm}^{-1}$ and a minimum of 100 scans. After data smoothing (a moving average Savitzky-Golay filter with a data point span of 40 and polynomial degree 2), the relative reflection is calculated and normalized in the range of 7 to $7.5\ \mu\text{m}$ to account for the different sensitivities of each pixel. Conventional infrared spectroscopic measurements as presented in Fig. 5.17 were

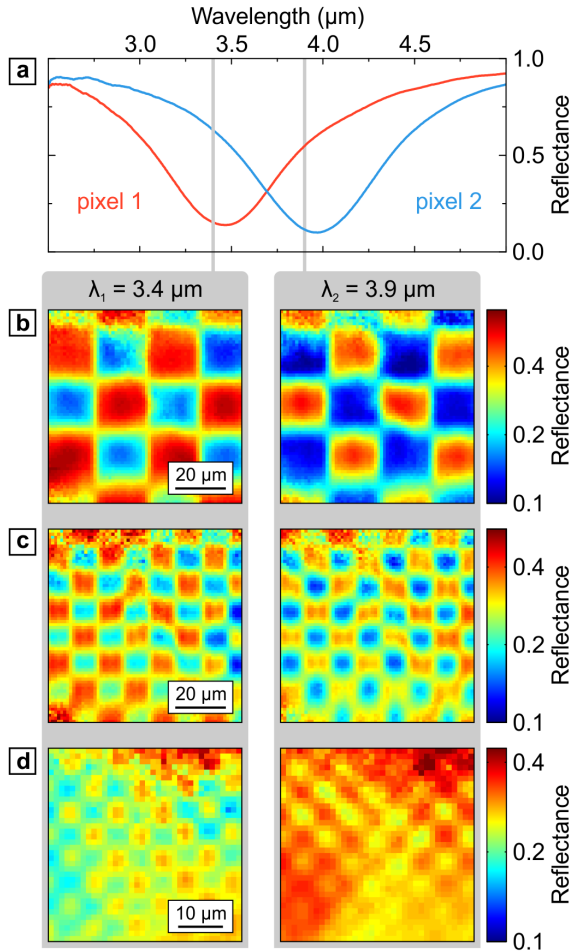


Figure 5.18: Sub-10 μm pixel size in a plasmonic perfect absorber.

The sample consists of a checkerboard pattern of absorber pixels with two different design wavelengths (3.4 and 3.9 μm). Reflectance data is recorded using a focal-plane array (FPA) detector connected to a FTIR spectrometer. (a) Representative reflectance spectra for the two pixels. (b) Color coded reflectance at the design wavelengths of the two distinct perfect absorber pixels for a pixel size of 20 μm . The pixel arrangement can be clearly distinguished. (c) Perfect absorber pixels with 10 μm size. The regular arrangement is again neatly visible. (d) Perfect absorber pixels with 5 μm size on the order of the device operating wavelength. A logarithmic reflectance scale is used in panels b-d. Please note the smaller scale bar in panel d. The GST spacer layer is in the amorphous phase for all measurements.

recorded with a single element detector in our labs as described previously.²¹⁵

The spatially resolved reflectance at the two design wavelengths is shown in Fig. 5.18b. At the first design wavelength ($\lambda_1 = 3.4\ \mu\text{m}$), square $20\ \mu\text{m} \times 20\ \mu\text{m}$ areas with low reflectance (blue color) can be clearly identified, exhibiting excellent contrast and spatial separation from adjacent areas of the pattern.

When examining the reflectance at the second design wavelength ($\lambda_2 = 3.9\ \mu\text{m}$), the situation is reversed, with reflective pixels at λ_1 now appearing absorptive and vice versa. This behavior is due to the high absorption of our device combined with the low FWHM of the resonances, which enables a spectrally non-overlapping pixelated absorber design. For a more challenging design with $10\ \mu\text{m}$ pixel size, individual pixels in the checkerboard pattern are still clearly visible with high contrast and good spatial separation (Fig. 5.18c).

When reducing the pixel size to $5\ \mu\text{m}$, which is on the order of the device operating wavelength, the reflectance contrast at the two design wavelengths is decreased. However, individual pixels containing only 6×6 Al nanoantennas can still be clearly distinguished. Importantly, this pixel size is close to the diffraction limit of mid-infrared radiation and approaches the ultimate limit of a single resonant nanostructure pixel.

Building on this two-wavelength design, we now extend our perfect absorber device towards multispectral absorption in the mid-infrared, allowing for the simultaneous imaging of several distinct wavelength bands, similar to the RGB color filter arrays in digital camera sensor chips. To achieve this, we utilize a conceptual advantage of our design: the ability to obtain near-perfect wavelength-tunable absorptive performance for different nanoantenna side lengths on a single GST spacer layer thickness.

This enables pixelated patterns with a wide range of different operating wavelengths on a single integrated infrared absorber chip. The maximum number of absorption bands that can be implemented without significant spectral overlap is highly dependent on the FWHM of the resonant absorption, which has an experimental value of around $0.5\ \mu\text{m}$ in our design. Considering a minimum spectral separation of adjacent absorption bands

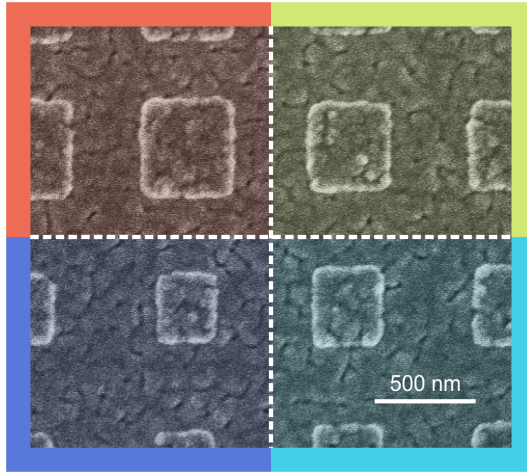


Figure 5.19: SEM image of the multispectral absorber design. Square Al nanoantennas with sizes ranging from 300 to 450 nm in 50 nm steps are clearly visible. The GST spacer layer is in the crystalline phase for this measurement.

on the order of the FWHM, this yields a limit of five distinct absorption bands in the 3–5 μm MWIR range. This number can be increased by incorporating materials with lower mid-infrared losses,⁴¹ or by utilizing optical devices with more complex Fano-type lineshapes.²¹⁶

We realize this multispectral concept experimentally by fabricating a perfect absorber device with a periodic superpixel arrangement composed of four individual pixels with distinct resonance wavelengths in the 2.5 to 4 μm range. The design integrates Al nanoantenna arrays with side lengths ranging from 300 to 450 nm in 50 nm steps, stacked above a 75 nm GST-326 spacer layer and a 100 nm Al mirror (Fig. 5.19).

To more clearly demonstrate the multispectral operation of the superpixel geometry, we extract the wavelength of lowest reflectance (resonance wavelength) from spatially resolved FTIR measurements on this pattern (Fig. 5.20a). The four different design wavelengths are clearly visible with excellent spatial separation. Additionally, representative reflectance spectra from the four individual pixels clearly demonstrate the high absorptive

performance ($A > 80\%$) and non-overlapping spectral characteristics of our design even for multiple mid-infrared absorption bands (Fig. 5.20b-e).

Multispectral plasmonic device designs can simultaneously resolve multiple wavelengths of incident radiation on a single integrated detector chip. This is achieved via the geometrical tunability of the absorber resonance, which is inherently passive. In addition, the phase change tunability of our design allows for active control over the absorption performance and consequently for the switching of the absorption between different bands. Also, compared to multispectral imaging, active control of individual absorber pixels does not reduce the final resolution of the microbolometer detector chip, resulting in a more versatile device.

For further validation of the thermal imaging capability of our absorber device, we relate the spectral locations of the four distinct mid-infrared absorption bands to the peak emission wavelength of an ideal blackbody with a specific temperature via Planck's law. That is, for every resonance wavelength (Fig. 5.21a), our design is especially sensitive to the thermal emission from a heated object with a certain temperature (Fig. 5.21b). Consequently, this calculated peak detection temperature can be used to characterize the thermal detection range and temperature-selective operation of our superpixel design.

Focusing on an individual superpixel, we find multispectral thermal imaging capability for peak detection temperatures ranging from 740 to 1150 K, allowing to simultaneously resolve objects with four distinct temperatures (Fig. 5.21c). The range of detection temperatures can now be tailored by utilizing the reversible amorphous to crystalline phase transition in GST. When heating the sample above the transition temperature, the multispectral thermal imaging capability is maintained and undergoes a shift to the temperature range from 605 to 930 K, again with high absorptive performance ($A > 75\%$) and spectrally distinct absorption bands (Fig. 5.21d).

Thus, our versatile thermal imaging chip offers the ability to actively switch between different temperature ranges, enabling applications such as selective thermography and chemical imaging. Due to the wavelength tunability of our design, other tem-

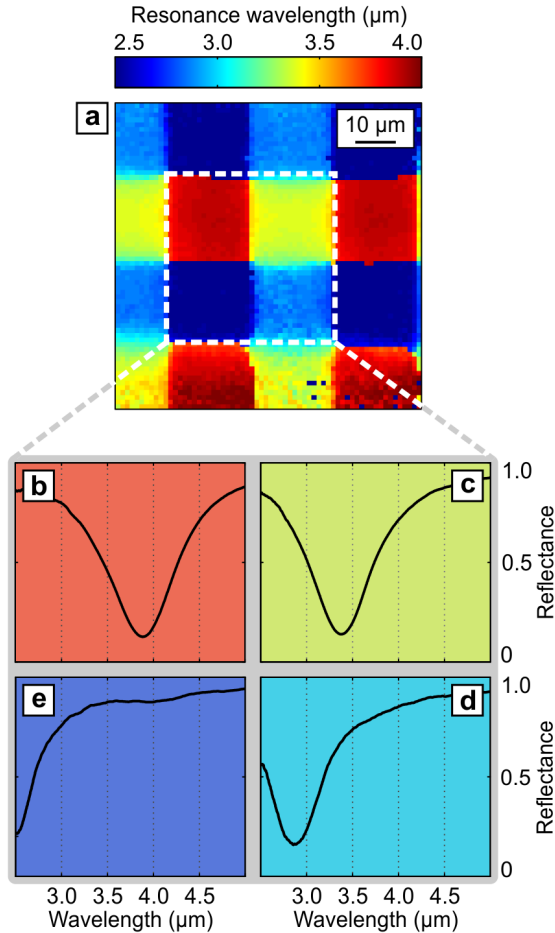


Figure 5.20: *Multispectral imaging in the mid-infrared.* (a) Color coded resonance wavelength of a four-wavelength pixelated plasmonic perfect absorber chip for multispectral imaging. Our device covers a wavelength range from 2.5 to 4 μm . This is achieved using Al nanoantenna arrays with antenna side lengths varying from 300 to 450 nm in 50 nm steps. The four individual pixels in the superpixel arrangement (white square) deliver a peak absorbance of $A > 80\%$ at resonance while providing 20 μm pixel size. (b-d) Representative reflectance spectra for the individual pixels. The resonance wavelength in panel a is taken as the reflectance minimum in the spectral range from 2.5 to 5 μm . The GST spacer layer is in the amorphous phase for all measurements.

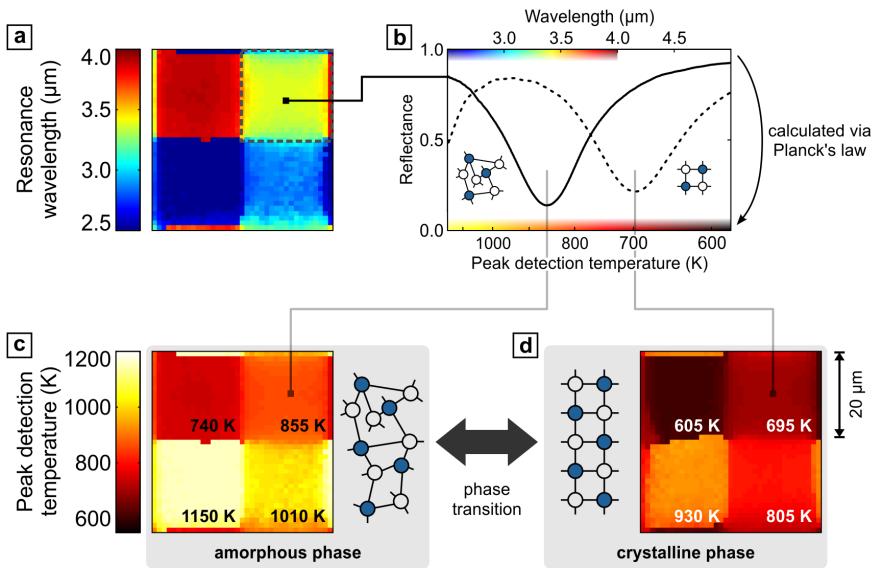


Figure 5.21: *Thermal imaging capability with switchable temperature detection range.* (a) Color coded resonance wavelength of an individual perfect absorber superpixel with four distinct mid-infrared absorption bands. (b) Representative reflectance spectra for the top right pixel from panel a with the GST layer in the amorphous (solid line) and crystalline phase (dashed line), respectively. The peak detection temperature is calculated from the resonance wavelength of the perfect absorber pixels using Planck's law. (c) Color coded peak detection temperature for the multispectral superpixel geometry. Our device offers multispectral thermal imaging capability for temperatures ranging from 740 to 1150 K. The numerical overlay in the lower right corner of each individual pixel represents the average peak detection temperature for this pixel. (d) Color coded peak detection temperature after heat-induced switching of the GST layer from the amorphous to the crystalline phase. The multispectral imaging capability is maintained and shifted to the temperature range from 605 to 930 K. Pixel size is 20 μm for all pixels shown in panels a, c, and d.

perature ranges can be implemented easily, possibly enabling the simultaneous imaging of the 3-5 and 8-12 μm spectral windows on a single detector chip.

As a first demonstration of active control in a multispectral mid-infrared perfect absorber, our device utilizes the heat-induced phase change of a GST-326 spacer layer. However, due to the robust material and phase change properties of our design, reversible optical switching should be possible as recently shown for Al nanoantenna arrays covered with a thin GST-326 film.⁴⁷ If necessary, the optical accessibility of the phase change material in our design can be optimized further by utilizing fully GST-covered Al antennas placed on a CMOS compatible dielectric spacer layer.

In order to obtain full electrical control of the absorption, our design can be extended to incorporate square germanium/Al/-GST-326/germanium nanostack structure (side length 350 nm) placed on top of an Al mirror (Fig. 5.22a). This design incorporates several design requirements for electrical switching.

First, individual nanostacks can be contacted electrically by using Germanium (Ge) to contact them to the Al back contact and to an electrode above. In our initial design, we utilize Ge to as contact material due to its optical transparency at mid-infrared wavelengths combined with its DC conductivity. The nanostack design can be easily modified to incorporate other electrode materials such as titanium nitride or indium tin oxide.⁵¹

Second, the GST is not incorporated as an extended film but as square nanostructures with dimensions of 350 nm \times 350 nm \times 20 nm, similar to previous experimental electrical switching demonstrations. The sandwich structure is embedded in PC-403, an insulating dielectric, which prevents electrical contact between the top and bottom electrodes. By applying a voltage pulse to individual nanostacks, reversible electrical switching of the nanostructured GST can be carried out.⁵¹

Further device integration on the detector chip level requires electrical connections for each individual nanostack, which can be accomplished in a cross-point geometry as demonstrated experimentally for phase change memory cells.²¹⁷

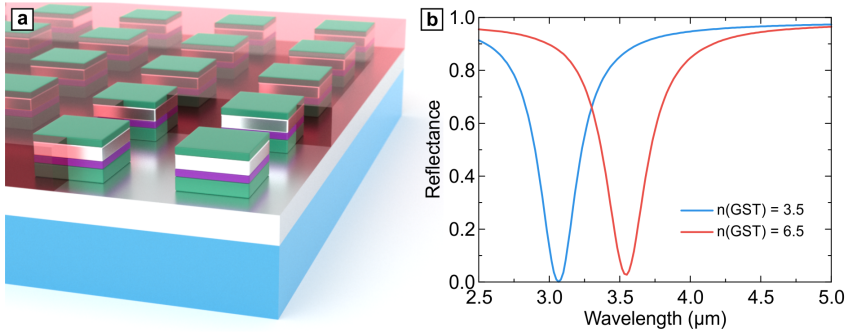


Figure 5.22: Possible perfect absorber device suitable for electrical switching.

(a) Cut-away view of a perfect absorber device suitable for electrical switching, which consists of square Ge/Al/GST/Ge nanostack structures placed on top of an Al mirror. Al nanostructures and mirror are shown in grey, germanium is green and the nanostructured GST-326 is shown in purple. The embedding dielectric PC-403 layer is shown in red. (b) Numerically calculated reflectance of the proposed design. Pronounced phase-change-induced switching is clearly visible. The blue line denotes the amorphous phase and the red line the crystalline phase.

Importantly, high reflectance contrast at resonance and pronounced phase-change-induced spectral shifts are maintained for the initial nanostack design, as shown by numerical calculations (Fig. 5.22b). Electrical switching, especially on fast timescales, may also be useful for background-correction, and lock-in detection approaches.

Moving closer to the technological realization of multispectral switchable microbolometer devices, future studies will need to focus on heat generation and transfer in the plasmonic absorption layers,^{218,219} optimizing them to exhibit both low heat capacity and high thermal conductivity. Especially, such devices may need to combine GST, which has a comparatively low thermal conductivity,²²⁰ with highly heat conducting CMOS compatible dielectrics such as aluminum nitride, to obtain microbolometer imaging devices with high sensitivity and fast response times.

In summary, we have demonstrated a switchable mid-infrared perfect absorber with temperature-selective thermal imaging capability. Our design exhibits high absorptive performance independent of incident angle and polarization, and can be integrated

in sub-10 μm absorber pixels, which enable near diffraction-limited imaging in the mid-infrared. The low FWHM of the absorption bands in our design combined with the use of a GST-326 spacer layer enables efficient band- and thus temperature-selective detection.

By simultaneously increasing the number of pixels and reducing the FWHM of the resonances in our multispectral design, more wavelengths can be resolved simultaneously, paving the way towards hyperspectral imaging and applications in meteorology, geoscience, or defence. Integrating the possibility of switching the GST-326 layer using all-optical or electrical means, our perfect absorber design can serve as a building block for highly selective absorptive coatings with ultrafast control and a wide range of design wavelengths in the future.

CONCLUSIONS & OUTLOOK

This thesis has covered a variety of hybrid plasmonic devices for applications ranging from chemical sensing to active mid-infrared imaging.

Focusing first on the all-optical detection of chemical and catalytic reactions down to very small reagent concentrations and detection volumes, the behavior of antenna-enhanced hydrogen sensing geometries was investigated using numerical simulations. Particularly, the catalytic dissociation of hydrogen molecules and the subsequent hydride formation in palladium structures was chosen as a model system.

Analyzing a palladium nanodisk placed in the nanofocus of a triangular gold nanoantenna, it was found that it is crucial to consider the hydrogen-induced lattice expansion of the palladium in addition to the dielectric change introduced during the palladium/palladium hydride phase transition.

Moving beyond top-down fabricated nanoantenna geometries, highly engineered, chemically synthesized nanosensor particles were investigated. Such plasmonic 'smart dust' geometries combine an efficient optical probe with a reagent sensitive material to obtain a wide range of functionalities.

Utilizing Au@SiO₂ core-shell nanoprobles, this concept was applied to the detection of hydrogen-induced catalytic events in adjacent palladium films of different thicknesses and morphologies. Importantly, these smart dust nanoprobles can be easily dispersed on arbitrary catalytically active surfaces, allowing for the investigation and spatial mapping of a wide range of reactions. Regarding sensitivity, it was found that a change of the palladium film thickness of only 5 nm was enough to change the sensing response by as much as 50%. Furthermore, changes of the film morphology (specifically from a 'dust on film' to a 'film on dust' arrangement) led to a complete reversal of the direction of the hydrogen-induced spectral shifts.

Whereas the previous Au@SiO₂ nanoprobles were ideal to locally map chemical reactions on extended reactive films, the detection of events involving only a very small number of molecules requires a move to extremely small sensing volumes. To achieve this, sub-5-nm palladium nanocrystals were attached to chemically synthesized gold nanorods using DNA self-assembly.

The use of DNA nanotechnology allowed for the precise positioning of the Pd satellite nanocrystals at ultrashort distances adjacent to the gold rods, making optimal use of the electric near-field enhancement next to the rod antenna. Performing optical hydrogen sensing experiments on these complex smart dust particles, it was possible to reliably track the hydrogen loading and unloading kinetics of the sub-5-nm Pd crystals at the single antenna level and in real time.

A second focus of this thesis was the investigation of plasmonic perfect absorbers, nanostructured optical devices designed to absorb all light of a certain design wavelength. Compared to smart-dust-based sensor geometries (which are ideal to push the limits of detection volume and sensitivity), perfect absorbers can act as a central building block for technologically relevant sensing applications due to their background-free detection scheme.

Applying this again to chemical sensing, a geometry of palladium nanowires stacked above a magnesium fluoride spacer layer and a gold mirror was used to detect hydrogen concentrations down to 0.5% in nitrogen carrier gas. This was achieved by optimizing the structure parameters to obtain a perfect absorber with very low reflectance and (since zero transmittance is assured via the thick gold mirror) absorbance $A > 99\%$ in the red part of the visible spectrum. Due to the near-zero reflectance at resonance, small hydrogen-induced changes of the optical response thus resulted in large relative intensity changes, enabling excellent sensitivity.

A further crucial point for technological applications is the need for angle-independence of the optical response from perfect absorber devices. This allows for enhanced stability and alignment tolerance in an integrated sensor geometry, and permits the utilization of all light from the forward-facing half-space in energy harvesting and imaging applications.

In order to understand the underlying principles of angle-independence in perfect absorbers, extensive angular reflectance measurements on various perfect absorber geometries were carried out. Comparing these results with thorough numerical simulations on the systems allowed to construct an optical impedance matching model for the optical behavior of the investigated absorber structures.

Specifically, perfect matching of the imaginary part of the optical impedance to its vacuum value of zero was identified as a crucial factor for angle-dependent performance. Building on this design rule for angle-independent perfect absorber structures, this impedance matching model was verified for an absorber geometry consisting of disordered plasmonic resonators, underlining the versatility of the approach.

Finally, this thesis focused on extending the previous concepts towards active plasmonic devices, where the optical properties can be strongly modified by an external stimulus. As a first basic building block, yttrium hydride (YH_x) nanoantennas were investigated, which allow to completely turn a plasmonic resonance on and off by controlling the external hydrogen partial pressure. Continuing from this, a switchable perfect absorber design based on Au/YH_x nanostacks placed on top of a platinum mirror was introduced.

Even though the use of yttrium hydride nanostructures yields high dynamic range, it was found that the switching times in this system were comparatively low. Especially, hydrogen desorption occurred on timescales on the order of minutes or even hours, making this material system unsuitable for optical control in realistic technological applications.

To overcome this, germanium antimony telluride (GeSbTe , or GST) was investigated for use in a mid-infrared perfect absorber geometry with active post-fabrication absorption control. As a material, GST is widely used in optical data storage applications and can be switched all-optically and electrically on nano- and potentially picosecond timescales.

The incorporation of this material enabled the realization of an active mid-infrared plasmonic perfect absorber consisting of square aluminum nanoantennas stacked above a GST-326 spacer

layer and an aluminum mirror. Absorbance $> 90\%$ was obtained experimentally in the 3-5 μm spectral range, with straightforward geometrical tunability of the resonance wavelength via the side length of the Al nanoantennas.

By utilizing the amorphous to crystalline phase transition in GST and the associated strong refractive index change, large reflectance contrast at resonance and a large spectral tuning range were realized, allowing for band- and consequently temperature-selective absorptive performance. Extending this to a pixelated design with four distinct absorption bands in the mid-infrared, an integrated perfect absorber chip with multispectral thermal imaging capability and external control over the temperature detection range was realized in a fully CMOS compatible device.

Building on the presented results, there are several promising research directions where hybrid plasmonic devices can be applied in the future.

First, the concept of silica shell-isolated smart dust nanoprobe (section 4.2) could be applied to perform spatially resolved mapping of catalytic processes on extended reactive surfaces. By dispersing numerous nanoprobe on the surface and performing imaging spectroscopy, one would be able to record time-resolved optical response of all nanoprobe in a certain viewfield simultaneously.

Correlated with electron microscopy or atomic force microscopy characterization of the reactive surface, this would allow to quantify the influence of localized defects, cracks, and other morphological deviations of the surface on the local catalytic reactions. Insights gained with such measurements could be used to further understand and optimize catalytic systems in industry and materials science.

Second, the proposed DNA-assembled bimetallic nanosensors (section 4.3) could be extended to incorporate satellite nanospheres composed of different materials, allowing for the detection of other chemically significant reagents. Furthermore, the use of such nanoprobe in biological systems could be explored, aiming to resolve the chemical reactions occurring in a variety of organisms down to the microorganism scale. This approach

would enable the all-optical and potentially *in vivo* monitoring of physiological processes with unprecedented flexibility.

Finally, the concept of an active mid-infrared metasurface (section 5.4) could be extended towards the full spatial control of the phase and amplitude of incident light, addressing the current lack of efficient mid-infrared spatial light modulators.

The basic building blocks of such a light modulating metasurface would be arrays of hybrid plasmonic oligomer structures with an adjacent GST layer, providing both a Fano-type optical response with the required phase modulation and mid-infrared transmission window as well as active external control over the optical properties.

Furthermore, by subdividing the proposed metasurface into distinct pixels with side lengths of several microns, the proposed device could be extended to obtain full spatial control over amplitude and phase of the light. Importantly, electrical switching of individual pixels could be realized using a cross-bar geometry common in phase-change memory cells, aiding technological device integration.

Going beyond the ideas outlined here, the versatility of hybrid plasmonic geometries will lead to a multitude of new designs and applications, potentially bringing nanophotonics-based concepts to technological devices that are used every day.

BIBLIOGRAPHY

- [1] J. Valentine, S. Zhang, T. Zentgraf, E. Ulin-Avila, D. A. Genov, G. Bartal, and X. Zhang, "Three-dimensional optical metamaterial with a negative refractive index," *Nature* **455**(7211), 376–379 (2008).
- [2] H. A. Atwater and A. Polman, "Plasmonics for improved photovoltaic devices," *Nature Materials* **9**(3), 205–213 (2010).
- [3] E. Boisselier and D. Astruc, "Gold nanoparticles in nanomedicine: preparations, imaging, diagnostics, therapies and toxicity," *Chemical Society Reviews* **38**(6), 1759–1782 (2009).
- [4] K. L. Kelly, E. Coronado, L. L. Zhao, and G. C. Schatz, "The Optical Properties of Metal Nanoparticles: The Influence of Size, Shape, and Dielectric Environment," *J Phys Chem B* **107**(3), 668–677 (2003).
- [5] C. L. Haynes and R. P. Van Duyne, "Nanosphere Lithography: A Versatile Nanofabrication Tool for Studies of Size-Dependent Nanoparticle Optics," *The Journal of Physical Chemistry B* **105**(24), 5599–5611 (2001).
- [6] L. J. Guo, "Nanoimprint Lithography: Methods and Material Requirements," *Advanced Materials* **19**(4), 495–513 (2007).
- [7] E. M. Larsson, S. Syrenova, and C. Langhammer, "Nanoplasmonic sensing for nanomaterials science," *Nanophotonics* **1**(3-4), 249–266 (2012).
- [8] K. M. Mayer and J. H. Hafner, "Localized Surface Plasmon Resonance Sensors," *Chemical Reviews* **111**(6), 3828–3857 (2011).

- [9] J. N. Anker, W. P. Hall, O. Lyandres, N. C. Shah, J. Zhao, and R. P. Van Duyne, "Biosensing with plasmonic nanosensors," *Nature Materials* **7**(6), 442–453 (2008).
- [10] K. A. Willets and R. P. Van Duyne, "Localized Surface Plasmon Resonance Spectroscopy and Sensing," *Annual Review of Physical Chemistry* **58**(1), 1–33 (2007).
- [11] S. Lal, S. Link, and N. J. Halas, "Nano-optics from sensing to waveguiding," *Nature Photonics* **1**(11), 641–648 (2007).
- [12] S. A. Maier, *Plasmonics: Fundamentals and Applications* (Springer, 2007).
- [13] G. V. Hartland, "Optical Studies of Dynamics in Noble Metal Nanostructures," *Chemical Reviews* **111**(6), 3858–3887 (2011).
- [14] N. Liu, M. Mesch, T. Weiss, M. Hentschel, and H. Giessen, "Infrared Perfect Absorber and Its Application As Plasmonic Sensor," *Nano Letters* **10**(7), 2342–2348 (2010).
- [15] B. Luk'yanchuk, N. I. Zheludev, S. A. Maier, N. J. Halas, P. Nordlander, H. Giessen, and T. C. Chong, "The Fano resonance in plasmonic nanostructures and metamaterials," *Nature Materials* **9**(9), 707–715 (2010).
- [16] X. Yin, M. Schaeferling, B. Metzger, and H. Giessen, "Interpreting chiral nanophotonic spectra: the plasmonic Born-Kuhn model." *Nano Letters* **13**(12), 6238–6243 (2012).
- [17] A. Tittl, "Perfect absorber sensor: towards single catalytic detection," Diploma thesis, University of Stuttgart, Germany (2011).
- [18] G. Mie, "Beiträge zur Optik trüber Medien, speziell kolloidaler Metallösungen," *Annalen der Physik* **330**(3), 377–445 (1908).
- [19] H. Kuwata, H. Tamaru, K. Esumi, and K. Miyano, "Resonant light scattering from metal nanoparticles: Practical analysis beyond Rayleigh approximation," *Applied Physics Letters* **83**(22), 4625 (2003).

- [20] M. A. Ordal, R. R. Bell, R. W. Alexander, L. L. Long, and M. R. Querry, "Optical properties of fourteen metals in the infrared and far infrared: Al, Co, Cu, Au, Fe, Pb, Mo, Ni, Pd, Pt, Ag, Ti, V, and W," *Appl Opt* **24**(24), 4493 (1985).
- [21] N. Landy, S. Sajuyigbe, J. Mock, D. R. Smith, and W. J. Padilla, "Perfect Metamaterial Absorber," *Physical Review Letters* **100**(20), 207,402 (2008).
- [22] H. Tao, C. Bingham, A. Strikwerda, D. Pilon, D. B. Shrekenhamer, N. Landy, K. Fan, X. Zhang, W. J. Padilla, and R. D. Averitt, "Highly flexible wide angle of incidence terahertz metamaterial absorber: Design, fabrication, and characterization," *Physical Review B* **78**(24), 241,103 (2008).
- [23] A. Tittl, P. Mai, R. Taubert, D. Dregely, N. Liu, and H. Giessen, "Palladium-based plasmonic perfect absorber in the visible wavelength range and its application to hydrogen sensing," *Nano Letters* **11**(10), 4366–4369 (2011).
- [24] K. Chen, R. Adato, and H. Altug, "Dual-Band Perfect Absorber for Multispectral Plasmon-Enhanced Infrared Spectroscopy," *ACS Nano* **6**(9), 7998–8006 (2012).
- [25] A. Vora, J. Gwamuri, N. Pala, A. Kulkarni, J. M. Pearce, and D. Ö. Güney, "Exchanging Ohmic Losses in Metamaterial Absorbers with Useful Optical Absorption for Photovoltaics," *Scientific Reports* **4**, 4901 (2014).
- [26] G. Dolling, M. Wegener, C. M. Soukoulis, and S. Linden, "Negative-index metamaterial at 780 nm wavelength," *Optics Letters* **32**(1), 53–55 (2007).
- [27] S. Linden, C. Enkrich, M. Wegener, J. Zhou, T. Koschny, and C. M. Soukoulis, "Magnetic response of metamaterials at 100 terahertz." *Science* **306**(5700), 1351–1353 (2004).
- [28] Z. Fang, L. Fan, C. Lin, D. Zhang, A. J. Meixner, and X. Zhu, "Plasmonic coupling of bow tie antennas with Ag nanowire." *Nano Letters* **11**(4), 1676–1680 (2011).

- [29] H.-T. Chen, "Interference theory of metamaterial perfect absorbers," *Optics Express* **20**(7), 7165–7172 (2012).
- [30] S. Kishore, J. A. Nelson, J. H. Adair, and P. C. Eklund, "Hydrogen storage in spherical and platelet palladium nanoparticles," *Journal of Alloys and Compounds* **389**(1-2), 234–242 (2005).
- [31] J. R. Lacher, "A Theoretical Formula for the Solubility of Hydrogen in Palladium," *Proceedings of the Royal Society A: Mathematical, Physical and Engineering Sciences* **161**(907), 525–545 (1937).
- [32] T. B. Flanagan and W. A. Oates, "The Palladium-Hydrogen System," *Annual Review of Materials Science* **21**, 269–304 (1991).
- [33] C. Langhammer, I. Zorić, B. Kasemo, and B. M. Clemens, "Hydrogen Storage in Pd Nanodisks Characterized with a Novel Nanoplasmonic Sensing Scheme," *Nano Letters* **7**(10), 3122–3127 (2007).
- [34] N. Liu, M. L. Tang, M. Hentschel, H. Giessen, and A. P. Alivisatos, "Nanoantenna-enhanced gas sensing in a single tailored nanofocus." *Nature Materials* **10**(8), 631–636 (2011).
- [35] T. Shegai and C. Langhammer, "Hydride Formation in Single Palladium and Magnesium Nanoparticles Studied By Nanoplasmonic Dark-Field Scattering Spectroscopy," *Advanced Materials* **23**(38), 4409–4414 (2011).
- [36] L. Jewell and B. Davis, "Review of absorption and adsorption in the hydrogen-palladium system," *Applied Catalysis A: General* **310**, 1–15 (2006).
- [37] J. N. Huiberts, R. Griessen, J. H. Rector, R. J. Wijngaarden, J. P. Dekker, D. G. de Groot, and N. J. Koeman, "Yttrium and lanthanum hydride films with switchable optical properties," *Nature* **380**(6), 231–234 (1996).

- [38] R. Griessen, I. A. M. E. Giebels, and B. Dam, *Optical properties of metal-hydrides: switchable mirrors, in Hydrogen as a Future Energy Carrier* (Wiley-VCH Verlag GmbH & Co. KGaA, 2008).
- [39] S. J. van der Molen, J. W. J. Kerssemakers, J. H. Rector, N. J. Koeman, B. Dam, and R. Griessen, "Hydriding kinetics of Pd capped YH_x switchable mirrors," *J Appl Phys* **86**(11), 6107 (1999).
- [40] G. V. Naik, J. Kim, and A. Boltasseva, "Oxides and nitrides as alternative plasmonic materials in the optical range [Invited]," *Optical Materials Express* **1**(6), 1090–1099 (2011).
- [41] S. Law, D. C. Adams, A. M. Taylor, and D. Wasserman, "Mid-infrared designer metals," *Optics Express* **20**(11), 12,155–12,165 (2012).
- [42] S. R. C. Vivekchand, C. J. Engel, S. M. Lubin, M. G. Blaber, W. Zhou, J. Y. Suh, G. C. Schatz, and T. W. Odom, "Liquid Plasmonics: Manipulating Surface Plasmon Polaritons via Phase Transitions," *Nano Letters* **12**(8), 4324–4328 (2012).
- [43] B. F. Soares, F. Jonsson, and N. I. Zheludev, "All-Optical Phase-Change Memory in a Single Gallium Nanoparticle," *Physical Review Letters* **98**, 153,905 (2007).
- [44] M. J. Dicken, K. Aydin, I. M. Pryce, L. A. Sweatlock, E. M. Boyd, S. Walavalkar, J. Ma, and H. A. Atwater, "Frequency tunable near-infrared metamaterials based on VO₂ phase transition." *Optics Express* **17**(20), 18,330–18,339 (2009).
- [45] Z. L. Samson, K. F. MacDonald, F. De Angelis, B. Gholipour, K. Knight, C. C. Huang, E. Di Fabrizio, D. W. Hewak, and N. I. Zheludev, "Metamaterial electro-optic switch of nanoscale thickness," *Applied Physics Letters* **96**(14), 143,105 (2010).
- [46] K. Shportko, S. Kremers, M. Woda, D. Lencer, J. Robertson, and M. Wuttig, "Resonant bonding in crystalline phase-change materials." *Nature Materials* **7**(8), 653–658 (2008).

- [47] A.-K. U. Michel, P. Zalden, D. N. Chigrin, M. Wuttig, A. M. Lindenberg, and T. Taubner, "Reversible Optical Switching of Infrared Antenna Resonances with Ultrathin Phase-Change Layers Using Femtosecond Laser Pulses," *ACS Photonics* **1**(9), 833–839 (2014).
- [48] T. Cao, C. Wei, R. E. Simpson, L. Zhang, and M. J. Cryan, "Rapid phase transition of a phase-change metamaterial perfect absorber," *Optical Materials Express* **3**(8), 1101–1110 (2013).
- [49] R. L. Cotton and J. Siegel, "Stimulated crystallization of melt-quenched $\text{Ge}_2\text{Sb}_2\text{Te}_5$ films employing femtosecond laser double pulses," *Journal of Applied Physics* **112**(1), 3520 (2012).
- [50] K. Sokolowski-Tinten, J. Solis, J. Bialkowski, J. Siegel, C. N. Afonso, and D. von der Linde, "Dynamics of Ultrafast Phase Changes in Amorphous GeSb Films," *Physical Review Letters* **81**(1), 3679–3682 (1998).
- [51] P. Hosseini, C. D. Wright, and H. Bhaskaran, "An optoelectronic framework enabled by low-dimensional phase-change films," *Nature* **511**(7508), 206–211 (2014).
- [52] D. Loke, T. H. Lee, W. J. Wang, L. P. Shi, R. Zhao, Y. C. Yeo, T. C. Chong, and S. R. Elliott, "Breaking the speed limits of phase-change memory." *Science* **336**(6088), 1566–1569 (2012).
- [53] G. Bruns, P. Merkelbach, C. Schlockermann, M. Salinga, M. Wuttig, T. D. Happ, J. B. Philipp, and M. Kund, "Nanosecond switching in GeTe phase change memory cells," *Applied Physics Letters* **95**(4), 043,108 (2009).
- [54] A.-K. U. Michel, D. N. Chigrin, T. W. W. Maß, K. Schöner, M. Salinga, M. Wuttig, and T. Taubner, "Using low-loss phase-change materials for mid-infrared antenna resonance tuning." *Nano Letters* **13**(8), 3470–3475 (2013).

- [55] M. Hu, C. Novo, A. Funston, H. Wang, H. Staleva, S. Zou, P. Mulvaney, Y. Xia, and G. V. Hartland, "Dark-field microscopy studies of single metal nanoparticles: understanding the factors that influence the linewidth of the localized surface plasmon resonance," *Journal of Materials Chemistry* **18**(17), 1949 (2008).
- [56] C. Sönnichsen, T. Franzl, T. Wilk, G. von Plessen, and J. Feldmann, "Drastic Reduction of Plasmon Damping in Gold Nanorods," *Physical Review Letters* **88**(7), 077402 (2002).
- [57] N. J. Halas, S. Lal, W.-S. Chang, S. Link, and P. Nordlander, "Plasmons in Strongly Coupled Metallic Nanostructures," *Chemical Reviews* **111**(6), 3913–3961 (2011).
- [58] J. Liu, Y. Sun, and X. Fan, "Highly versatile fiber-based optical Fabry-Pérot gas sensor." *Optics Express* **17**(4), 2731–2738 (2009).
- [59] P. Tassin, L. Zhang, R. Zhao, A. Jain, T. Koschny, and C. Soukoulis, "Electromagnetically Induced Transparency and Absorption in Metamaterials: The Radiating Two-Oscillator Model and Its Experimental Confirmation," *Physical Review Letters* **109**(18), 187401 (2012).
- [60] A. Miroshnichenko, S. Flach, and Y. Kivshar, "Fano resonances in nanoscale structures," *Reviews of Modern Physics* **82**(3), 2257–2298 (2010).
- [61] L. Novotny and N. van Hulst, "Antennas for light," *Nature Photonics* **5**(2), 83–90 (2011).
- [62] P. Muhschlegel, H.-J. Eisler, O. J. F. Martin, B. Hecht, and D. W. Pohl, "Resonant optical antennas." *Science* **308**(5728), 1607–1609 (2005).
- [63] J. Zuloaga, E. Prodan, and P. Nordlander, "Quantum Plasmonics: Optical Properties and Tunability of Metallic Nanorods," *ACS Nano* **4**(9), 5269–5276 (2010).

- [64] K. J. Savage, M. M. Hawkeye, R. Esteban, A. G. Borisov, J. Aizpurua, and J. J. Baumberg, "Revealing the quantum regime in tunnelling plasmonics," *Nature* **491**(7425), 574–577 (2013).
- [65] J. A. Scholl, A. García-Etxarri, A. L. Koh, and J. A. Dionne, "Observation of Quantum Tunneling between Two Plasmonic Nanoparticles," *Nano Letters* pp. 564–569 (2013).
- [66] E. M. Larsson, C. Langhammer, I. Zoric, and B. Kasemo, "Nanoplasmonic Probes of Catalytic Reactions," *Science* **326**(5956), 1091–1094 (2009).
- [67] G. Korotcenkov, "Gas response control through structural and chemical modification of metal oxide films: state of the art and approaches," *Sensors & Actuators: B. Chemical* **107**(1), 209–232 (2005).
- [68] G. Eranna, B. C. Joshi, D. P. Runthala, and R. P. Gupta, "Oxide Materials for Development of Integrated Gas Sensors—A Comprehensive Review," *Critical Reviews in Solid State and Materials Sciences* **29**(3-4), 111–188 (2004).
- [69] M. Ando, T. Kobayashi, S. Iijima, and M. Haruta, "Optical CO sensitivity of Au-CuO composite film by use of the plasmon absorption change," *Sensors & Actuators: B. Chemical* **96**(3), 589–595 (2003).
- [70] G. Sirinakis, R. Siddique, I. Manning, P. H. Rogers, and M. A. Carpenter, "Development and Characterization of Au-YSZ Surface Plasmon Resonance Based Sensing Materials: High Temperature Detection of CO," *The Journal of Physical Chemistry B* **110**(27), 13,508–13,511 (2006).
- [71] W. J. Buttner, M. B. Post, R. Burgess, and C. Rivkin, "An overview of hydrogen safety sensors and requirements," *International Journal of Hydrogen Energy* **36**(3), 2462–2470 (2011).
- [72] S. Linic, P. Christopher, and D. B. Ingram, "Plasmonic-metal nanostructures for efficient conversion of solar to chemical energy." *Nature Materials* **10**(12), 911–921 (2011).

- [73] D. Buso, G. Busato, M. Guglielmi, A. Martucci, V. Bello, G. Mattei, P. Mazzoldi, and M. L. Post, "Selective optical detection of H₂ and CO with SiO₂ sol-gel films containing NiO and Au nanoparticles," *Nanotechnology* **18**(47), 475,505 (2007).
- [74] G. Dharmalingam, N. A. Joy, B. Grisafe, and M. A. Carpenter, "Plasmonics-based detection of H₂ and CO: discrimination between reducing gases facilitated by material control," *Beilstein Journal of Nanotechnology* **3**, 712–721 (2012).
- [75] P. H. Rogers, G. Sirinakis, and M. A. Carpenter, "Direct Observations of Electrochemical Reactions within Au-YSZ Thin Films via Absorption Shifts in the Au Nanoparticle Surface Plasmon Resonance," *Journal of Physical Chemistry C* **112**(17), 6749–6757 (2008).
- [76] P. R. Ohodnicki, C. Wang, S. Natesakhawat, J. P. Baltrus, and T. D. Brown, "In-situ and ex-situ characterization of TiO₂ and Au nanoparticle incorporated TiO₂ thin films for optical gas sensing at extreme temperatures," *Journal of Applied Physics* **111**(6), 064,320 (2012).
- [77] E. Della Gaspera, M. Guglielmi, S. Agnoli, G. Granozzi, M. L. Post, V. Bello, G. Mattei, and A. Martucci, "Au Nanoparticles in Nanocrystalline TiO₂-NiO Films for SPR-Based, Selective H₂S Gas Sensing," *Chemistry of Materials* **22**(11), 3407–3417 (2010).
- [78] P. H. Rogers, G. Sirinakis, and M. A. Carpenter, "Plasmonic-based Detection of NO₂ in a Harsh Environment," *Journal of Physical Chemistry C* **112**(24), 8784–8790 (2008).
- [79] H. Jans and Q. Huo, "Gold nanoparticle-enabled biological and chemical detection and analysis," *Chemical Society Reviews* **41**(7), 2849–2866 (2012).
- [80] J. Yang, J. Yang, and J. Y. Ying, "Morphology and Lateral Strain Control of Pt Nanoparticles via Core-Shell Construction Using Alloy AgPd Core Toward Oxygen Reduction Reaction," *ACS Nano* pp. 9373–9382 (2012).

- [81] M. L. Christian and K.-F. Aguey-Zinsou, "Core-Shell Strategy Leading to High Reversible Hydrogen Storage Capacity for NaBH_4 ," *ACS Nano* pp. 7739–7751 (2012).
- [82] Y.-C. Hsieh, Y. Zhang, D. Su, V. Volkov, R. Si, L. Wu, Y. Zhu, W. An, P. Liu, P. He, S. Ye, R. R. Adzic, and J. X. Wang, "Ordered bilayer ruthenium–platinum core-shell nanoparticles as carbon monoxide-tolerant fuel cell catalysts," *Nature Communications* **4**, 2466 (2013).
- [83] T. Ghodselahi, H. Zahrabi, M. H. Saani, and M. A. Vesaghi, "CO Gas Sensor Properties of Cu@CuO Core-Shell Nanoparticles Based on Localized Surface Plasmon Resonance," *The Journal of Physical Chemistry C* **115**(45), 22,126–22,130 (2011).
- [84] P. Vasileva, B. Donkova, I. Karadjova, and C. Dushkin, "Synthesis of starch-stabilized silver nanoparticles and their application as a surface plasmon resonance-based sensor of hydrogen peroxide," *Colloids and Surfaces A: Physicochemical and Engineering Aspects* **382**(1-3), 203–210 (2011).
- [85] B. Halliwell, M. V. Clement, and L. H. Long, "Hydrogen peroxide in the human body," *FEBS Letters* **486**(1), 10–13 (2000).
- [86] T. Endo, A. Shibata, Y. Yanagida, Y. Higo, and T. Hatsuzawa, "Localized surface plasmon resonance optical characteristics for hydrogen peroxide using polyvinylpyrrolidone coated silver nanoparticles," *Materials Letters* **64**(19), 2105–2108 (2010).
- [87] R. T. Hill, J. J. Mock, A. Hucknall, S. D. Wolter, N. M. Jokerst, D. R. Smith, and A. Chilkoti, "Plasmon ruler with angstrom length resolution." *ACS Nano* **6**(10), 9237–9246 (2012).
- [88] C. Ciraci, R. T. Hill, J. J. Mock, Y. Urzhumov, A. I. Fernández-Domínguez, S. A. Maier, J. B. Pendry, A. Chilkoti, and D. R. Smith, "Probing the ultimate limits

- of plasmonic enhancement," *Science* **337**(6098), 1072–1074 (2012).
- [89] M. Yamauchi, R. Ikeda, H. Kitagawa, and M. Takata, "Nanosize Effects on Hydrogen Storage in Palladium," *The Journal of Physical Chemistry C* **112**(9), 3294–3299 (2008).
- [90] M. Khanuja, D. Varandani, and B. R. Mehta, "Pulse like hydrogen sensing response in Pd nanoparticle layers," *Applied Physics Letters* **91**(25), 253,121 (2007).
- [91] M. L. Tang, N. Liu, J. A. Dionne, and A. P. Alivisatos, "Observations of Shape-Dependent Hydrogen Uptake Trajectories from Single Nanocrystals," *Journal of the American Chemical Society* **133**(34), 13,220–13,223 (2011).
- [92] D. Seo, G. Park, and H. Song, "Plasmonic Monitoring of Catalytic Hydrogen Generation by a Single Nanoparticle Probe," *Journal of the American Chemical Society* **134**(2), 1221–1227 (2012).
- [93] A. Tittl, X. Yin, H. Giessen, X.-D. Tian, Z. Q. Tian, C. Krimers, D. N. Chigrin, and N. Liu, "Plasmonic Smart Dust for Probing Local Chemical Reactions," *Nano Letters* **13**(4), 1816–1821 (2013).
- [94] C. Wang, L. Ma, M. Hossain, H. Wang, S. Zou, J. J. Hickman, and M. Su, "Direct visualization of molecular scale chemical adsorptions on solids using plasmonic nanoparticle arrays," *Sensors & Actuators: B. Chemical* **150**(2), 667–672 (2010).
- [95] T. Morris and G. Szulczewski, "A Spectroscopic Ellipsometry, Surface Plasmon Resonance, and X-ray Photoelectron Spectroscopy Study of Hg Adsorption on Gold Surfaces," *Langmuir* **18**(6), 2260–2264 (2002).
- [96] S. Ahmadnia-Feyzabad, A. A. Khodadadi, M. Vesali-Naseh, and Y. Mortazavi, "Highly sensitive and selective sensors to volatile organic compounds using MWCNTs/SnO₂," *Sensors & Actuators: B. Chemical* **166-167**, 150–155 (2012).

- [97] L. I. B. Silva, A. C. Freitas, T. A. P. Rocha-Santos, M. E. Pereira, and A. C. Duarte, "Breath analysis by optical fiber sensor for the determination of exhaled organic compounds with a view to diagnostics." *Talanta* **83**(5), 1586–1594 (2011).
- [98] W. Ma, J. Luo, W. Ling, and W. Wang, "Chloroform-sensing properties of plasmonic nanostructures using poly(methyl methacrylate) transduction layer," *Micro & Nano Letters* **8**(2), 111–114 (2013).
- [99] N. Strohsfeldt, A. Tittl, and H. Giessen, "Long-term stability of capped and buffered palladium-nickel thin films and nanostructures for plasmonic hydrogen sensing applications," *Optical Materials Express* **3**(2), 194–204 (2013).
- [100] E. Prodan, P. Nordlander, and N. J. Halas, "Effects of dielectric screening on the optical properties of metallic nanoshells," *Chemical Physics Letters* **368**, 94–101 (2003).
- [101] M. Hentschel, D. Dregely, R. Vogelgesang, H. Giessen, and N. Liu, "Plasmonic Oligomers: The Role of Individual Particles in Collective Behavior," *ACS Nano* **5**(3), 2042–2050 (2011).
- [102] M. Rahmani, D. Y. Lei, V. Giannini, B. Lukiyanchuk, M. Ranjbar, T. Y. F. Liew, M. Hong, and S. A. Maier, "Subgroup Decomposition of Plasmonic Resonances in Hybrid Oligomers: Modeling the Resonance Lineshape," *Nano Letters* **12**(4), 2101–2106 (2012).
- [103] G. Schider, J. R. Krenn, W. Gotschy, B. Lamprecht, H. Ditlbacher, A. Leitner, and F. R. Aussenegg, "Optical properties of Ag and Au nanowire gratings," *Journal of Applied Physics* **90**(8), 3825 (2001).
- [104] S. Tikhodeev, A. L. Yablonskii, E. A. Muljarov, N. A. Gippius, and T. Ishihara, "Quasiguide modes and optical properties of photonic crystal slabs," *Physical Review B* **66**(4), 045,102 (2002).

- [105] S. Fan and J. Joannopoulos, "Analysis of guided resonances in photonic crystal slabs," *Physical Review B* **65**(23), 235,112 (2002).
- [106] A. Christ, S. Tikhodeev, N. Gippius, J. Kuhl, and H. Giessen, "Waveguide-Plasmon Polaritons: Strong Coupling of Photonic and Electronic Resonances in a Metallic Photonic Crystal Slab," *Physical Review Letters* **91**(18), 183,901 (2003).
- [107] D. Nau, A. Seidel, R. B. Orzekowsky, S. H. Lee, S. Deb, and H. Giessen, "Hydrogen sensor based on metallic photonic crystal slabs," *Optics Letters* **35**(18), 3150–3152 (2010).
- [108] C. Valsecchi and A. G. Brolo, "Periodic Metallic Nanostructures as Plasmonic Chemical Sensors," *Langmuir* **29**(19), 5638–5649 (2013).
- [109] A. G. Brolo, R. Gordon, B. Leathem, and K. L. Kavanagh, "Surface Plasmon Sensor Based on the Enhanced Light Transmission through Arrays of Nanoholes in Gold Films," *Langmuir* **20**(12), 4813–4815 (2004).
- [110] T. W. Ebbesen, H. J. Lezec, H. F. Ghaemi, T. Thio, and P. A. Wolff, "Extraordinary optical transmission through sub-wavelength hole arrays," *Nature* **391**(6668), 667–669 (1998).
- [111] E. Maeda, S. Mikuriya, K. Endo, I. Yamada, A. Suda, and J.-J. Delaunay, "Optical hydrogen detection with periodic subwavelength palladium hole arrays," *Applied Physics Letters* **95**(13), 133,504 (2009).
- [112] P. Fedtke, M. Wienecke, M.-C. Bunescu, M. Pietrzak, K. Deistung, and E. Borchardt, "Hydrogen sensor based on optical and electrical switching," *Sensors & Actuators: B. Chemical* **100**(1-2), 151–157 (2004).
- [113] A. Kinkhabwala, Z. Yu, S. Fan, Y. Avlasevich, K. Müllen, and W. E. Moerner, "Large single-molecule fluorescence enhancements produced by a bowtie nanoantenna," *Nature Photonics* **3**(11), 654–657 (2009).

- [114] H. Duan, A. I. Fernández-Domínguez, M. Bosman, S. A. Maier, and J. K. W. Yang, "Nanoplasmonics: Classical down to the Nanometer Scale," *Nano Letters* **12**(3), 1683–1689 (2012).
- [115] M. W. Knight, H. Sobhani, P. Nordlander, and N. J. Halas, "Photodetection with Active Optical Antennas," *Science* **332**(6030), 702–704 (2011).
- [116] Y. Zhao, N. Engheta, and A. Alù, "Effects of shape and loading of optical nanoantennas on their sensitivity and radiation properties," *Journal of the Optical Society of America B* **28**(5), 1266 (2011).
- [117] N. Liu, F. Wen, Y. Zhao, Y. Wang, P. Nordlander, N. J. Halas, and A. Alù, "Individual Nanoantennas Loaded by Three-dimensional Optical Nanocircuits," *Nano Letters* **13**(1), 142–147 (2012).
- [118] A. Tittl, C. Kremers, J. Dorfmüller, D. N. Chigrin, and H. Giessen, "Spectral shifts in optical nanoantenna-enhanced hydrogen sensors," *Optical Materials Express* **2**(2), 111–118 (2012).
- [119] C. Wadell, T. J. Antosiewicz, and C. Langhammer, "Optical Absorption Engineering in Stacked Plasmonic Au-SiO₂-Pd Nanoantennas." *Nano Letters* **12**, 4784–4790 (2012).
- [120] A. Dasgupta and G. V. P. Kumar, "Palladium bridged gold nanocylinder dimer: plasmonic properties and hydrogen sensitivity," *Appl Opt* **51**(11), 1688–1693 (2012).
- [121] M. A. Poyli, V. M. Silkin, I. P. Chernov, P. M. Echenique, R. D. Muiño, and J. Aizpurua, "Multiscale Theoretical Modeling of Plasmonic Sensing of Hydrogen Uptake in Palladium Nanodisks," *The Journal of Physical Chemistry Letters* **3**(18), 2556–2561 (2012).
- [122] M. E. Stewart, C. R. Anderton, L. B. Thompson, J. Maria, S. K. Gray, J. A. Rogers, and R. G. Nuzzo, "Nanostructured Plasmonic Sensors," *Chemical Reviews* **108**(2), 494–521 (2008).

- [123] C. Drake, S. Deshpande, D. Bera, and S. Seal, "Metallic nanostructured materials based sensors," *International Materials Reviews* **52**(5), 289–317 (2007).
- [124] F. Neubrech, A. Pucci, T. Cornelius, S. Karim, A. García-Etxarri, and J. Aizpurua, "Resonant Plasmonic and Vibrational Coupling in a Tailored Nanoantenna for Infrared Detection," *Physical Review Letters* **101**(15), 157403 (2008).
- [125] J. Dorfmueller, R. Vogelgesang, W. Khunsin, C. Rockstuhl, C. Etrich, and K. Kern, "Plasmonic Nanowire Antennas: Experiment, Simulation, and Theory," *Nano Letters* **10**(9), 3596–3603 (2010).
- [126] T. Schumacher, K. Kratzer, D. Molnar, M. Hentschel, H. Giessen, and M. Lippitz, "Nanoantenna-enhanced ultrafast nonlinear spectroscopy of a single gold nanoparticle," *Nature Communications* **2**, 333 (2011).
- [127] W. E. Vargas, I. Rojas, D. E. Azofeifa, and N. Clark, "Optical and electrical properties of hydrided palladium thin films studied by an inversion approach from transmittance measurements," *Thin Solid Films* **496**(2), 189–196 (2006).
- [128] A. Tittl, H. Giessen, and N. Liu, "Plasmonic gas and chemical sensing," *Nanophotonics* **3**(3), 157–180 (2014).
- [129] J. I. Avila, R. J. Matelon, R. Trabol, M. Favre, D. Lederman, U. G. Volkmann, and A. L. Cabrera, "Optical properties of Pd thin films exposed to hydrogen studied by transmittance and reflectance spectroscopy," *Journal of Applied Physics* **107**(2), 023,504 (2010).
- [130] F. Yang, S.-C. Kung, M. Cheng, J. C. Hemminger, and R. M. Penner, "Smaller is Faster and More Sensitive: The Effect of Wire Size on the Detection of Hydrogen by Single Palladium Nanowires," *ACS Nano* **4**(9), 5233–5244 (2010).
- [131] O. L. Muskens, V. Giannini, J. A. Sánchez-Gil, and J. Gómez Rivas, "Strong Enhancement of the Radiative Decay Rate of Emitters by Single Plasmonic Nanoantennas," *Nano Letters* **7**(9), 2871–2875 (2007).

- [132] P. B. Johnson and R. W. Christy, "Optical-Constants of Noble-Metals," *Physical Review B* **6**(12), 4370–4379 (1972).
- [133] J. Becker, A. Trügler, A. Jakab, U. Hohenester, and C. Sönnichsen, "The Optimal Aspect Ratio of Gold Nanorods for Plasmonic Bio-sensing," *Plasmonics* **5**(2), 161–167 (2010).
- [134] T. Mitsui, M. K. Rose, E. Fomin, D. F. Ogletree, and M. Salmeron, "Dissociative hydrogen adsorption on palladium requires aggregates of three or more vacancies." *Nature* **422**(6933), 705–707 (2003).
- [135] E. M. van Schrojenstein Lantman, T. Deckert-Gaudig, A. J. G. Mank, V. Deckert, and B. M. Weckhuysen, "Catalytic processes monitored at the nanoscale with tip-enhanced Raman spectroscopy," *Nature Nanotechnology* **7**(9), 583–586 (2012).
- [136] H. Kim, K. M. Kosuda, R. P. Van Duyne, and P. C. Stair, "Resonance Raman and surface- and tip-enhanced Raman spectroscopy methods to study solid catalysts and heterogeneous catalytic reactions." *Chemical Society Reviews* **39**(12), 4820–4844 (2010).
- [137] N. Jiang, E. T. Foley, J. M. Klingsporn, M. D. Sonntag, N. A. Valley, J. A. Dieringer, T. Seideman, G. C. Schatz, M. C. Hersam, and R. P. Van Duyne, "Observation of Multiple Vibrational Modes in Ultrahigh Vacuum Tip-Enhanced Raman Spectroscopy Combined with Molecular-Resolution Scanning Tunneling Microscopy," *Nano Letters* **12**(10), 5061–5067 (2012).
- [138] M. D. Sonntag, J. M. Klingsporn, L. K. Garibay, J. M. Roberts, J. A. Dieringer, T. Seideman, K. A. Scheidt, L. Jensen, G. C. Schatz, and R. P. Van Duyne, "Single-Molecule Tip-Enhanced Raman Spectroscopy," *The Journal of Physical Chemistry C* **116**(1), 478–483 (2012).
- [139] B. Pettinger, B. Ren, G. Picardi, R. Schuster, and G. Ertl, "Nanoscale Probing of Adsorbed Species by Tip-Enhanced

- Raman Spectroscopy," *Physical Review Letters* **92**(9), 96,101 (2004).
- [140] D.-Y. Wu, J. F. Li, B. Ren, and Z. Q. Tian, "Electrochemical surface-enhanced Raman spectroscopy of nanostructures." *Chemical Society Reviews* **37**(5), 1025–1041 (2008).
- [141] S. Chen, M. Svedendahl, R. P. V. Duyne, and M. Käll, "Plasmon-Enhanced Colorimetric ELISA with Single Molecule Sensitivity," *Nano Letters* **11**(4), 1826–1830 (2011).
- [142] Z. Liu, W. Hou, P. Pavaskar, M. Aykol, and S. B. Cronin, "Plasmon resonant enhancement of photocatalytic water splitting under visible illumination." *Nano Letters* **11**(3), 1111–1116 (2011).
- [143] J. F. Li, Y. F. Huang, Y. Ding, Z. L. Yang, S. B. Li, X. S. Zhou, F. R. Fan, W. Zhang, Z. Y. Zhou, D. Y. Wu, B. Ren, Z. L. Wang, and Z. Q. Tian, "Shell-isolated nanoparticle-enhanced Raman spectroscopy," *Nature* **464**(7287), 392–395 (2010).
- [144] C. Langhammer, V. P. Zhdanov, I. Zorić, and B. Kasemo, "Size-Dependent Kinetics of Hydriding and Dehydriding of Pd Nanoparticles," *Physical Review Letters* **104**(13), 135,502 (2010).
- [145] A. B. Dahlin, J. O. Tegenfeldt, and F. Höök, "Improving the instrumental resolution of sensors based on localized surface plasmon resonance." *Analytical Chemistry* **78**(13), 4416–4423 (2006).
- [146] B. Efron, "Bootstrap methods: another look at the jackknife," *The Annals of Statistics* **7**(1), 1–26 (1979).
- [147] B. Efron, "Nonparametric estimates of standard error: the jackknife, the bootstrap and other methods," *Biometrika* **68**(3), 589–599 (1981).
- [148] N. Liu, H. Guo, L. Fu, S. Kaiser, H. Schweizer, and H. Giessen, "Plasmon Hybridization in Stacked Cut-Wire

- Metamaterials," *Advanced Materials* **19**(21), 3628–3632 (2007).
- [149] X. Shan, I. Díez-Pérez, L. Wang, P. Wiktor, Y. Gu, L. Zhang, W. Wang, J. Lu, S. Wang, Q. Gong, J. Li, and N. Tao, "Imagining the electrocatalytic activity of single nanoparticles," *Nature Nanotechnology* **7**(1), 668–672 (2012).
- [150] J. Zhang, M. B. Vukmirovic, Y. Xu, M. Mavrikakis, and R. R. Adzic, "Controlling the catalytic activity of platinum-monolayer electrocatalysts for oxygen reduction with different substrates," *Angewandte Chemie International Edition* **44**(14), 2132–2135 (2005).
- [151] S. Park, J. Vohs, and R. Gorte, "Direct oxidation of hydrocarbons in a solid-oxide fuel cell," *Nature* **404**(6775), 265–267 (2000).
- [152] Z. Zou, J. Ye, K. Sayama, and H. Arakawa, "Direct splitting of water under visible light irradiation with an oxide semiconductor photocatalyst," *Nature* **414**(6), 625–627 (2001).
- [153] X. Ye, C. Zheng, J. Chen, Y. Gao, and C. B. Murray, "Using Binary Surfactant Mixtures To Simultaneously Improve the Dimensional Tunability and Monodispersity in the Seeded Growth of Gold Nanorods," *Nano Letters* **13**(2), 765–771 (2013).
- [154] J. Burdick, R. Laocharoensuk, P. M. Wheat, J. D. Posner, and J. Wang, "Synthetic Nanomotors in Microchannel Networks: Directional Microchip Motion and Controlled Manipulation of Cargo," *Journal of the American Chemical Society* **130**(26), 8164–8165 (2008).
- [155] C. Sönnichsen, B. M. Reinhard, J. Liphardt, and A. P. Alivisatos, "A molecular ruler based on plasmon coupling of single gold and silver nanoparticles," *Nature Biotechnology* **23**(6), 741–745 (2005).
- [156] B. Nikoobakht and M. A. El-Sayed, "Preparation and Growth Mechanism of Gold Nanorods (NRs) Using Seed-

- Mediated Growth Method," *Chemistry of Materials* **15**(10), 1957–1962 (2003).
- [157] B. Xiong, R. Zhou, J. Hao, Y. Jia, Y. He, and E. S. Yeung, "Highly sensitive sulphide mapping in live cells by kinetic spectral analysis of single Au-Ag core-shell nanoparticles," *Nature Communications* **4**, 1708 (2013).
- [158] W. Gao, A. Pei, and J. Wang, "Water-Driven Micromotors," *ACS Nano* **6**(9), 8432–8438 (2012).
- [159] L. Qin, S. Park, L. Huang, and C. A. Mirkin, "On-wire lithography." *Science* **309**(5731), 113–115 (2005).
- [160] Z. Deng and C. Mao, "DNA-Templated Fabrication of 1D Parallel and 2D Crossed Metallic Nanowire Arrays," *Nano Letters* **3**, 1545–1548 (2003).
- [161] Y. Hatakeyama, M. Umetsu, S. Ohara, F. Kawadai, S. Takami, T. Naka, and T. Adschiri, "Homogenous Spherical Mosslike Assembly of Pd Nanoparticles by using DNA Compaction: Application of Pd–DNA Hybrid Materials to Volume-Expansion Hydrogen Switches," *Advanced Materials* **20**(6), 1122–1128 (2008).
- [162] L. A. Stearns, R. Chhabra, J. Sharma, Y. Liu, W. T. Petuskey, H. Yan, and J. C. Chaput, "Template-Directed Nucleation and Growth of Inorganic Nanoparticles on DNA Scaffolds," *Angewandte Chemie International Edition* **121**(45), 8646–8648 (2009).
- [163] S. Pal, R. Varghese, Z. Deng, Z. Zhao, A. Kumar, H. Yan, and Y. Liu, "Site-Specific Synthesis and In Situ Immobilization of Fluorescent Silver Nanoclusters on DNA Nanoscaffolds by Use of the Tollens Reaction," *Angewandte Chemie International Edition* **50**(18), 4176–4179 (2011).
- [164] R. Schreiber, S. Kempter, S. Holler, V. Schüller, D. Schiffels, S. S. Simmel, P. C. Nickels, and T. Liedl, "DNA origami-templated growth of arbitrarily shaped metal nanoparticles." *Small (Weinheim an der Bergstrasse, Germany)* **7**(13), 1795–1799 (2011).

- [165] Y. Geng, A. C. Pearson, E. P. Gates, B. Uprety, R. C. Davis, J. N. Harb, and A. T. Woolley, "Electrically Conductive Gold- and Copper-Metallized DNA Origami Nanostructures," *Langmuir* **29**(10), 3482–3490 (2013).
- [166] J. Hao, J. Wang, X. Liu, W. J. Padilla, L. Zhou, and M. Qiu, "High performance optical absorber based on a plasmonic metamaterial," *Applied Physics Letters* **96**(25), 251,104 (2010).
- [167] C. Hu, Z. Zhao, X. Chen, and X. Luo, "Realizing near-perfect absorption at visible frequencies." *Optics Express* **17**(13), 11,039–11,044 (2009).
- [168] M. Khanuja, B. R. Mehta, P. Agar, P. K. Kulriya, and D. K. Avasthi, "Hydrogen induced lattice expansion and crystallinity degradation in palladium nanoparticles: Effect of hydrogen concentration, pressure, and temperature," *Journal of Applied Physics* **106**(9), 093,515 (2009).
- [169] C. Hyeonsik, Y. S. Jae, D. L. Jae, M. J. Jung, and L. So-Hee, "Comparison of Pd, Pt and Pt/Pd as Catalysts for Hydrogen Sensor Films," *J Korean Phys Soc* **55**(61), 2693–2696 (2009).
- [170] T. Weiss, G. Granet, N. A. Gippius, S. Tikhodeev, and H. Giessen, "Matched coordinates and adaptive spatial resolution in the Fourier modal method." *Optics Express* **17**(10), 8051–8061 (2009).
- [171] H. C. Guo, D. Nau, A. Radke, X. P. Zhang, J. Stodolka, X. L. Yang, S. Tikhodeev, N. A. Gippius, and H. Giessen, "Large-area metallic photonic crystal fabrication with interference lithography and dry etching," *Applied Physics B: Lasers and Optics* **81**(2-3), 271–275 (2005).
- [172] J. W. Goodman, *Introduction to Fourier optics* (Roberts & Co Publishers, 2005).
- [173] M. G. Harats, N. Livneh, G. Zaiats, S. Yochelis, Y. Paltiel, E. Lifshitz, and R. Rapaport, "Full Spectral and Angular Characterization of Highly Directional Emission from

- Nanocrystal Quantum Dots Positioned on Circular Plasmonic Lenses," *Nano Letters* **14**(10), 5766–5771 (2014).
- [174] T. Weiss, N. A. Gippius, S. Tikhodeev, G. Granet, and H. Giessen, "Efficient calculation of the optical properties of stacked metamaterials with a Fourier modal method," *Journal of Optics A: Pure and Applied Optics* **11**(11), 114,019 (2009).
- [175] A. Polyakov, M. Zolotarev, P. J. Schuck, and H. A. Padmore, "Collective behavior of impedance matched plasmonic nanocavities," *Optics Express* **20**(7), 7685–7693 (2012).
- [176] F. Falco, T. Tamir, and K. M. Leung, "Grating diffraction and Wood's anomalies at two-dimensionally periodic impedance surfaces," *JOSA A* **21**(9), 1621–1634 (2004).
- [177] A. H. A. A. Oliner, "A New Theory of Wood's Anomalies on Optical Gratings," *Appl Opt* **4**(10), 1275–1297 (1965).
- [178] A. Tittl, M. G. Harats, R. Walter, X. Yin, M. Schäferling, N. Liu, R. Rapaport, and H. Giessen, "Quantitative angle-resolved small-spot reflectance measurements on plasmonic perfect absorbers: impedance matching and disorder effects." *ACS Nano* **8**(10), 10,885–10,892 (2014).
- [179] R. Walter, A. Tittl, A. Berrier, F. Sterl, T. Weiss, and H. Giessen, "Large-Area Low-Cost Tunable Plasmonic Perfect Absorber in the Near Infrared by Colloidal Etching Lithography," *Advanced Optical Materials* (2015).
- [180] K. H. Su, Q. H. Wei, X. Zhang, J. J. Mock, D. R. Smith, and S. Schultz, "Interparticle Coupling Effects on Plasmon Resonances of Nanogold Particles," *Nano Letters* **3**(8), 1087–1090 (2003).
- [181] M. Quinten and U. Kreibig, "Absorption and elastic scattering of light by particle aggregates." *Appl Opt* **32**(30), 6173–6182 (1993).
- [182] D. Nau, A. Schönhardt, C. Bauer, A. Christ, T. Zentgraf, J. Kuhl, M. Klein, and H. Giessen, "Correlation Effects in

- Disordered Metallic Photonic Crystal Slabs," *Physical Review Letters* **98**(13), 133,902 (2007).
- [183] M. A. Kats, D. Sharma, J. Lin, P. Genevet, R. Blanchard, Z. Yang, M. M. Qazilbash, D. N. Basov, S. Ramanathan, and F. Capasso, "Ultra-thin perfect absorber employing a tunable phase change material," *Applied Physics Letters* **101**(22), 221,101 (2012).
- [184] Z. L. Sámson, S.-C. Yen, K. F. MacDonald, K. Knight, S. Li, D. W. Hewak, D. P. Tsai, and N. I. Zheludev, "Chalcogenide glasses in active plasmonics," *physica status solidi (RRL) - Rapid Research Letters* **4**(10), 274–276 (2010).
- [185] A. L. Stepanov, G. Bour, A. Reinholdt, and U. Kreibig, "The formation of hydrogenated yttrium nanoparticles," *Technical Physics Letters* **28**(8), 642–644 (2002).
- [186] N. Strohfeldt, A. Tittl, M. Schäferling, F. Neubrech, U. Kreibig, R. Griessen, and H. Giessen, "Yttrium hydride nanoantennas for active plasmonics." *Nano Letters* **14**(3), 1140–1147 (2014).
- [187] A. T. M. Van Gogh, D. Nagengast, E. Kooij, N. Koeman, J. Rector, R. Griessen, C. Flipse, and R. Smeets, "Structural, electrical, and optical properties of $\text{La}_{1-z}\text{YzH}_x$ switchable mirrors," *Physical Review B* **63**(19), 195,105 (2001).
- [188] M. Gartz and M. Quinten, "Broadening of resonances in yttrium nanoparticle optical spectra," *Applied Physics B: Lasers and Optics* **73**(4), 327–332 (2001).
- [189] A. F. T. Hoekstra, A. S. Roy, and T. F. Rosenbaum, "Scaling at the Mott–Hubbard metal–insulator transition in yttrium hydride," *Journal of Physics: Condensed Matter* **15**(9), 1405 (2003).
- [190] S. Law, V. Podolskiy, and D. Wasserman, "Towards nano-scale photonics with micro-scale photons: the opportunities and challenges of mid-infrared plasmonics," *Nanophotonics* **2**(2), 103–130 (2013).

- [191] J. J. Talghader, A. S. Gawarikar, and R. P. Shea, "Spectral selectivity in infrared thermal detection," *Light: Science & Applications* **1**(8), e24 (2012).
- [192] C. D. Tran, "Infrared Multispectral Imaging: Principles and Instrumentation," *Applied Spectroscopy Reviews* **38**(2), 133–153 (2003).
- [193] T. Schimert, C. Hanson, J. Brady, T. Fagan, M. Taylor, W. McCardel, R. Gooch, M. Gohlke, and A. J. Syllaios, "Advances in small-pixel, large-format α -Si bolometer arrays," *Proceedings of the SPIE* **7298**, 72,980T–72,980T–5 (2009).
- [194] F. Niklaus, C. Vieider, and H. Jakobsen, "MEMS-based uncooled infrared bolometer arrays: a review," *Proceedings of the SPIE* **6836**, 68,360D–68,360D–15 (2008).
- [195] T. Cao, C.-w. Wei, R. E. Simpson, L. Zhang, and M. J. Cryan, "Broadband Polarization-Independent Perfect Absorber Using a Phase-Change Metamaterial at Visible Frequencies," *Scientific Reports* **4**, 3955 (2014).
- [196] T. Cao, L. Zhang, R. E. Simpson, and M. J. Cryan, "Mid-infrared tunable polarization-independent perfect absorber using a phase-change metamaterial," *JOSA B* **30**(6), 1580–1585 (2013).
- [197] M. A. Kats, R. Blanchard, S. Zhang, P. Genevet, C. Ko, S. Ramathanan, and F. Capasso, "Vanadium Dioxide as a Natural Disordered Metamaterial: Perfect Thermal Emission and Large Broadband Negative Differential Thermal Emission," *Physical Review X* **3**(4), 041,004 (2013).
- [198] T. Siegrist, P. Jost, H. Volker, M. Woda, P. Merkelbach, C. Schlockermann, and M. Wuttig, "Disorder-induced localization in crystalline phase-change materials." *Nature Materials* **10**(3), 202–208 (2011).
- [199] M. Wuttig and N. Yamada, "Phase-change materials for rewriteable data storage," *Nature Materials* **6**(11), 824–832 (2007).

- [200] T. Tsafack, E. Piccinini, B.-S. Lee, E. Pop, and M. Rudan, "Electronic, optical and thermal properties of the hexagonal and rocksalt-like $\text{Ge}_2\text{Sb}_2\text{Te}_5$ chalcogenide from first-principle calculations," *Journal of Applied Physics* **110**(6), 063,716 (2011).
- [201] D. Y. Lei, K. Appavoo, Y. Sonnefraud, R. F. Haglund, and S. A. Maier, "Single-particle plasmon resonance spectroscopy of phase transition in vanadium dioxide." *Optics Letters* **35**(23), 3988–3990 (2010).
- [202] B. Gholipour, J. Zhang, K. F. MacDonald, D. W. Hewak, and N. I. Zheludev, "An All-Optical, Non-volatile, Bidirectional, Phase-Change Meta-Switch," *Advanced Materials* **25**(22), 3050–3054 (2013).
- [203] T. Maier and H. Brueckl, "Multispectral microbolometers for the midinfrared," *Optics Letters* **35**(22), 3766–3768 (2010).
- [204] T. Maier and H. Brueckl, "Wavelength-tunable microbolometers with metamaterial absorbers," *Optics Letters* **34**(19), 3012–3014 (2009).
- [205] W. Ma, Y. Wen, and X. Yu, "Broadband metamaterial absorber at mid-infrared using multiplexed cross resonators," *Optics Express* **21**(25), 30,724–30,730 (2013).
- [206] F. B. P. Niesler, J. K. Gansel, S. Fischbach, and M. Wegener, "Metamaterial metal-based bolometers," *Applied Physics Letters* **100**(20), 203,508 (2012).
- [207] S. J. Tan, L. Zhang, D. Zhu, X. M. Goh, Y. M. Wang, K. Kumar, C.-W. Qiu, and J. K. W. Yang, "Plasmonic Color Palettes for Photorealistic Printing with Aluminum Nanostructures," *Nano Letters* **14**(7), 4023–4029 (2014).
- [208] S. Yokogawa, S. P. Burgos, and H. A. Atwater, "Plasmonic Color Filters for CMOS Image Sensor Applications," *Nano Letters* **12**(8), 4349–4354 (2012).

- [209] Q. Chen and D. R. S. Cumming, "High transmission and low color cross-talk plasmonic color filters using triangular-lattice hole arrays in aluminum films." *Optics Express* **18**(13), 14,056–14,062 (2010).
- [210] T. Xu, Y.-K. Wu, X. Luo, and L. J. Guo, "Plasmonic nanoresonators for high-resolution colour filtering and spectral imaging," *Nature Communications* **1**(5), 1–5 (2010).
- [211] Y. S. Do, J. H. Park, B. Y. Hwang, S.-M. Lee, B.-K. Ju, and K. C. Choi, "Plasmonic Color Filter and its Fabrication for Large-Area Applications," *Advanced Optical Materials* **1**(2), 133–138 (2013).
- [212] Q. Chen, D. Chitnis, K. Walls, T. D. Drysdale, S. Collins, and D. R. S. Cumming, "CMOS Photodetectors Integrated With Plasmonic Color Filters," *Photonics Technology Letters, IEEE* **24**(3), 197–199 (2012).
- [213] J.-L. Tissot, S. Tinnes, A. Durand, C. Minassian, P. Robert, M. Vilain, and J.-J. Yon, "High-performance uncooled amorphous silicon video graphics array and extended graphics array infrared focal plane arrays with 17- μm pixel pitch," *Optical Engineering* **50**(6), 061,006–061,006–7 (2011).
- [214] D. Moss, B. Gasharova, and Y.-L. Mathis, "Practical tests of a focal plane array detector microscope at the ANKA-IR beamline," *Infrared physics & technology* **49**(1-2), 53–56 (2006).
- [215] S. Cataldo, J. Zhao, F. Neubrech, B. Frank, C. Zhang, P. V. Braun, and H. Giessen, "Hole-mask colloidal nanolithography for large-area low-cost metamaterials and antenna-assisted surface-enhanced infrared absorption substrates." *ACS Nano* **6**(1), 979–985 (2012).
- [216] S. H. Mousavi, I. Kholmanov, K. B. Alici, D. Purtseladze, N. Arju, K. Tatar, D. Y. Fozdar, J. W. Suk, Y. Hao, A. B. Khanikaev, R. S. Ruoff, and G. Shvets, "Inductive Tuning of Fano-Resonant Metasurfaces Using Plasmonic Response of

- Graphene in the Mid-Infrared," *Nano Letters* **13**(3), 1111–1117 (2013).
- [217] H. S. P. Wong, S. Raoux, S. Kim, J. Liang, J. P. Reifenberg, B. Rajendran, M. Asheghi, and K. E. Goodson, "Phase Change Memory," *Proceedings of the IEEE* **98**(12), 2201–2227 (2010).
- [218] J. Hao, L. Zhou, and M. Qiu, "Nearly total absorption of light and heat generation by plasmonic metamaterials," *Physical Review B* **83**(16), 165,107 (2011).
- [219] W. Withayachumnankul, C. M. Shah, C. Fumeaux, B. S. Y. Ung, W. J. Padilla, M. Bhaskaran, D. Abbott, and S. Srimam, "Plasmonic Resonance toward Terahertz Perfect Absorbers," *ACS Photonics* **1**(7), 625–630 (2014).
- [220] H.-K. Lyeo, D. G. Cahill, B.-S. Lee, J. R. Abelson, M.-H. Kwon, K.-B. Kim, S. G. Bishop, and B.-k. Cheong, "Thermal conductivity of phase-change material $\text{Ge}_2\text{Sb}_2\text{Te}_5$," *Applied Physics Letters* **89**(15), 151,904 (2006).

ACKNOWLEDGMENTS

Looking back on four amazing years of plasmonics research in Stuttgart, I'm simply grateful for all the people who contributed to the success of this work, scientifically or otherwise.

Especially, I would like to thank:

- Prof. Harald Giessen for accepting me in his group and for giving me such a rewarding topic to work on. For his constant encouragement and guidance, and for all the opportunities and ideas he has provided over the years.
- Prof. Peter Michler, Prof. Thomas Zentgraf, and Prof. Hans Peter Büchler for taking the time to be on my examination committee.
- Dr. Na Liu for her ideas and for fruitful collaborations on several projects.
- Monika Ubl and Ramon Walter for all their nanofabrication assistance and insight in the Mikrostrukturlabor. Jürgen Weis for allowing me to work in the clean room at the Max Planck Institute for Solid State Research and Thomas Reindl for his lithography support.
- Nikolai Strohfeldt for being my office mate and good friend, for all the shared projects, and for always lightening the mood in the face of paper rejections and other troubles.
- All my colleagues at the 4th Physics Institute, who made the last years not only interesting, but also incredibly fun.

Finally, my heart-felt thanks go to my family and to my girlfriend. Without their continued support, encouragement and patience this thesis and also much of the studies preceding it would not have been possible.